8-2011

Monte Carlo Simulations of Single-Molecule Fluorescence Detection Experiments

William Neil Robinson
wrobinso@utsi.edu

To the Graduate Council:

I am submitting herewith a dissertation written by William Neil Robinson entitled "Monte Carlo Simulations of Single-Molecule Fluorescence Detection Experiments." I have examined the final electronic copy of this dissertation for form and content and recommend that it be accepted in partial fulfillment of the requirements for the degree of Doctor of Philosophy, with a major in Physics.

Lloyd M. Davis, Major Professor

We have read this dissertation and recommend its acceptance:

Christian G. Parigger, L. Montgomery Smith, Marianne Breinig, Horce W. Crater

Accepted for the Council:

Carolyn R. Hodges

Vice Provost and Dean of the Graduate School

(Original signatures are on file with official student records.)

Monte Carlo Simulations of Single-Molecule Fluorescence Detection Experiments

A Dissertation Presented for the
Doctor of Philosophy
Degree
The University of Tennessee, Knoxville

William Neil Robinson
August 2011

ACKNOWLEDGEMENTS

Thank you, Randy and Charlotte Garrett. You changed my life. Thank you, Dr. Parigger, for always being available to listen and give advice and for doing so much with the IGMCS program. Thank you, Carole Thomas, for coordinating all of CLA's outreach events. Those were amazing. Thanks to the awesome computer crew at UTSI: Richard Gulley, Charlie Gonzalez, and Lisa Lehman. I have appreciated all the help and computer parts! Thank you, Dr. Canfield, for editing much of this document. Thank you, Dr. Hofmeister, for the guidance and for several nice hikes throughout Tennessee. Thank you, Mom and Aunt Steff for all the prayers, emails, and support. Thank you, Mark Cross, for always being so helpful with connecting me to my committee. Thank you, Dad, for flying me up to Maryland and teaching me how to ski. A big thanks to my entire committee, Dr. Crater, Dr. Breinig, Dr. Smith, and Dr. Parigger for serving and for always being so understanding of scheduling difficulties. Thank you to John Jeffries and Dr. Greg Holiday for inspiring me to continue in Physics. I'd also like to thank Helen Mason for her contribution to my funding through the Helen Mason Fellowship. In addition, I'd like to thank the NIH for its support of this research. And finally, thank you, Dr. Davis, for being my advisor. Thank you for working with me through our difficulties, for challenging me, for finding funding for me, and for the excellent career advice and guidance.

ABSTRACT

Several Monte Carlo simulations of single-molecule fluorescence systems are developed to help evaluate and improve ongoing experiments. In the first simulation, trapping of a single molecule in a nanochannel is studied. Molecules move along the nanochannel by diffusion and electrokinetic flow. Single-molecule fluorescence signals excited by two spatially offset laser beams are detected and the direction of the flow is adjusted to try to equalize the signals and center the molecule between the beams. An algorithm is evaluated for trapping individual molecules in succession by rapidly reloading the trap after a molecule photobleaches or escapes. This is shown to be effective for trapping fast-diffusing single-chromophore molecules in succession within a micron-sized confocal region while accommodating the limited electrokinetic speed and the finite latency of feedback imposed by experimental hardware. In the second simulation, trapping of a molecule in a two-dimensional fluidic device consisting of sub-micron-separated glass plates is studied. Two different illumination schemes for sensing the molecule's position are compared: (i) a single continuous laser spot circularly scanned at 40 KHz or 240 KHz in the plane of the device; and (ii) four pulsed laser spots arranged in a square and temporally alternated at 304 MHz In either case, the times of detected photons are used by algorithms to control the electrokinetic flow in two dimensions to compensate diffusion and achieve single-molecule trapping. However each scheme is found to have limitations, as circular scanning produces a modulation in the fluorescence signal and in

the autocorrelation function, whereas the four-pulse scheme becomes ineffective if the fluorescence lifetime of the molecule is greater than the time between laser pulses, The third simulation investigates appropriate conditions for detection of single molecules flowing through an array of fluidic channels for an application to high-throughput screening for pharmaceutical drug discovery. For parallelized single-molecule detection, illumination is provided by a continuous laser focused to a line intersecting all channels and fluorescence is imaged to a single row of pixels of an electron-multiplying CCD with sufficient gain for single-photon detection. The simulation separately models each channel to determine laser, flow, and camera operating conditions suitable for efficient detection.

TABLE OF CONTENTS

LIST OF TABLES

LIST OF FIGURES

LIST OF ATTACHMENTS

Chapter 1: Introduction

1.1 Computer Simulations of Single-Molecule Experiments

Monte Carlo simulation of single-molecule detection in solution was first reported simultaneously with experimental results (1), and was used to give proof of concept and explore the parameter space of ongoing experiments, as it is in this dissertation. Other early work studied detection efficiency for single molecules in solution (2). Single-molecule simulations have also been used to study DNA tagged with multiple chromophores (3) and to study the noise in fluorescence correlation spectroscopy (4).

Simulation remains an important component in a wide array of recent work in single-molecule fluorescence science. Simulation has been used to explore photodynamics of specific emitters in different environments (5) and has been used alongside fluorescence resonance energy transfer (FRET) spectroscopy to study protein folding (6). It has also been used to develop new FRET techniques that can extract more information from experiments (7).

The simulations in this dissertation are based on algorithms designed for generating the times of arrival of detected photons by use of variable time intervals for the photophysical processes. These algorithms are featured in work studying fluorescence correlation spectroscopy (8) including triplet crossing and saturation (9). Enderlein's

initial proposal of tracking molecules with a scanning laser spot was tested with simulation (10), and Moerner's group recently developed a simulation for testing a new scanning pattern for use with the Anti-Brownian ELectrokinetic (ABEL) trap, an implementation and expansion of Enderlein's proposal discussed in the next section (11).

Several theses and dissertations from the University of Tennessee Space Institute have developed simulations to study and help improve a number of different single-molecule spectroscopy experiments. Dennis Bunfield presented a MS thesis on single-molecule detection that included a maximum likelihood estimation of fluorescence lifetime for the distinction of molecular types (12). Yuxing Sun presented a PhD dissertation that compared the maximum likelihood estimation technique in Bunfield and Davis's earlier work with a neural networking technique, which could be trained to achieve improved single-molecule identification by also accounting for other molecular photophysical properties (13). My own MS thesis presented initial simulations of single-molecule trapping in one dimension in a nanochannel (14). This has been further developed for more detailed studies as a part of the first simulation reported in this dissertation.

This dissertation also presents two other simulations that each study separate experimental setups. One compares two different illumination and position sensing strategies for single-molecule trapping in two dimensions. Hence Section 1.2 below provides introductory information and a literature review on trapping and tracking single

molecules. The last simulation studies single-molecule detection in a flowing solution in a nanochannel with detection by use of an electron multiplying charge-coupled device (EM-CCD) camera. A single continuous laser can be focused onto a line across many channels, and the fluorescence response can be imaged onto a EM-CCD camera for parallelized single-molecule detection. The simulation models a single fluidic channel to determine appropriate laser, flow and camera parameters. More on single-molecule detection and on the camera is discussed in Section 1.3.

1.2 Single-Molecule Tracking and Trapping

Tracking and trapping single molecules that freely diffuse in solution has become an important and developing need in nanoscience and biotechnology (15). Confocal fluorescence microscopy allows the detection of a single molecule, but except in highly viscous solutions, the molecule will swiftly diffuse out of a focal region. To prolong the observation time, the molecule may be attached to a surface or to an anchor such as a polystyrene nanobead, but this may change the internal dynamics and interactions of the molecule. It is therefore desirable to observe and manipulate molecules that are free in solution.

There are established techniques for trapping in one (16) and two (17) dimensions, and techniques for tracking in two (10, 18-20) and three (21-23) dimensions. Tracking is the

adjustment of optics and/or the sample stage to keep a fluorescent molecule in focus and centered in the field of view; trapping is the movement of the molecule and/or the surrounding solution by electrokinetics, magnetokinetics, or optical manipulation back into a constant region of observation as the molecule is displaced by diffusion.

One dimension

Our group has performed experiments demonstrating trapping in a nanochannel, where the molecule's motion is limited effectively to one dimension (16). Earlier work on the detection of fluorescent molecules in nanochannels was reported in 1997 (24). Lab-on-a-chip devices can be routinely fabricated with multiple nanochannels (25). For illumination of the nanochannel trap, a single pulsed laser beam was passed through a beam splitter and traveled along two separate paths (16). One path was longer than the other such that laser pulses would arrive alternately at two overlapping spots along the nanochannel as seen in Figure 1. A 3-D mockup of the trap in action is presented in Attachment 1. In the experiment, time-gated photon detection with a single-photon avalanche diode (SPAD) detector was used to map detected photons to the laser pulse most probably responsible for excitation. Two electrodes provided electrokinetic position control by inducing flow to the left if the right spot were responsible for more excitations and vice

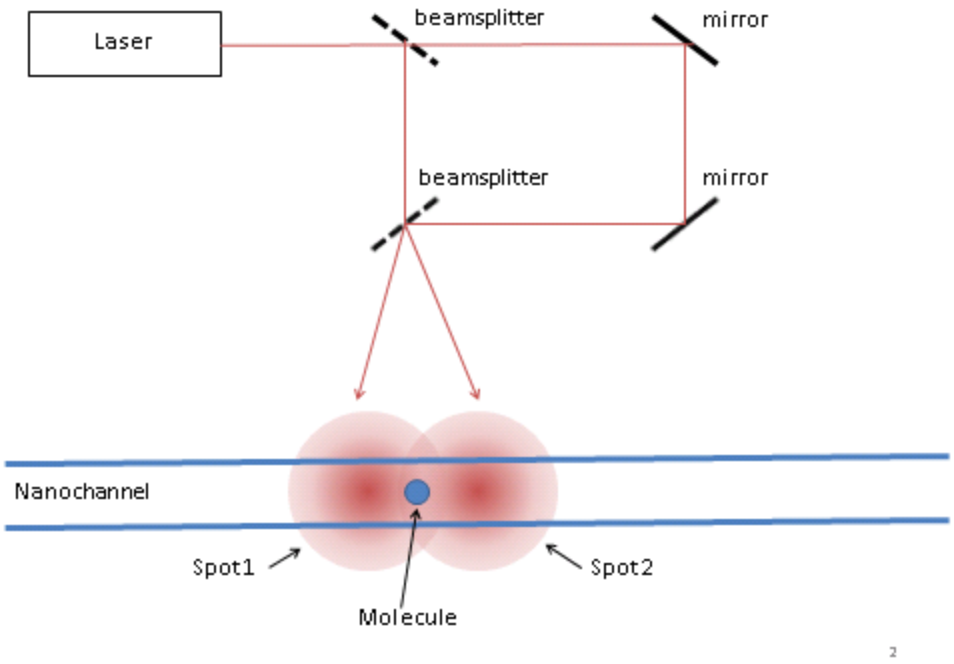

Figure 1. Diagram of the 1-D trapping setup. A single laser source provides pulses that are split at the first beamsplitter and sent down separate paths to recombine at the second beamsplitter, such that the pulses arrive 6.6 ns apart at the left and right spot locations respectively. At the bottom of the figure, a molecule moves through the nanochannel, where it experiences laser irradiation, possibly emits fluorescence, and then has its position modulated between the laser spots by electrokinetic flow.

versa. Here, trapping was strongly displayed. However, the molecules would eventually stick to the walls of the nanochannel and become immobilized so that a fresh device would be needed for each new experiment.

Chapter 2 of this dissertation discusses the underlying physical processes and the algorithms for computer simulations of trapping in one dimension. Detailed results from the 1-D trapping simulations and comparison with experimental results are presented in two papers, which are included in Appendices 1 and 2.

Two and three dimensions

In 2000, Enderlein put forth a technique for compensating the Brownian diffusion of a molecule in two dimensions by first sensing its position by use of a circularly scanning laser spot (10). He proposed a system using feedback with a confocal microscope such that detected photons from the molecule are used to control a translation stage, which attempts to keep the molecule at the center of the detection region. The fluorescence is detected as an analog signal, which is modulated at the frequency of rotation of the laser spot. The phase of modulation gives the angular location of the molecule, while the amplitude of modulation gives the radial displacement of the molecule from the center of the circle. In one subsequent implementation of this technique by Cohen et al., rather than

use of analog lock-in detection, the time of arrival of a single photon is mapped against the period of the rotating laser spot to estimate the molecule's position (17). As described below, the simulation study in this dissertation considers this last form of position estimation from the timing of single-photon detections.

Several groups have developed tracking techniques for single molecules in two dimensions using the circular scanning technique (10, 18-20), and Cohen and Moerner have performed trapping with their **A**nti-**B**rownian **EL**ectrokinetic (ABEL) trap (17). The trapping of single molecules in solution is a growing field (26). The ABEL trap used four electrodes to provide electrokinetic control of a fluorescent molecule confined between two glass plates. Here, a scanning laser spot provides excitation, similar to Enderlein's setup; however, instead of translating the sample with a stage, which is slow due to the inertia of the stage, the molecule's position was controlled directly via electrokinesis induced by the electrodes. The device used a pair of acousto-optic beam deflectors (AOBD) to move the focused laser spot in a circle in the plane of the trap, and the performance was limited chiefly by the period of the rotation of the spot and the latency of the feedback system. The shear-wave AOBD chosen for their experiment was operated at 40 kHz (27), but Cohen stated that a longitudinal-wave AOBD capable of operating at 260 kHz would be preferable.

It is worth noting that other illumination schemes have recently been evaluated, such as Wang and Moerner's "knight's tour" scan pattern (11) for the ABEL trap, which has trapped 10 nm molecules in simulation. This scanning pattern is a complex series of "jumps" in a 2-D region with ~1 μs occupancy time at each spot. The authors claim that this implementation is a necessary improvement over circular scanning in order to trap molecules as small as 10 nm inside a 2 μm wide illumination region with photon detection rates as low as 14 ms^{-1}. Most recently, Fields and Cohen have demonstrated trapping with this illumination scheme of a molecule 800× smaller than previously trapped for times greater than 1 s (28). The advance over previous work was in part due to the addition of a Kalman digital filter technique (29), wherein an appropriate weighting of the theoretically predicted position probability density and the latest experimental photon data are combined for an improved estimate of the molecule's position.

Tracking has been performed in 3-D by modulating the scanning laser circle in the axial direction to outline a cylinder. Tracking has been achieved using this technique via one-photon excitation (18) and two-photon excitation (20). Recently, new illumination and imaging techniques featuring custom point spread functions have been used to track nanoparticles in 3-D. These techniques have been used on quantum dots in solution and in living cells (30-33).

Other types of trapping exist that involve magnetic control (34-37), but these require tethering the molecule to a bead, which is not desirable for many studies. Optical trapping, first reported by Ashkin in 1997 (38), is popular for many applications (39), but the intensity required to trap scales nonlinearly with the inverse of the particle size (40). For single, fluorescently labeled biomolecules, this results in unfeasibly high laser powers and rapid photobleaching, which here is the destruction of the molecule by the laser. Photobleaching occurs when the absorption of a photon breaks bonds in the molecule such that it may no longer fluoresce.

Another interesting 2-D tracking technique is photothermal tracking, specifically **S**ingle **Na**noparticle **P**hotothermal **T**racking (SNaPT) (41). Laser light is scattered from a gold nanoparticle and heats the local environment. The increase of temperature will change the refractive index of the medium and thus enable detection when the region is repetitively scanned. Particles as small as 5 nm have been tracked in living cells with this technique.

Another experiment trapped and manipulated single quantum dots for over an hour at a time in two dimensions by using electrokinetic manipulation and a CCD camera for detection (42). A broad 532 nm, 250 W/cm^2 source was used over the entire area of interest. To obtain these results, the quantum dot was suspended in a solution with a viscosity 230 times higher than that of water at room temperature. This setup later

achieved application in the affixing of these quantum dots to a surface with 132 nm precision (43).

Whereas the above described work demonstrates that single-molecule trapping has uses in nanofabrication, most setups for single-molecule trapping are motivated by a desire to prolong the observation time of a freely diffusing molecule. In this case, relevant figures of merit include the trapping time and the number of photons detected from the molecule before photobleaching or escape. Simulation provides useful information not possible to obtain in experiment, but the simulated data is also studied by taking the autocorrelation function (ACF) of the detected photon stream. The ACF width shows the mean trapping time, and its amplitude is inversely proportional to the trap occupancy. As there are several different approaches to trapping with different experimental hardware requirements, computer simulations provide an effective method of comparison.

Chapter 3 of this paper describes the use of Monte Carlo simulations to study two-dimensional trapping of a single fluorescent emitter in a solution of water using two different illumination schemes. The first entails a circular-scanning laser spot, simulated as a spot that moves between sixty-four discrete locations approximating a circle. The other is a new technique extended from that used for trapping a molecule in a nanochannel: a pulsed laser source is split into four paths that are aligned and temporally delayed to produce four focused laser spots in a square pattern in the plane of the sample

cell, and with pulses that arrive successively in time. These setups are both shown in Figure 2. Video mock-ups of these traps are presented in Attachments 2 and 3. In both of these setups, a SPAD provides single-photon detection, and the times of arrival of the individual photons are recorded. Whereas Enderlein's initial proposal for trapping in 2-D entails lock-in detection of an analog fluorescence signal (10), this study only considers single-photon detection as implemented in Ref. (17).

The desired result of the study is to provide a comparison of our new technique with the most common illumination scheme of similar experiments and to determine the advantages of each approach under different operating parameters. The goal of both setups is to trap a single molecule at mean fluorescence photon detection rates of $\sim 10^5\ s^{-1}$ and to replace the fluorescently labeled molecule quickly in the event of escape or photobleaching.

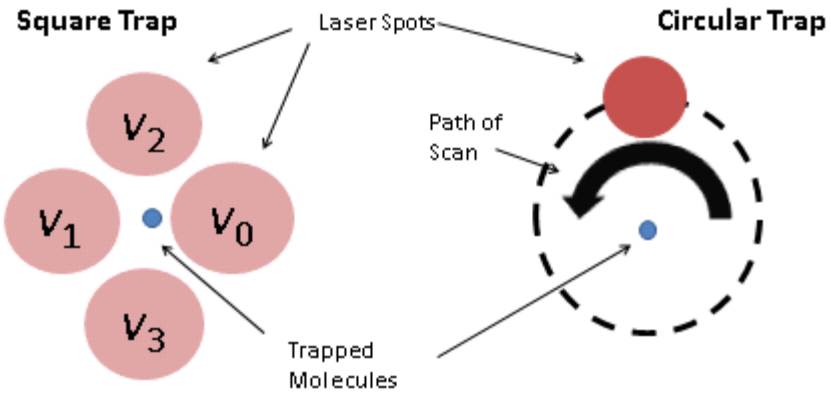

Figure 2. Diagram of the two trapping configurations. In the square configuration shown on the left, laser pulses from a single source are split and delayed such that they arrive at vertices *v*0, *v*1, *v*2, and *v*3 in numerical order spaced 3.3 ns apart. In the circular configuration shown on the right, a single spot is scanned in a circle. In both cases, a molecule is shown trapped between the beams as it experiences irradiance, and possibly emits fluorescence after excitation. The fluorescence is used as feedback to modulate the molecule's position via electrokinetics.

1.3 Detection of Single Molecules in a Flow with an EM-CCD Camera

Single-molecule detection is a critical part of today's fluorescence spectroscopy research (44) including medical and biological topics like DNA sequencing (45). Although there are other techniques for detecting single molecules, fluorescence detection was reported in 1990 (1) and remains a popular and preferred method for a variety of experiments (46). Fluorescence detection may be performed in a variety of ways (47). In the other simulations described in this dissertation, a confocal microscope images fluorescence photons onto a SPAD detector. Though not common, it has been shown that EM-CCDs can be used in fluorescence correlation spectroscopy with sufficient time resolution to resolve the diffusion of individual dye molecules (48). Other work has used the EM-CCD in simulation for spatially-resolved single-molecule detection (49). Here multiple excitation volumes were imaged onto separate areas of the EM-CCD to achieve detection in parallel. With a time resolution of 20 μs, the diffusion of single dye molecules was resolvable.

Chapter 4 of this dissertation describes a simulation of single-molecule detection in a nanochannel for the application of high-throughput screening. This kind of screening has application in pharmaceutical drug development and other areas of science (50). Work is underway to perform hundreds of single-molecule detection experiments in parallel using a lab-on-a-chip device containing hundreds of micro/nanochannels illuminated by a

single continuous-wave laser source with detection of light provided by an Andor iXon 897 EM-CCD camera (51). Simulation of a fluidic channel of the device gives guidance to the experiment by showing feasibility of detection across a range of parameters and allowing comparison of the different possible modes of operation of the EM-CCD camera.

The camera has a 512 × 512 pixel sensor that has a quantum efficiency for conversion of 600 nm photons to photoelectrons of ~90%. Electrons at each pixel of the sensor are transferred to a 512 × 512 frame-transfer buffer, and from there they are digitized, with possible gain prior to digitization, while another frame of signal is accumulated on the sensor. The camera software enables considerable flexibility in how the charges are shifted from the sensor to the frame transfer buffer, in binning of charges in adjacent pixels, and in how the charges are digitized.

For the experiments on parallelized single-molecule detection, the row of fluidic channels is illuminated by a laser focused to a narrow line, which intersects all the channels. The fluorescence light from the narrow line of illumination is imaged onto the camera sensor to just a single row of pixels, or just a few rows of pixels that are subsequently binned together. Similarly, each fluidic channel in the line of illumination is imaged to a single pixel in the row, or just a few pixels that are binned together. The setup is shown in Figure 3, and a video is shown in Attachment 4.

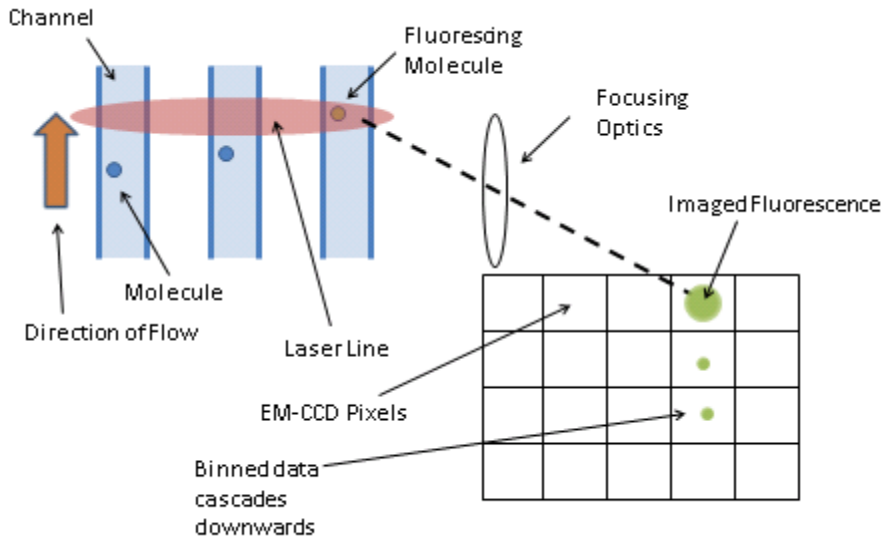

Figure 3. Diagram of the parallelized single-molecule detection experiment. Multiple channels, shown in blue, are illuminated by a single laser beam focused across the fluidic channels in a line and along the length of the channels as a Gaussian. The fluorescence from molecules that pass through the excitation region is imaged onto a region of an EM-CCD, shown as a black grid. After a set exposure time, the charges in the pixels of the EM-CCD are shifted downwards, and new data is collected at the top.

The readout of the charges in the pixels, or binned pixels, of the camera can be performed in a number of ways, and one of the goals of this study is to compare the different readout methods. Hence the camera is simulated in different modes: (i) kinetics mode with continuous readout or (ii) fast kinetics mode with shorter possible exposure times. Either of these modes may be operated with or without gain and at different exposure times and digitization rates.

Kinetics mode features continuous recording via frame transfer. The lowest possible exposure time for this mode is 122 µs, achieved by binning just a few rows of pixels, so that each exposure requires digitizing just a single row. As the pixels are continuously digitized from the frame transfer buffer faster than the exposure time, there is effectively no dead time between each exposure. Fast kinetics mode features a shorter minimum exposure time, down to 1 µs, limited mostly by the time taken to shift charges from one row of camera pixels to the next. In fast kinetics mode, the fluorescence is imaged to just the top row of pixels, so the other 511 rows of pixels in the image area and the 512 rows of pixels in the frame transfer buffer can be used to store data. Once these 1023 rows each hold data, the camera temporarily slows the rate of shifting charges until all 1023 rows of stored data are digitized. The rate of digitizing pixels is 10 MHz (i.e., 100 ns/pixel), which gives 51.2 µs for each row of pixels. So for a 1 µs exposure time, after every 1.023 ms of recording time, there will be an effective dead time of approximately

52.4 ms (1023 × 51.2 µs). The exact value must account for the charge shift times as well as the digitization time.

One of the major findings of the simulation is that it is possible when using a gain of 1000 to detect the majority (>95%) of single molecules that flow through the channel at velocities between 1×10^{-4} and 7.5×10^{-4} m/s with the camera operating in kinetics mode with a bin time of 122 µs, as shown in Section 4.3. Similarly successful detection was possible at longer bin times when using slower velocities and slower camera readout without gain.

1.4 Programming Environment and Tools

The simulations created for this doctoral research are written for the Intel C++ compiler version 11.1. The Intel compiler includes a library of routines for generating arrays of pseudo-random numbers of various specified distributions. This simulation used multiple concurrent streams of the uniform, exponential, Gaussian, and geometric distributions, which are all transforms of the MCG31 implementation of the Mersenne twister. MCG31 is the default generator and is one of, if not the fastest of, the Intel Math Kernel Library (MKL) generators. It has a short period compared to other generators, but this period, though approached, is not exceeded in the reported simulations.

One computer used to run the simulations presented in this dissertation was an eight-processor machine running Windows XP and Cygwin (a Linux-like environment for use inside Windows). The simulations can be run with different parameter sets concurrently across the eight processors using the job control features and scripting features available in the Bash shell and Python. For most parameter sets, simulations only take a few minutes to run, and 1-100 runs are scheduled at a time.

An early version of the simulation of single-molecule detection presented in Chapter 3 was written in Matlab and then recoded into C++ to increase its speed. Analysis and graphing was done in Python with NumPy and Matplotlib (Matlab-like plotting environment for Python), Gnuplot, Matlab, and Excel.

Chapter 2: Simulation of Electrokinetic Trapping in 1-D

2.1 Overview

Simulations of trapping molecules in a nanochannel were presented in my Master's thesis (14). As part of my doctoral research, a more detailed study on this topic was completed. This included evaluation of the autocorrelation function (ACF) of the detected photon signal and of the time-averaged concentration profile of the molecules in the trapping region over a wide range of parameters, including varying laser power. The effects of latency of feedback were examined. Also, the mean number of photons emitted per molecule and the average time each molecule spends in the trap were used as a measure of the trapping performance. These results and their comparison with previous experimental results have been published in the paper presented in Appendix 1 (52).

The publication in Appendix 1 also shows the effect on trapping performance when the split of power between the two laser spots is uneven. It was found that the trapping performance improves when the downstream beam is brighter. The reason for this is that if a molecule escapes upstream, flow is increased to bring in a new molecule, and the escaped one thus returns to the illumination region possibly to become trapped again. If it escapes downstream, then it is flushed from the chamber; hence preventing escape on the downstream side is more critical.

The paper in Appendix 2 (53) presents a review of the experiments and extends the simulations to consider the effect on trapping performance of the separation of the laser spots. The trapping performance is measured by the time-averaged concentration of molecules in the trapping region, the mean number of fluorescence photons detected per molecule, and the mean time each molecule spends in the trap before photobleaching or escape. Although the trapping performance improves according to these metrics when the spot separation is increased, Appendix 2 shows that there is an additional bump in the ACF because the fluorescence signal fluctuates in time as the trapped molecule diffuses between the two laser spots. A similar additional bump in the ACF is found when the split of power between the two laser spots is uneven.

While detailed results of the simulations of single-molecule trapping in 1-D are presented in the Appendices and are not repeated in the body of this dissertation, the algorithms and underlying physical processes form the basis of the other simulations of this dissertation, and hence are briefly presented below.

As discussed in Section 2.2, simulation of trapping in 1-D uses a discrete grid for molecular transport and features a control algorithm used in a feedback loop for active trapping of a single molecule. A vector holds the times of scheduled events. These events can be diffusion, translation, change of speed of translation, entry into simulation, excitation of a molecule, or decay from the excited state with possible photon detection.

Between each event, the array or vector is searched for the lowest time value. The event corresponding to this value is performed next, and new events are scheduled at the conclusion of this event, while other scheduled events may be canceled or rescheduled. For example, when diffusion occurs, molecules have their times of next possible excitation recalculated and also the time of next diffusion is scheduled. Diffusion could also result in a molecule leaving the simulation volume and the subsequent cancellation of all photophysical events scheduled for that molecule. So there is no overall fixed time-step, and the time between events can be short when a molecule is rapidly exciting and decaying, or long when there are no molecules near the center of the illumination profile or when there are no molecules in the simulation volume at all.

2.2 Molecular Motion

As a numerical approximation, molecule positions are confined to a finite grid, which represents the simulation volume. Molecules in the simulation volume move under two independent influences: diffusion and flow. Diffusion along the discrete grid occurs at times determined by the grid spacing Δx and the diffusion coefficient D. The grid spacing is set to Δx = 0.01 μm, which is small compared to the 0.5 μm beam waist of each laser focus. Fick's second law of diffusion in one dimension is given by

$$\frac{\partial \rho}{\partial t} = D \frac{\partial^2}{\partial x^2} \rho \,, \tag{1}$$

where $\rho(x)dx$ is the probability of finding a molecule within *dx* of *x*. With the initial condition that the molecule begins at the origin, $\rho(x, t=0)dx = \delta(x)dx$, the solution to Eqn. (1) is:

$$\rho(x,t)dx = \frac{1}{\sqrt{2\pi}\sigma(t)} \exp\left[\frac{-x^2}{2\sigma^2(t)}\right]dx, \tag{2}$$

which is a normalized Gaussian distribution with a standard deviation

$$\sigma(t) = \sqrt{2Dt}\,. \tag{3}$$

To model diffusion on the grid, each molecule can move to a new grid location at regular fixed time intervals Δt_D, chosen such that the standard deviation is equal to the grid size:

$$\Delta t_D = \frac{\Delta x^2}{2D}\,. \tag{4}$$

When a diffusion event occurs, every molecule undergoes steps described below that allow it to move randomly. If a molecule moves and it is in the ground state, a new excitation time is calculated, as discussed in Section 2.3, because the laser irradiance at the molecule's new position may have changed, but if a molecule moves off the grid, it is removed from the simulation.

The diffusion process uses one 32-bit uniform random number between 0 and 1 to determine movement along the channel. This number is compared against the cumulative probabilities in Table 1, which are determined by numerically integrating the Gaussian

Table 1. Cumulative probabilities for diffusion in one dimension.

J	$P(j)$ Value
0	0.382924922548026
1	0.624655260005155
−1	0.866385597462284
2	0.926983133405366
−2	0.987580669348448
3	0.993557705595188
−3	0.999534741841929
4	0.999763973247840
−4	0.999993204653751
5	0.999996583337313
−5	0.999999962020875
6	0.999999980970278
−6	0.999999999919680

distribution of Eqn. (2) as discussed in Appendix 1, to determine how many grid spaces the molecule will move. If the random number is less than or equal to $P(0)$, it does not move. If the number is greater than $P(0)$ but less than or equal to $P(1)$, then it moves one step in the positive direction. If the number is between $P(1)$ and $P(-1)$, then it will move one step in the negative direction. Likewise, if the number is between $P(-1)$ and $P(2)$, it will move two steps in the positive direction, and so on.

The molecules are also moved by an applied electrokinetic flow, i.e., by electrophoresis and electroosmosis. When the simulation begins, a constant drift velocity v_F is simulated, and a translation of one grid step for each molecule occurs at regular time intervals Δt_F such that

$$v_F \, \Delta t_F = \pm \Delta x \, . \tag{5}$$

When trapping is underway, the flow can be turned off or have its direction reversed, as photons are detected. The time of the next flow step is changed whenever the flow velocity is adjusted. If the velocity changes from v_F to v_F' at a time t' following the last translation, then the time until the next flow step is $\Delta t_F'$ such that

$$v_F t' + v_F' (\Delta t_F' - t') = \pm \Delta x \, . \tag{6}$$

Entry and exit of molecules to and from the simulation can occur due to diffusion or applied flow. These possibilities are handled as separate events. If the molecule enters due to flow, it is placed at the upstream edge of the simulation volume. For entry due to

diffusion, the molecule may enter at any of the five most upstream points or five most downstream points on the grid, as given below.

The frequency of entry by either method is dependent on the mean number of molecules per grid point, C_0,

$$C_0 = 10^3 N_A C \, \Delta x \, d_y d_z \,, \tag{7}$$

where N_A is Avogadro's number, C is the molar concentration of the solution, and d_y and d_z are the width and depth of the channel. For a concentration C = 100 pM and $d_y = d_z = 10^{-7}$m, $C_0 = 6\times10^{-6}$ molecules per grid point.

When molecules diffuse to new grid points, there is a chance that some may move off the grid and leave the simulation, but there is an equal possibility that new molecules may diffuse onto the grid. Again, the probabilities that molecules enter at various points on the grid are determined by adding contributions found by numerically integrating the Gaussian distribution of Eqn. (2), as discussed in Section 2.2 of Appendix 1. The key findings are: (i) the total probability that a molecule can move onto the 1-D grid due to diffusion with a precision of $1{:}2^{32}$ for comparison with a 32-bit random number is given by

$$P(\text{1-D}) = 0.763540130047191 \, C_0; \tag{8}$$

and (ii) Once a molecule is scheduled to enter by diffusion, the Q_k values listed in Table 2, which are derived in Section 2.2 of Appendix 1, are used in comparison with a uniform random number between 0 and 1 to determine placement relative to the simulation edges. Here a random number lower or equal to Q_0's value would result in a molecule generated at the upstream edge of the channel; higher than Q_0 but less than or equal to Q_L, and the molecule will enter on the right edge. This continues as in the example of diffusion above.

Table 2. Cumulative probabilities for new entry positions in one dimension.

k	Q_k Value
$-L$	0.404066599711270
L	0.808133199422541
$1-L$	0.895625174513805
$L-1$	0.983117149605069
$2-L$	0.991249444832068
$L-2$	0.999381740059067
$3-L$	0.999686395503419
$L-3$	0.999991050947771
$4-L$	0.999995500604795
$L-4$	0.999999950261819
$5-L$	0.999999975130910
$L-5$	1.000000000000000

2.3 Excitation and Photophysics

Laser irradiation is provided by pulses from a single source, split and temporally alternated such that every odd pulse arrives at one of the two locations 6.6 ns before an even pulse arrives at the other location. The laser intensity from spot n = 0, 1, at a location along the channel x at time t is given as

$$I_n(x,t) = \frac{2P}{\pi\omega_0^2} \exp[-2(x-x_n)^2/\omega_0^2] \sum_j \delta(t - jT - nT/2), \quad (9)$$

where P is the laser power in each beam , ω_0 = 0.5 μm is the laser beam waist, x_n is the position of the active laser spot, $\delta(t)$ is the Dirac delta distribution, which represents the temporal profile of a laser pulse, and T = 13.2 ns is the period. The rate of excitation is then given by

$$k_n(x,t) = \sigma_a I_n(x,t) / E_\lambda , \quad (10)$$

where σ_a is the absorption cross-section, and E_λ is the photon energy. Multiplication of k_n by the period T yields the probability that a molecule in the ground state is excited for each laser pulse. Two geometrically distributed random numbers, each giving the number of laser pulses that would occur until the next possible excitation by each of the beams, are generated with these two probabilities of excitation as the probabilities of success. Unless an intervening event such as diffusion occurs first, the next molecular excitation will occur at the earlier of the two times.

The possible relaxation pathways of a molecule after excitation from the ground state S_0 to the S_1 excited state are shown in the Jablonski diagram in Figure 4. Using a similar cumulative probability process as described for diffusion and molecular entry, once the molecule is excited, it has a 5% chance of producing a detectable photon (path *ii*). It has a 0.1% chance of entering the triplet state via intersystem crossing from the S_1 excited state with an expected decay time of 1 μs (path *iii*). Decay from the triplet manifold occurs usually by radiationless decay or quenching without photon emission and rarely by emission of phosphorescence. The detection of phosphorescent photons is not modeled as the event is rare. The phosphorescent emission spectra have lower energy than fluorescence, and most phosphorescence would thus be filtered out. There are also a chance of photobleaching and being removed from the simulation (path *iv*) and a chance of decaying from the singlet state without emission of a detectable photon (path *i*).

Table 3 displays the probabilities to determine the decay path for each excitation. When decaying from the singlet state, the expected decay time is 3 ns. From the triplet state, the expected decay time is 1 μs, and from either the singlet or triplet state, an exponentially distributed random number with a mean equal to the expected decay time is produced to determine the actual time of decay. When relaxation pathway *ii* occurs, a random Gaussian number with standard deviation $\sigma = 127.4$ ps and a mean of 3σ is added to the decay time to represent timing jitter of the SPAD detector. The modified decay

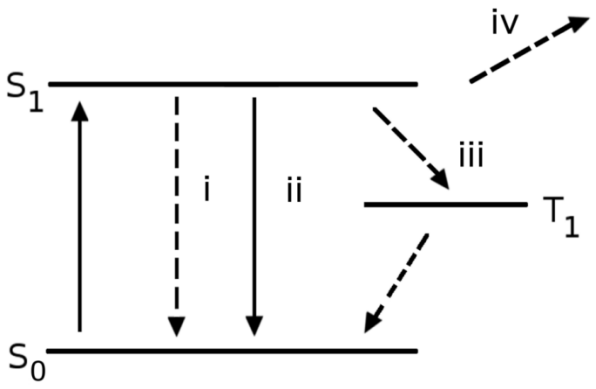

Figure 4. Jablonski diagram for the relaxation pathways of a molecule in simulation. S_0 is the singlet ground state, S_1 is the singlet excited state, and T_1 is the triplet state. *i* represents decay without detected photon emission, *ii* is the case of detected photon emission, *iii* is the case of inter-system crossing from the singlet excited state to the triplet manifold, and *iv* is the case of photobleaching, where the molecule becomes non-fluorescent or destroyed.

Table 3. Relaxation pathway probabilities

Path	Mechanism	Probability
i	Singlet decay without photon detection	$P_{(i)} = 1 - P_{(ii)} - P_{(iii)} - P_{(iv)}$
ii	Singlet decay with photon detection	$P_{(ii)} = 0.05$
iii	Triplet Crossing	$P_{(iii)} = 10^{-3}$
iv	Photobleaching	$P_{(iv)} = 10^{-5}$

time is recorded as an unsigned integer time-stamp ts_i representing the number of laser pulses that have arrived since the simulation began.

Background photons may also be detected, consisting of detector dark counts (d = 50 s^{-1}) and scattered light coming through the filters (s = 15 μW^{-1} s^{-1}). The background rate B is set in simulation as $B = s\overline{P} + d$, where $\overline{P} = 2P$ is the sum of the laser powers in each of the two beams. These photons are assumed to be Poissonian such that the timing of the next background photon is determined by an exponentially distributed random number with a mean equal to 1/B. For either detection case, fluorescence emission or background, there is a 0.5% chance that the detector experiences an afterpulse. In this case, another photon detection will be scheduled to occur at a random time later with an exponential distribution with a mean of 100 ns. Also, the detector has a dead-time of 40 ns, during which it ignores any incoming photons (54).

2.4 Trapping

The trapping algorithm adjusts the flow velocity based on the unsigned integer time-stamps ts_i of the last 6 detected photons. The minimization of the error in the estimate of a molecule's position requires a balance between shot noise, which decreases with the number of collected photons, and the uncertainty due to diffusional motion that occurs

while acquiring photons. The number 6 was obtained from an analysis of these factors (55) and was used in experiments (16). When the channel is empty of fluorescent molecules, the detected signal falls to the level of the background detection rate, and the flow is set to a maximum to bring new molecules into the illumination region. Every time a photon is detected, the difference between the time-stamp of the most recent photon and the one detected two photons earlier must be less than a threshold.

If this check is passed 6 times in a row, a molecule is assumed to be in the trapping region, and active trapping begins. If more of the last 6 photons are odd (even), then the molecule is assumed to be to the left (right) of the center of the trap, so the velocity is set towards the right (left) at its maximum speed after a delay of 6 μs representing the latency of the simulated system. If the numbers of odd and even time-stamps are the same, then the flow is set to zero. If the threshold check fails, the flow is set to zero while more photon time-stamps are collected and the check is repeated. If it fails five or more times in a row, trapping ceases and the flow is set to a maximum to bring in a new molecule. See the flow chart in Figure 5, which is also Figure 4 in Appendix 2.

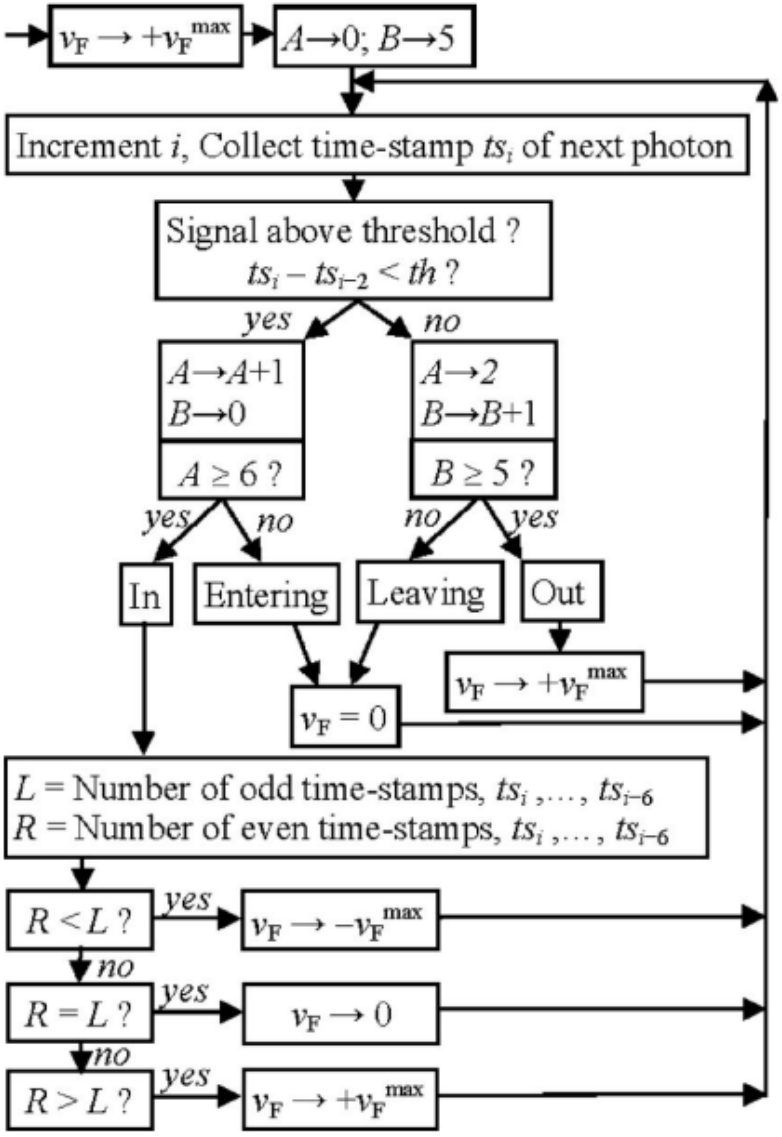

Figure 5. Flowchart of the trapping algorithm used in the nanochannel trap.

Chapter 3: Simulation of Electrokinetic Trapping in 2-D

3.1 Overview

This chapter studies single-molecule trapping in two dimensions by use of simulations that are an extension of those described in Chapter 2. A fluidic device consisting of glass surfaces spaced 0.1–1.0 microns apart defines the 2-D region of interest, as molecules are effectively confined in one dimension between the two surfaces, but free to move in the other two dimensions. To achieve trapping in 2-D, temporally and spatially varying laser illumination together with fast, time-gated photon detection are used to gain information on the position of the molecule, which is then used to control the voltages at four electrodes and thereby counteract Brownian diffusion by electrokinetic motion of the molecule. Illumination and position correction are achieved through two different schemes. In the first, illumination is provided by a pulsed laser spot that alternates between the four vertices of a square, which are positioned in the plane of the 2-D region between the glass surfaces and the molecule is repositioned to the center of the square. The order of the pulses at the vertices as seen in Figure 2 (page 13) is v_0, v_1, v_2, v_3. In the second, a single focused laser spot is swept around in a circle in the plane of the 2-D region and the molecule is repositioned to the center of the circle, as also shown in Figure 2. For the case of one-photon excitation, the laser is continuous, while for the case of two-photon excitation it is pulsed with a repetition rate of 304 MHz .

Detection of individual photons is performed by a single-photon avalanche diode (SPAD) and the times of detection are used by the control algorithm to adjust the electrokinetic motion to reposition the fluorescing molecule. Features of the detection via SPAD that are included in the simulation include single-photon detection efficiency, background, afterpulses, dead-time, and photon timing jitter, which are summarized in Table 4 and discussed above in Section 2.3. Both schemes are simulated separately with one- and two-photon excitation, which are discussed in Section 3.2.

This simulation uses a discrete 2-D grid for molecular transport and features extensions to the control algorithms developed for trapping a single molecule in the 1-D simulation.

To simulate excitation of molecules by the laser beams, a molecule's location relative to an active laser spot is mapped to a list of pre-generated random numbers, which allow the time of the next possible excitation to be determined. For pulsed excitation (i.e., for the square trap or for two-photon excitation with the circular trap), these random numbers have a geometric distribution with a mean equal to the mean number of laser pulses before excitation. They represent the number of laser pulses that occur before a possible excitation, given the intensity at the location of the molecule. For the circular trap, the numbers represent a time until excitation and are exponentially distributed. This is described in more detail in Section 3.3.

Table 4. SPAD parameters

Parameter	Value
Detection efficiency	65%
Dark counts	50 s^{-1}
Dead-time	40 ns
Timing jitter (Gaussian std. dev.)	0.127 ns
Chance of afterpulse	0.5%
Afterpulse 1/e decay time	100 ns

Next, the times of molecular entry for the next entries from diffusion and flow are calculated by generating exponentially distributed random numbers that represent the waiting time until the next entry. The positions of these entries are found by comparing random uniform numbers against cumulative probabilities as described in the next section, and events for these entries are loaded into a vector.

As in the 1-D simulation, a vector of the times of possible future events drives the simulation. Most of the results for the 1-D simulation were taken with a version of the code that uses a C++ vector of fixed dimension, which includes space for a fixed number of molecules, greater than the maximum number of molecules in the simulation. For the 2-D simulation, a dynamically sized C++ vector is used, wherein a memory reallocation expands or contracts the vector whenever a molecule enters or leaves the simulation volume. This allows for any reasonable number of molecules to occupy the simulation at the cost of some time for memory reallocation. Each event object in the vector is no longer a time but a data structure that contains the time of the event, the event type, an ID-number, and a double-precision floating point variable named ‘extra’ to be used differently by different events. The class that defines these objects also has a static member function find_index_of_next_event(), which finds the event with the lowest time value upon making a pass through the vector.

3.2 Molecular Motion

For simulation of diffusion in two dimensions, two uniform random numbers are used to determine movement in the *X*- and *Y*-directions separately. These two random numbers, one for *X* and one for *Y*, are individually compared against the cumulative probabilities in Table 1, just as in Section 2.2. The 2-D grid has the same spacing Δx in both dimensions, so the diffusion steps along the *X*- and *Y*-axes are processed at the same time.

As before, the molecules are also moved by an applied electrokinetic flow, although it may have different components along the *X*- and *Y*-axes. To simulate flow, translation along each axis is applied during execution of the diffusion step. Because the speed of flow is slow in comparison to diffusion, displacement due to flow often will not amount to one grid unit per diffusion interval. Two variables store the sub-grid distances traveled in X and Y, and the positions of all molecules are updated when either of these accumulated distances exceeds one grid unit. The velocity along each axis is independent, so the flow can be applied in any linear combination of v_x and v_y such that $v_f = v_x \hat{x} + v_y \hat{y}$. When the trap is set to bring in new molecules at the beginning of the simulation and each time the simulated volume is set to flush a photobleached molecule, a constant drift velocity is simulated in the positive direction for both *X* and *Y*. When the simulation is actively trapping, the flow can be turned off or have its direction and speed

changed along each axis as photons are detected. This is described in more detail in Section 3.4.

For the parameters given in Table 5 (for one-photon excitation trapping) and Table 6 (for two-photon excitation trapping), execution of the translation step together within the diffusion step was found to result in a small speed improvement for the code. This is because scheduling a translation as a separate event sometimes requires extra memory allocations and deallocations, which are a slow operation compared to arithmetic operations. If it is desired to run a simulation with very slow diffusion or very fast translation, the code may be easily switched to run translation events separately from diffusion at any desired rate.

Entry into the simulation can occur due to diffusion or applied flow and can occur along the *X*- or *Y*-axis. Entry from diffusion along both axes is handled by a single event, but *X* and *Y* flow entries are handled as separate events, because the flow along each axis is independent. If a molecule enters due to flow, it is placed randomly along the relevant edge of the simulation with no displacement from the edge. Placement of molecules that enter due to diffusion is more complicated and is discussed below.

In the jargon of C++ programming, each molecule is an object of the Molecule Class. Entry from diffusion is handled by the constructor function of this class. Position is

Table 5. One-photon excitation trapping simulation parameters

Parameter	Square value(s)	Circular value(s)
Laser power P in each beam	75 µW	300 µW
Beam waist ω_0	1 µm	1 µm
Laser foci distance from origin / Scanning radius	1.2 ω_0	1.2 ω_0
Laser pulse spacing	3.3 ns	(continuous)
Scanning rate	76 MHz	260 kHz , 40 kHz
Absorption cross section σ_a	2×10^{-20} m^2	2×10^{-20} m^2
Fluorescence lifetime τ_f	1.2 ns	1.2 ns
Triplet lifetime τ_p	1 µs	1 µs
Grid resolution Δx	10 nm	10 nm
Diffusion coefficient D	2.2×10^{-10} m^2/s	2.2×10^{-10} m^2/s
Translation velocity	.002 m/s	.002 m/s
Concentration C	1 pM	1 pM
Feedback latency	5 µs	5 µs

Table 6. Trapping simulation parameters for two-photon excitation

Parameter	Square value(s)	Circular value(s)
Laser power P in each beam	10 mW, 30 mW	10 mW, 30 mW
Beam waist ω_0	0.5 μm	0.5 μm
Laser foci distance from origin / Scanning radius	0.5 ω_0, 1.2 ω_0	0.5 ω_0, 1.2 ω_0
Laser pulse spacing	3.3 ns	3.3 ns
Scanning rate	76 MHz	260 kHz
Absorption cross-section δ	2×10^{-20} m^4/s	2×10^{-20} m^4/s
Fluorescence lifetime τ_f	1.2 ns	1.2 ns
Triplet lifetime τ_p	1 μs	1 μs
Grid resolution Δx	10 nm	10 nm
Diffusion coefficient D	2.2×10^{-10} m^2/s	2.2×10^{-10} m^2/s
Translation velocity	.002 m/s	.002 m/s
Concentration C	1 pM	1 pM
Feedback latency	5 μs	5 μs

determined by one random number. This number determines both the side of entry (North, South, East, or West) and the distance from the edge. The edge distance may be up to five grid increments from the boundary.

In the 1-D simulation, the probability that a molecule could move onto the grid across either of the two endpoints is given by P(1-D) in Eqn. (8) in Section 2.2. For the 2-D grid, a molecule can move onto the grid in a number of different ways by crossing an edgepoint. Overall, the probability that a molecule can move onto the 2-D grid is

$$P(\text{2-D}) = 2L\,P(\text{1-D})\,, \tag{11}$$

where L is the number of grid points along each edge.

As detailed in section 2.2 in the 1-D simulation, the values Q_k for the grid points k given in Table 2 were used in comparison with a uniform random number between 0 and 1 to determine the placement of a newly entered molecule. For the 2-D simulation, this process was modified to allow entry from four edges instead of two ends. The range between Q_0 and Q_{L} was split in half to accommodate entry from the North and West edges, while the range between Q_{L} and Q_1 was split for the East and South edges. The other ranges were similarly divided, resulting in the new cumulative probabilities displayed in Table 7. N, W, E, and S represent edges along the respective cardinal directions. As for the other sets of cumulative probabilities, if a uniform random number between 0 and 1 is less than the first item in the table, then the North edge will be

Table 7. Cumulative probabilities for new entry positions in two dimensions

k	Q_k Expression	Q_k Value
N	$Q_N = Q_L/4$	0.202033299855635
W	$Q_W = Q_N + Q_L/4$	0.404066599711270
E	$Q_E = Q_W + Q_L/4$	0.606099899566906
S	$Q_S = Q_L$	0.808133199422541
$N-1$	$Q_{N-1} = Q_S + (Q_{L-1} - Q_L)/4$	0.851879186968173
$W+1$	$Q_{W+1} = Q_{N-1} + (Q_{L-1} - Q_L)/4$	0.895625174513805
$E-1$	$Q_{E-1} = Q_{W+1} + (Q_{L-1} - Q_L)/4$	0.939371162059437
$S+1$	$Q_{S+1} = Q_{L-1}$	0.983117149605069
$N-2$	$Q_{N-2} = Q_{S+1} + (Q_{L-2} - Q_{L-1})/4$	0.987183297218569
$W+2$	$Q_{W+2} = Q_{N-2} + (Q_{L-2} - Q_{L-1})/4$	0.991249444832068
$E-2$	$Q_{E-2} = Q_{W+2} + (Q_{L-2} - Q_{L-1})/4$	0.995315592445567
$S+2$	$Q_{S+2} = Q_{L-2}$	0.999381740059067
$N-3$	$Q_{N-3} = Q_{S+2} + (Q_{L-3} - Q_{L-2})/4$	0.999534067781243
$W+3$	$Q_{W+3} = Q_{N-3} + (Q_{L-3} - Q_{L-2})/4$	0.999686395503419
$E-3$	$Q_{E-3} = Q_{W+3} + (Q_{L-3} - Q_{L-2})/4$	0.999838723225595
$S+3$	$Q_{S+3} = Q_{L-3}$	0.999991050947771
$N-4$	$Q_{N-4} = Q_{S+3} + (Q_{L-4} - Q_{L-3})/4$	0.999993275776283

Table 7. Continued

$W+4$	$Q_{W+4} = Q_{N-4} + (Q_{L-4} - Q_{L-3})/4$	0.999995500604795
$E-4$	$Q_{E-4} = Q_{W+4} + (Q_{L-4} - Q_{L-3})/4$	0.999997725433307
$S+4$	$Q_{S+4} = Q_{L-4}$	0.999999950261819
$N-5$	$Q_{N-5} = Q_{S+4} + (Q_{L-5} - Q_{L-4})/4$	0.999999962696364
$W+5$	$Q_{W+5} = Q_{N-5} + (Q_{L-5} - Q_{L-4})/4$	0.999999975130909
$E-5$	$Q_{E-5} = Q_{W+5} + (Q_{L-5} - Q_{L-4})/4$	0.999999987565455
$S+5$	$Q_{S+5} = Q_{L-5}$	1.000000000000000

selected. If this random number is between two *Q* values on the chart, the outcome corresponding to the higher Q value is selected. For example, if the random number were 0.988, then *k* would be $N-2$, and the molecule would be placed two grid units inward from the North edge defining the *Y*-coordinate as two short of the upper limit of simulation.

Once an edge and a distance from the edge are selected, the position along the edge is generated by use of another call to a uniformly distributed random number. Continuing the example from the previous paragraph, the *X*-coordinate would be set between the West and East edges by a uniform random number. Overall, the algorithm ensures that molecules enter points on the grid randomly at the same rate as molecules can hop off the grid due to diffusion.

Once the position of the new molecule is determined, the entry method generates diffusion and translation events if those features are currently off. When there are no molecules present in the simulation, diffusion and translation are turned off. Finally, the entry method sets the time of future entries by use of an exponentially distributed random number with a mean for diffusion E_D and mean for translation E_T where,

$$E_D = \Delta t_D / P(\text{2-D}) \text{ and } E_T = \Delta t_F / C_0 . \quad (12)$$

3.3 Excitation and Photophysics

For both types of 2-D trap, the time of the next possible excitation event for each molecule in the simulation is re-evaluated after a molecule decays from the excited state or after it moves to a new position. The time of the next possible excitation is dependent upon the irradiance the molecule experiences at its position and whether one-photon or two-photon excitation is in use.

One-photon excitation

Simulation of the illumination of the molecule and subsequent excitation throughout the course of a run requires many random numbers. For this, matrices G_s for the square case (*S*) and G_c for the circular case (*C*) are used to map the laser intensity at the molecule's position to a pregenerated set of random numbers that specify the time for the next possible excitation event.

For the square case the laser intensity at a location (*x*,*y*) due to spot *n* at (x_n, y_n) at time *t* is given as

$$I_n(x,y,t) = \frac{2\bar{P}}{\pi\omega_0{}^2} \exp[-2((x-x_n)^2 + (y-y_n)^2)/\omega_0{}^2] \sum_j \delta(t - jT - nT/4), \qquad (13)$$

for n = 0, 1, 2, 3, where $\bar{P}$ is the laser power in each of the 4 beams, ω_0 is the laser beam waist, $\delta(t)$ represents the temporal pulse profile, which is approximately a delta distribution , and T = 13.2 ns is the period of the four-spot cycle. For each spot, the rate of one-photon excitation for a molecule in the ground state is then given by

$$k_n(x, y, t) = \sigma_a I_n(x, y, t) / E_\lambda , \tag{14}$$

where σ_a is the absorption cross-section of the molecule and E_λ is the photon energy. Multiplication of k_n by the period T yields the probability that a molecule in the ground state is excited for each laser pulse. The mean number of laser pulses from that beam before possible excitation by that beam is then $m_n(x,y,t) = \frac{1}{k_n T}$.

The elements of the G_s matrix depend on the relative intensity a molecule experiences at a displacement $(\Delta x, \Delta y)$ from a focused laser spot, where the relative intensity *RI* is a component of the intensity function defined as

$$RI(\Delta x, \Delta y) = \exp(-2(\Delta x^2 + \Delta y^2) / w_0^{\,2}) \ . \tag{15}$$

The elements of the G_s matrix are then discretized values of a single quadrant of $RI(\Delta x, \Delta y)$:

$$G_s(\Delta x, \Delta y) = \left\lfloor N_c RI(\Delta x, \Delta y) + \frac{1}{2} \right\rfloor, \text{ for } \Delta x, \Delta y \geq 0 , \tag{16}$$

where N_c = 1000 is the number of discrete integer values possible for a value of $RI(\Delta x, \Delta y)$. The addition of ½ inside the floor function brackets serves to round

$RI(\Delta x, \Delta y)$ to the nearest discrete value rather than just allow it to truncate. $G_s(|x - x_n|, |y - y_n|)$ then gives a discrete number between 0 and 1000 that depends on the discrete relative intensity at a position (x,y) due to a laser spot at (x_n,y_n).

For a molecule at (x,y), four random numbers must be generated to find the possible times of next excitation by each of the four beams. The four discrete values of $G_s(|x - x_n|, |y - y_n|)$ for $n = 0, 1, 2, 3$ then serve as indices to a two-dimensional array. Each column of this array is a set of geometrically distributed random numbers, which specify the number of laser pulses before possible excitation of the molecule experiencing the given level of irradiance. These numbers of pulses are multiplied by the laser period T to obtain the times of possible excitation by each of the spots. The lowest of these four times is the time used in simulation.

For the circular scanning case, the laser spot moves at a steady speed but is simulated as moving abruptly between 64 discrete positions. The molecule's time of next possible excitation is rescheduled for the new position and illumination after every movement of the molecule, shift of the laser spot, or after a decay event. For one-photon excitation, the laser is continuous, and the appropriate random number generator for the waiting time until the next excitation is exponentially distributed. Here the time until next possible excitation is found, as opposed to the discrete number of laser pulses until excitation. The laser intensity is given by

$$I_c(x,y,t) = \frac{2\overline{P}}{\pi\omega_0{}^2}\exp[-2((x-x_l(t))^2 + (y-y_l(t))^2)/\omega_0{}^2] \ , \tag{17}$$

with

$$x_l(t) = R\cos(\Omega t),\ y_l(t) = R\sin(\Omega t) \ , \tag{18}$$

where R and Ω are the radius angular frequency of the rotation of the beam. The rate of excitation is then given by

$$k_c(x,y,t) = \sigma_a I_c(x,y,t)/E_\lambda \ . \tag{19}$$

The elements of the matrix G_c are created differently from those of G_s and are given as:

$$G_c(\Delta x, \Delta y) = \frac{1}{k_0 RI(\Delta x, \Delta y)} \ , \text{for } \Delta x, \Delta y \geq 0 \, , \tag{20}$$

where $k_0 = \frac{2\sigma_a \overline{P}}{E_\lambda \pi\omega_0^2}$. The elements of G_c give the mean time for possible excitation for a molecule at a displacement (Δx, Δy) away from the center of the laser spot (x_l, y_l). To find the next possible time of excitation for a molecule at position (x,y) when the laser is focused at a spot (x_l,y_l), the simulation multiplies $G_c(|x-x_l|,|y-y_l|)$ by a pregenerated exponentially distributed random number with a mean of unity.

Two-photon excitation

The simulation can model either one-photon or two-photon excitation. The rate of two-photon excitation is dependent on the intensity squared and is given by

$$k^{(2)}(x,y,t) = \frac{1}{2}\frac{g_p T}{p}\delta I^2(x,y,t)\big/E_\lambda^2 , \tag{21}$$

where $I(x,y,t)$ is either $I_n(x,y,t)$ or $I_c(x,y,t)$. Here δ is the absorption cross-section for two-photon excitation, which has dimensions of $m^4 s^{-1}$ (not to be confused with $\delta(t)$, which is the temporal profile of the laser pulses), $g_p = 0.664$ is a dimensionless quantity that depends on the temporal pulse shape for the femtosecond laser pulses and has a value of 0.664 for Gaussian pulses, and $p = 100$ fs is the full width at half maximum (FWHM) temporal pulse-width. The inclusion of these factors follows Xu and Webb, and the factor of a half is because two photons are required to perform the excitation (56).

For one-photon excitation in the circular case, a continuous-wave laser is used. For two-photon excitation, a femtosecond pulsed laser with period $T = 3.3$ ns is used instead. The beam is still scanned in a circle as for one-photon excitation. Since the laser is pulsed, geometrically distributed random numbers are used in place of the exponentially distributed numbers used in one-photon excitation for the circular case. Both the circular and square traps have the mean number of pulses before possible excitation as $m^{(2)}$

$= \frac{1}{k^{(2)}T}$. The elements of the matrix $G^{(2)}$, now the same for both the square and circular configurations, are defined as

$$G^{(2)}(\Delta x, \Delta y) = \lfloor N_c R I^2(\Delta x, \Delta y) + 1/2 \rfloor. \quad (22)$$

For the square trap, the rest of the process continues as for the one-photon excitation case described above, with four geometrically distributed random numbers being generated for $m^{(2)}$ instead of m_n. The molecular relaxation pathways and other details for photon detection are still as described in section 2.3. For the circular trap, a single geometrically distributed random number is generated for $m^{(2)}$ to determine the possible time of excitation.

3.4 Trapping Behavior

Trapping algorithm for 4-beam illumination

Once a photon detection event occurs via relaxation pathway *ii* for the square case, the time of detection of the *N*-th photon t_N, divided by the laser pulse period *T*, is saved as a 32-bit unsigned integer timestamp ts_N in a binary file for later evaluation of the ACF. This integer can become larger than 32 bits allow, in which case it is wrapped. The wrapping is performed by taking ts_N = `fmod`($t_N * (T/4)^{-1}$, 2^{32}), where $(T/4)^{-1}$ is the precalculated reciprocal of *T*/4 and `fmod` is a function that returns the modulus of two

floating-point numbers. In this way the timestamp for the photon (i.e., number of laser pulses) is stored as a 32-bit integer value, and the count will start over once the maximum value is exceeded. The channel for the time-gated detection, which is the number of the laser spot that was present just before photon detection, designated as K_N, is also recorded. K_N is set equal to `fmod`$(t_N, T) * (T/4)^{-1}$.

The locations of the four spots are shown in Figure 2 on page 13. The first spot arrives at $v_0 = (x_0, y_0) = (R,0)$, the second at $v_1 = (x_1, y_1) = (-R,0)$, the third at $v_2 = (x_2, y_2) = (0,R)$, and the fourth spot at $v_3 = (x_3, y_3) = (0,-R)$, where $R = 1.2\ \omega_0$.This value is chosen for R as it was used by Cohen and Moerner (17) as a suitable value for the radius of the scan of the spot in the ABEL trap. This value is used in the circular scan of this work and is thus used in the square case as well so that the two methods may be compared under similar conditions.

For the trapping algorithm, if the laser spot at v_0 is the most recent, i.e., if $K_N = 0$ for the last detected photon, a change in flow is scheduled to move the molecule in the $-X$ direction at the maximum velocity after a delay (typically 5 μs) to account for the latency of the system. If the spot at v_1 is the most recent, i.e., $K_N = 1$, then the flow is set in the $+X$ direction Likewise, if the spot at v_2 is the most recent ($K_N = 2$), the flow is set in the $-Y$ direction, and if the spot at v_3 is the most recent ($K_N = 3$), the flow is set in the $+Y$ direction.

Trapping algorithm for circular scanning illumination

For the circular case, the flow velocity is adjusted after each detected photon, as in the square case. Here, as described in section 3.2, there are 64 discrete positions the laser spot can occupy approximating a continuously scanning laser beam. For each time of photon detection, Gaussian detector timing jitter is added, and as before, `fmod` is used to find the last active laser location: K_N is set equal to `fmod`(t_N, τ_{scan}) * $(\tau_{scan}/64)^{-1}$, where τ_{scan} = 3.85 μs is the time of a single scan of the rotating laser spot and $(\tau_{scan}/64)^{-1}$ is the precalculated reciprocal of $\tau_{scan}/64$. After a time equal to the latency of the feedback system (5 μs), the flow velocity is changed to be radially inward from the location of the laser beam at the time of detection.

Loading the trap

Although the algorithms for trapping differ for each illumination case (circular and square), the procedure used in each for loading the trap is the same. In both cases, the flow begins set to a maximum in the upper right direction. Setting the velocity this way is referred to as flushing the trap. The trap is flushed until a molecule enters the excitation volume and the photon count rate rises above a preset threshold.

To implement this in terms of the times of photon detections, a threshold time is set equal to $t_{th} = \frac{N_{th}}{5B}$, where B is the background photon count rate and N_{th} = 10 is the number of photons over which thresholding is performed. The number 5 was selected empirically. The time of each detected photon t_N is compared to the one that arrived N_{th} photons prior. If the difference in these times is greater than the threshold time, i.e., if $(t_N - t_{N-N_{th}}) > t_{th}$, then the trap is set to flush after a delay (typically 5 μs) to account for the latency of the system. If the difference in times is less than the threshold, then the flush is turned off if it is currently on, and the most recently detected photon channel number K_N is used in the appropriate trapping algorithm as described earlier in this section.

In this way, when the photon count rate drops near the level of background, the trap is flushed to bring in new molecules. When the count rate rises above the threshold, it is assumed that a molecule is fluorescing, and trapping proceeds. If the flush is set incorrectly due to statistical fluctuations in the background or a lag in fluorescence, subsequent photon detections can reset it, and trapping can continue if the molecule has not diffused too far from the excitation region.

3.5 Results and Conclusions

The performance of each type of trap was measured across a variety of parameters for one-photon and two-photon excitation. Table 5 (page 42) has the baseline parameters for simulation of one-photon excitation trapping, and Table 6 (page 43) has the same for two-photon excitation trapping. Multiple 1000 s duration experiments were simulated with variations of parameters to investigate performance. Limitations imposed by equipment such as feedback latency and background are also considered. Simulations results have provided validation for proposed and ongoing experiments and have given guidance for future work. Simulations have also allowed exploration of information not available in experiment, such as the molecular coordinates.

One-photon excitation

In Figures 6 and 7, examples of the position of a confined molecule and the photon count rate $R(t)$ are plotted versus time, while one-photon excitation trapping is active with parameters from Table 5 for the square and circular cases, respectively. The count rate is updated for each detected photon and averaged over the last $M = 10$ detected photons:

$$R(t) = \frac{M}{(t_N - t_{N-M})}, \tag{23}$$

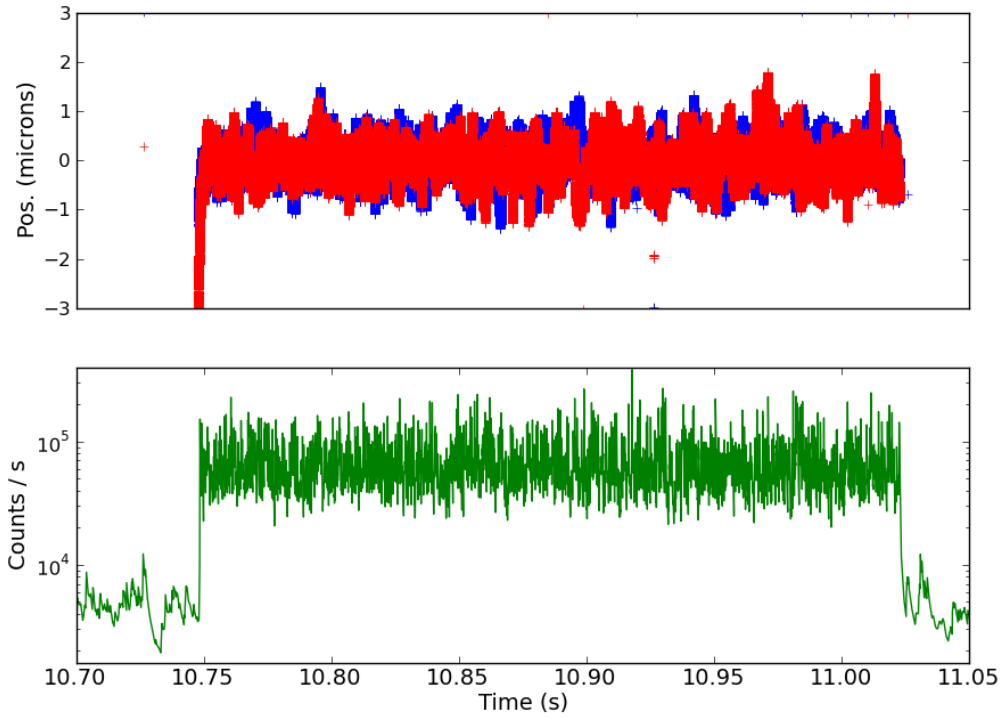

Figure 6. Example of photon count rate (green, bottom) and molecule trajectory (red: *X* coordinate, blue: *Y* coordinate) vs. time for the square trap. The stray coordinates are from other molecules entering and exiting the periphery of the simulation area while one molecule is trapped in the center.

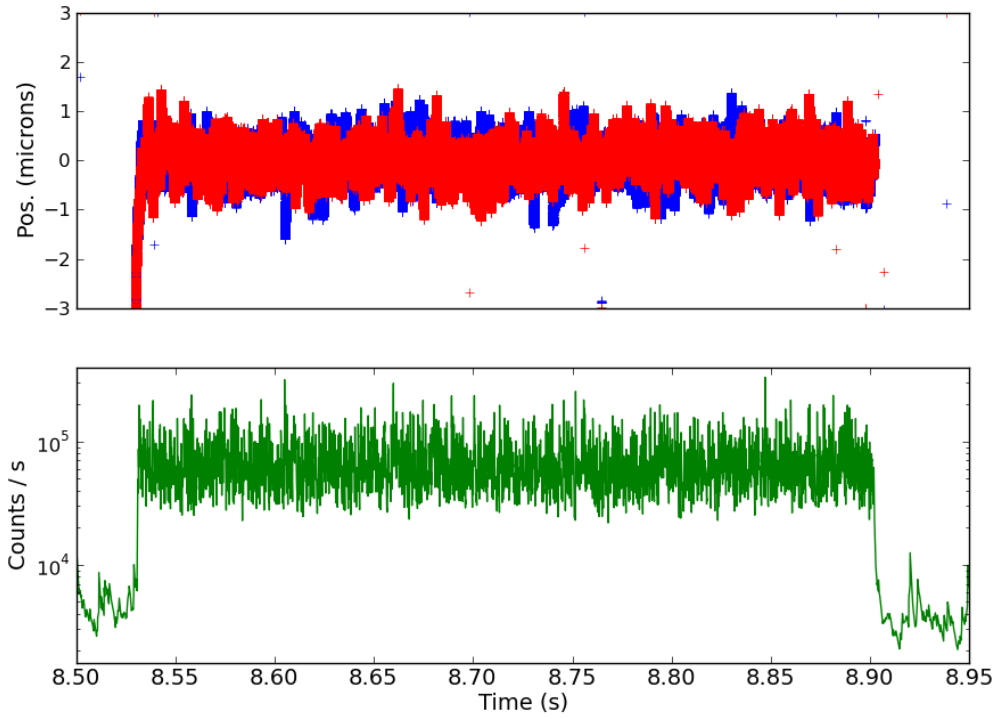

Figure 7. Example of photon count rate (green, bottom) and molecule trajectory (red: *X* coordinate, blue: *Y* coordinate) vs. time for the circular trap with scan frequency of 260 MHz.

where t_N is the time of detection of the *N*-th photon. *M* = 10 was chosen to match the thresholding in the trap's loading algorithm. In both of these figures, the count rate increases from the background level as the molecule enters the trapping region. The molecule is then held in this region until it photobleaches. Diffusion is actively corrected by modulating the electrokinetic flow. Then the molecule photobleaches and the count rate falls back down to the level of background. In both cases, the laser spots are at a radial distance 1.2 μm from the center. The molecule may move further away than this and still be actively trapped.

In Cohen and Moerner's implementation of the circular trap, they use a 40 kHz scanning frequency (27), but as stated in section 1.2, a choice of a longitudinal wave AOBD would have allowed operation at 260 kHz. To observe how this higher frequency changes the performance of the trap, both a 40 kHz and 260 kHz case are studied. Figure 7 displays data from the 260 kHz case.

Figures 8, 9 and 10 show the average number of photons collected per molecule and the average time trapped molecules survived without photobleaching versus laser power for the circular case operating at 260 kHz and 40 kHz and the square case, respectively. In these results, the 40 kHz case performs similarly to the 260 kHz case. Lower frequencies than 40 kHz were found to hinder performance (graphs not shown). A power near 90 μW yields the highest occupancy times for both the square and circular traps.

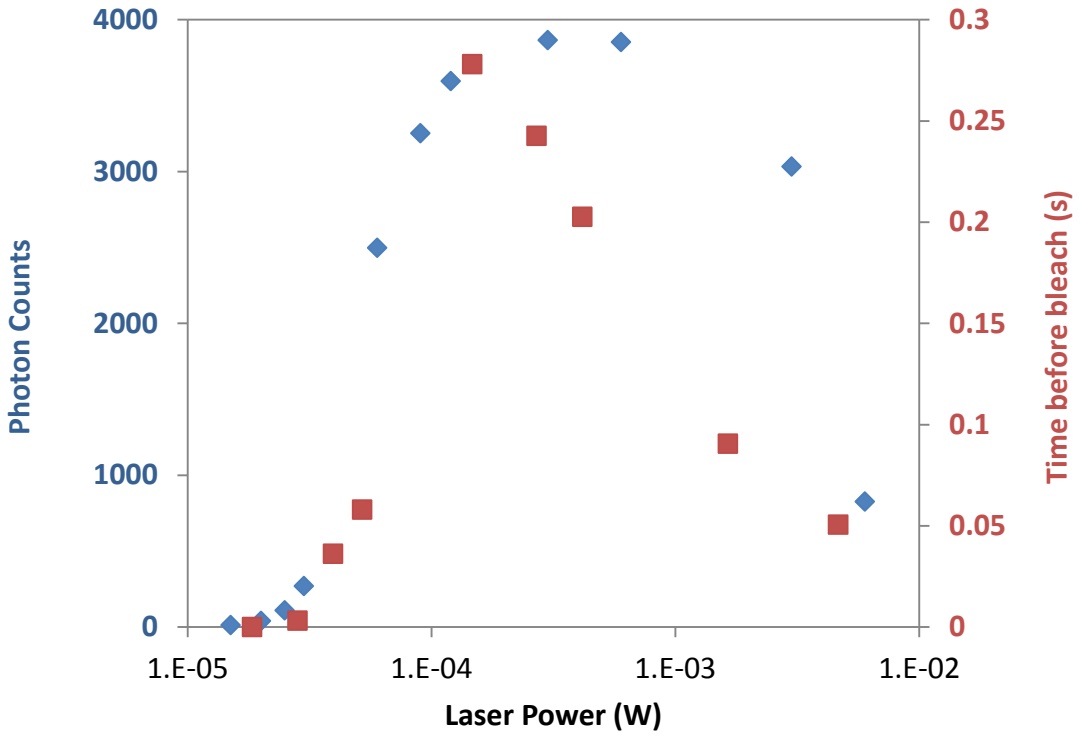

Figure 8. Average photons emitted per molecule (blue) and average time molecules remain trapped until bleaching (red) for the circular case at 260 kHz scanning frequency plotted against a variable laser power. Statistics are obtained by averaging the results of ~800–900 trapped molecules per data point.

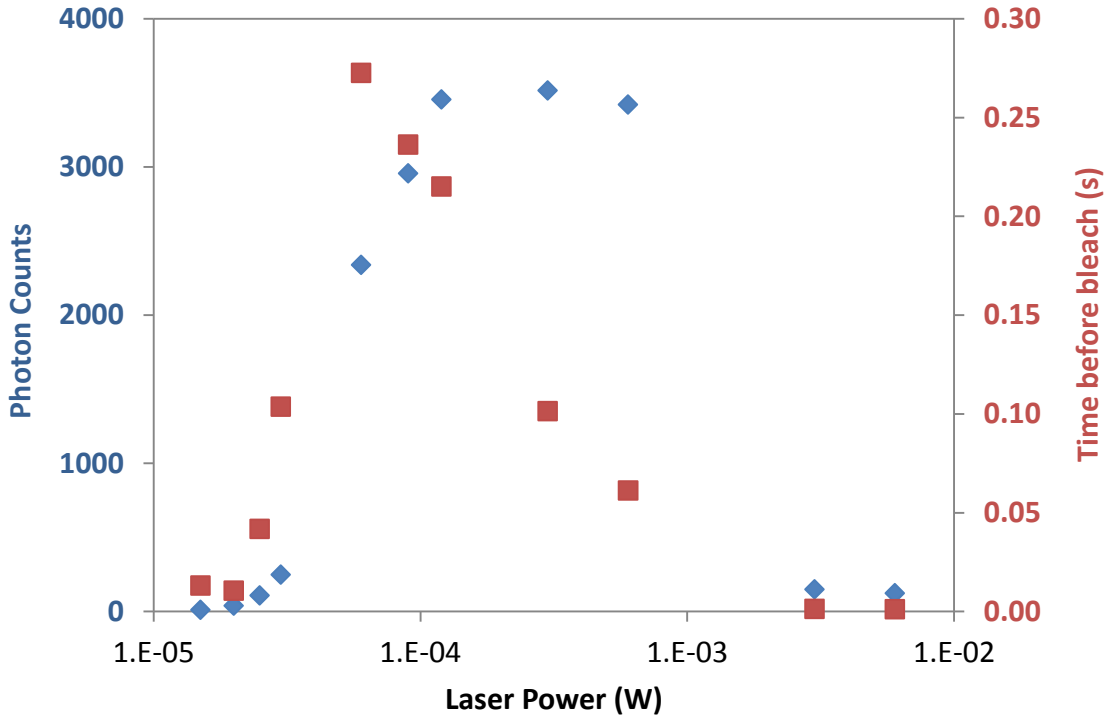

Figure 9. Average photons emitted per molecule (blue) and average time molecules remain trapped until bleaching (red) for the circular case at 40 kHz scanning frequency plotted against a variable laser power. Statistics are obtained by averaging the results of ~800–900 trapped molecules per data point.

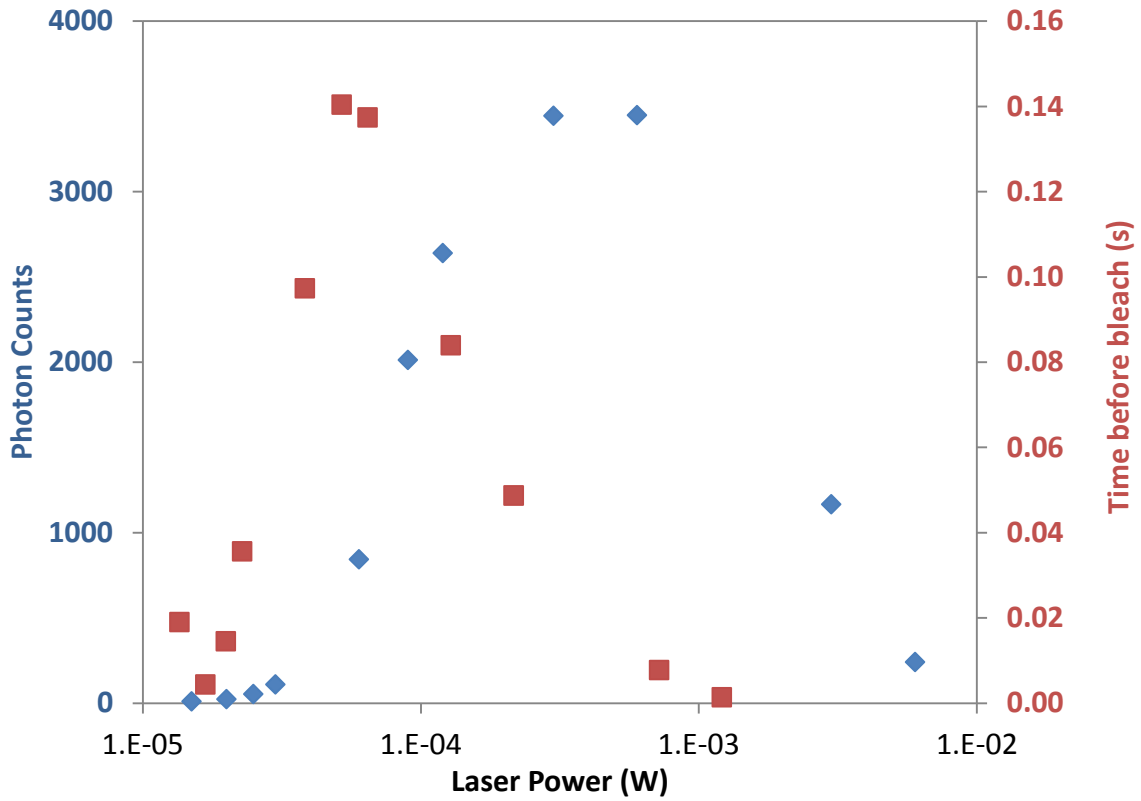

Figure 10. Average photons emitted per molecule (blue) and average time molecules remain trapped until bleaching (red) for the square case plotted against a variable laser power. Statistics are obtained by averaging the results of ~800–900 trapped molecules per data point.

The root-mean-square (RMS) deviation from the center for both the square and circular trap (both scan frequencies) is ~0.7 μm . Both types of trap are capable of holding the molecule not only within the illumination region but also well between the focal spots of the beams.

The simulation provides perfect trajectory data and molecule-by-molecule stastics that are not available in the physical experiment. Statistical analysis of the trap's performance is measured via normalized ACF $g(\tau)$ of the detected photons as it was in the one-dimensional trap as described in the papers included in the appendices. Figure 11 shows the ACF for 500-s datasets of the circular trap at 260 kHz, the square trap, and the case of no trapping respectively. There is modulation of the ACF for the circular case. This is due to the 260 kHz rate of the illumination cycle of the circular trap. At 260 kHz, the spot takes 3.85 μs to complete one cycle, and the modulation is observable in the microsecond range of the ACF. For comparison, recall that the four laser pulses in the square trap cycle every 13.2 ns, and as the fluorescence of the chosen molecule occurs in nanoseconds after excitation, there is no modulation visible for the square trap. The amplitude of the ACF is taken to be inversely proportional to $\overline{N}$, the mean number of molecules in the illumination region, and is also dependent on the signal-to-background ratio (8). The amplitudes of the trapping cases vary between individual datasets, but those seen in Figure 11 are representative of the trend.

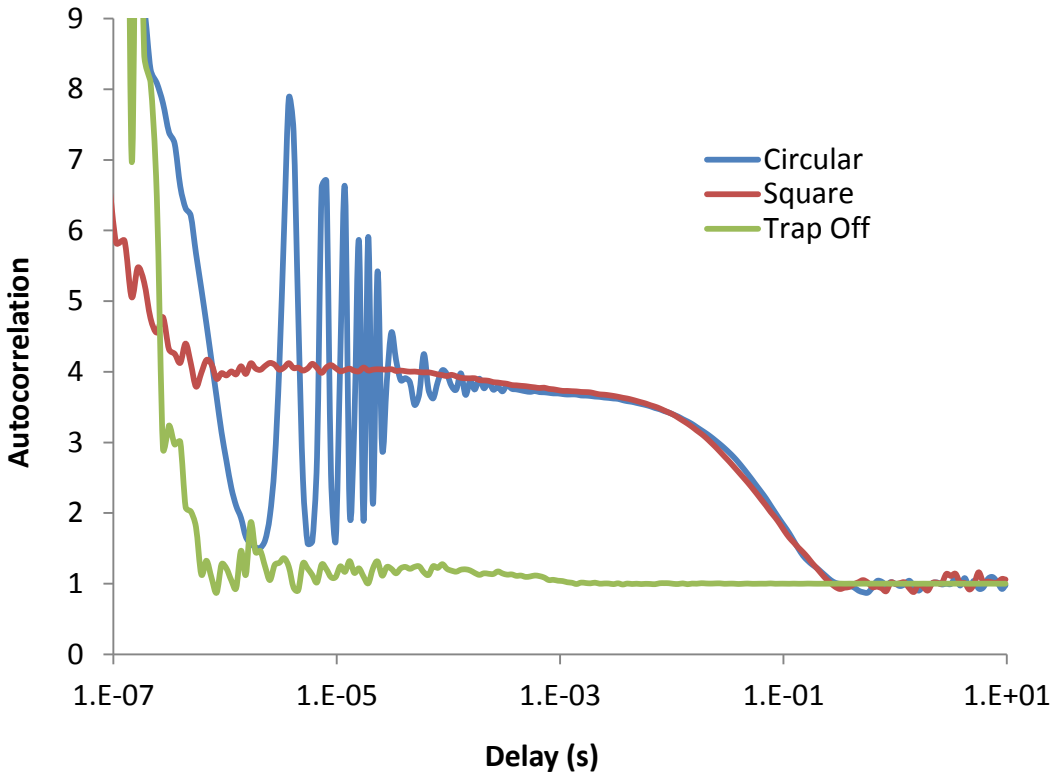

Figure 11. Autocorrelation functions for the circular trap at 260 kHz scanning frequency (blue), the square trap (red), and the case of no trapping (green).

The square trap confines molecules without modulation of the ACF, but it has a dependence on the fluorescence lifetime not found in the circular trap due to the difference in illumination cycle speeds. The square trap's illumination spot changes location every 3.3 ns. If the fluorescence lifetime of the molecule approaches or exceeeds this time, then cross-talk degrades the trapping performance. Figure 12 shows ACFs for several fluorescent lifetimes.

As another measure of the performance of the traps, time-averaged concentration profiles were recorded. Figure 13 shows a cross-sectional view of the concentration profiles of both types of trap. If it were plotted here, the concentration in the case of no trapping would be effectively constant with concentration fluctuations about 1 pM at the bottom of this figure. Figure 14 shows a 3-D view of the concentration profile of the square trap (the 3-D view of the other trapping cases look similar), while Figure 15 shows the same for the case of an inactive trap. Note that Figure 15 exhibits concentration fluctuations, which are expected for low concentrations and integration times and which form the basis of fluorescence fluctuation spectroscopy. The circular trap at 260 kHz shows a higher peak concentration due to its longer occupancy times. All profiles show a dramatic increase in the local concentration and indicate strong trapping behavior in the illumination region of the trap.

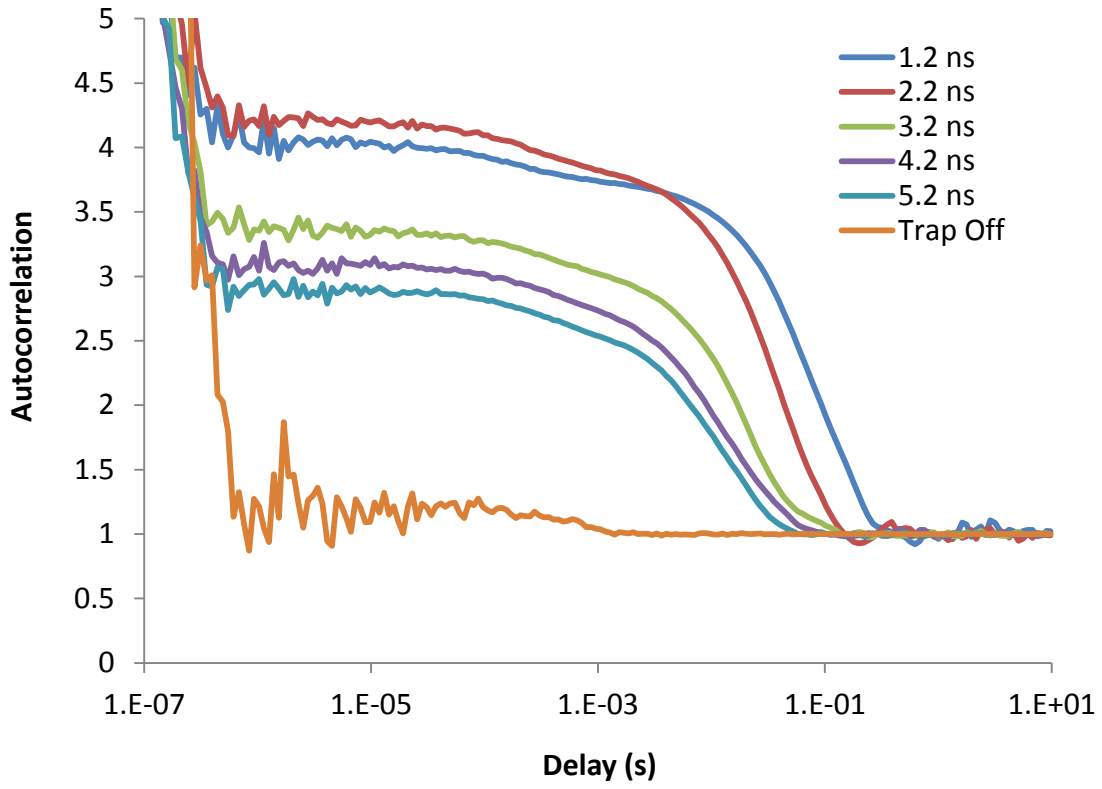

Figure 12. Autocorrelation functions for the square trap for varying fluorescent lifetime. The standard lifetime of 1.2 ns is shown in blue, and the trap still functions strongly for a lifetime of 2.2 ns but degrades quickly after. The amplitudes vary for individual datasets, but the differences in occupancy times (seen in the width of the ACF) are visible in this figure.

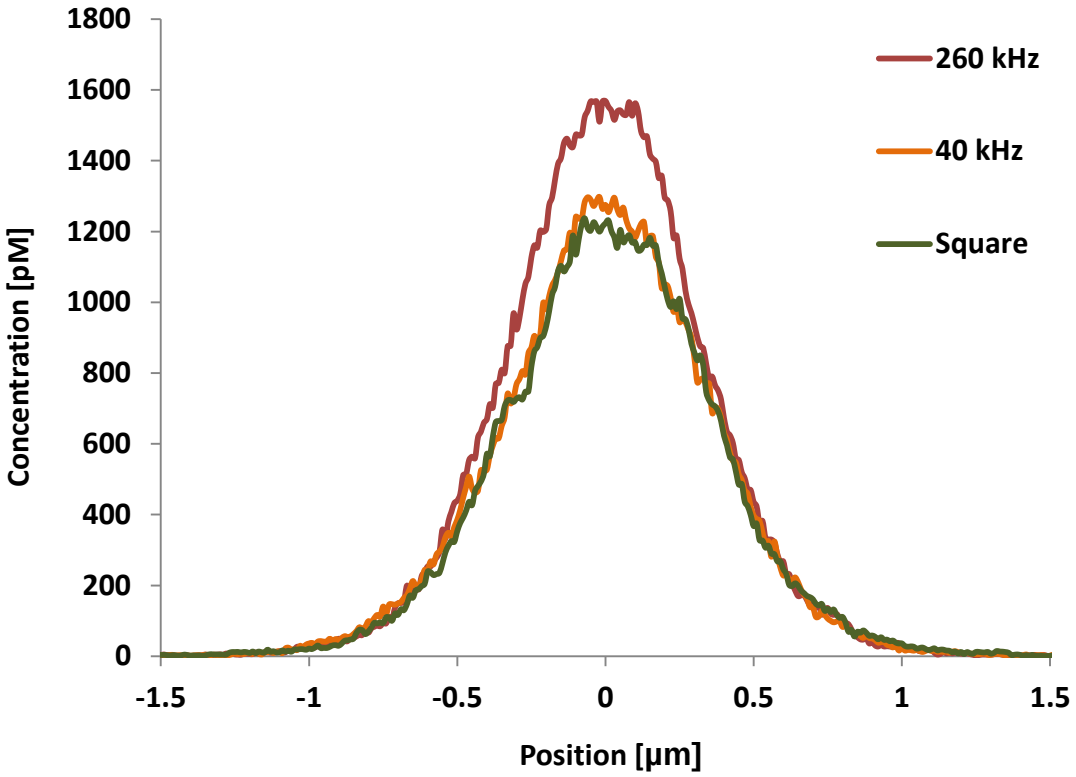

Figure 13. Cross-sectional concentration profiles along the X- axis (Y-axis looks similar) through the center of the trapping region for the square trap (green) and the circular trap at 40 kHz (gold) and 260 kHz (red).

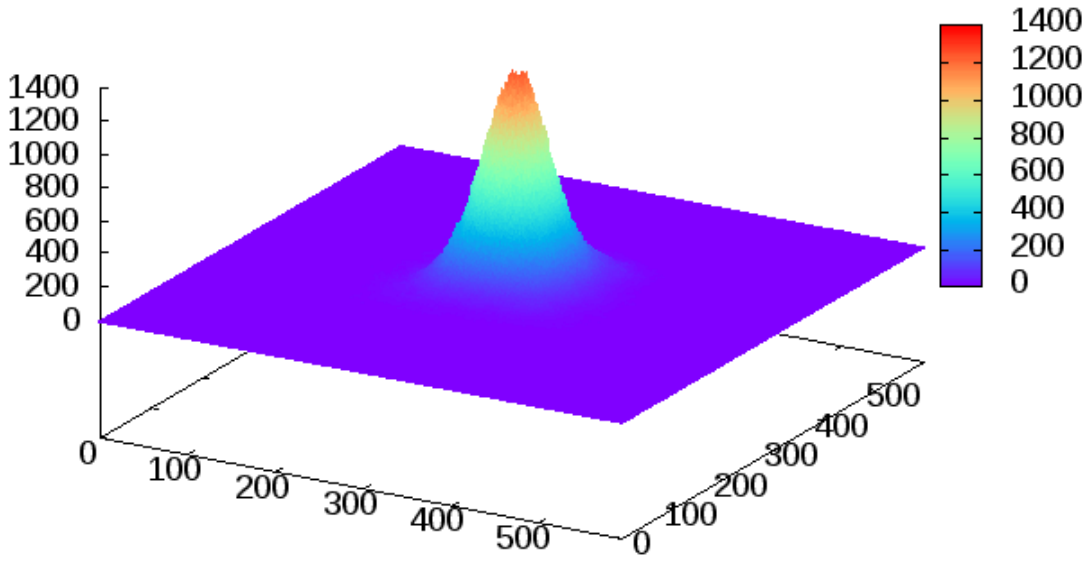

Figure 14. 3-D concentration profile for the square trap. Profile for the circular trap (260 kHz) looks similar with higher peak as seen in Figure 13.

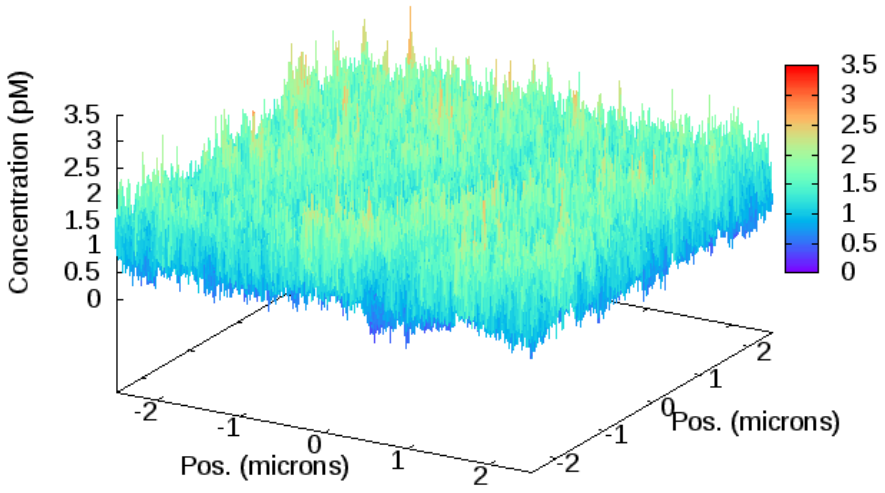

Figure 15. 3-D concentration profile for the case of no trapping.

The results show that confining a single molecule in two dimensions with one-photon excitation is viable by either of the techniques. For the square trap, occupancy times of ~140 ms are possible for molecules with short (1.2 ns) fluorescence lifetimes. For the circular case occupancy times of ~250–300 ms are possible for a trapped molecule. The previous study in a nanochannel showed possible occupancy times of 30–40 ms.

Increasing the diffusion coefficient of the molecules lessens the performance of the trap. For values of D up to 3.4×10^{-10} m^2/s, trapping does remain functional though. This value of D is representative of small dye molecules. The performance of both types of trap versus varying values of D is seen in Figure 16.

The circular trap shows longer occupancy times than the square across a variety of parameters. One possible reason for this is slower scan rate, which causes the modulation seen in the ACF. The square trap produces a more constant excitation rate, causing molecules to emit fluorescence faster and then to bleach sooner.

Two-photon excitation

Figures 17 and 18 show the trajectories of trapped molecules plotted with fluorescence count rates induced by two-photon excitation, which are calculated the same as for the case of one-photon excitation. The count rates here are higher, and the background is

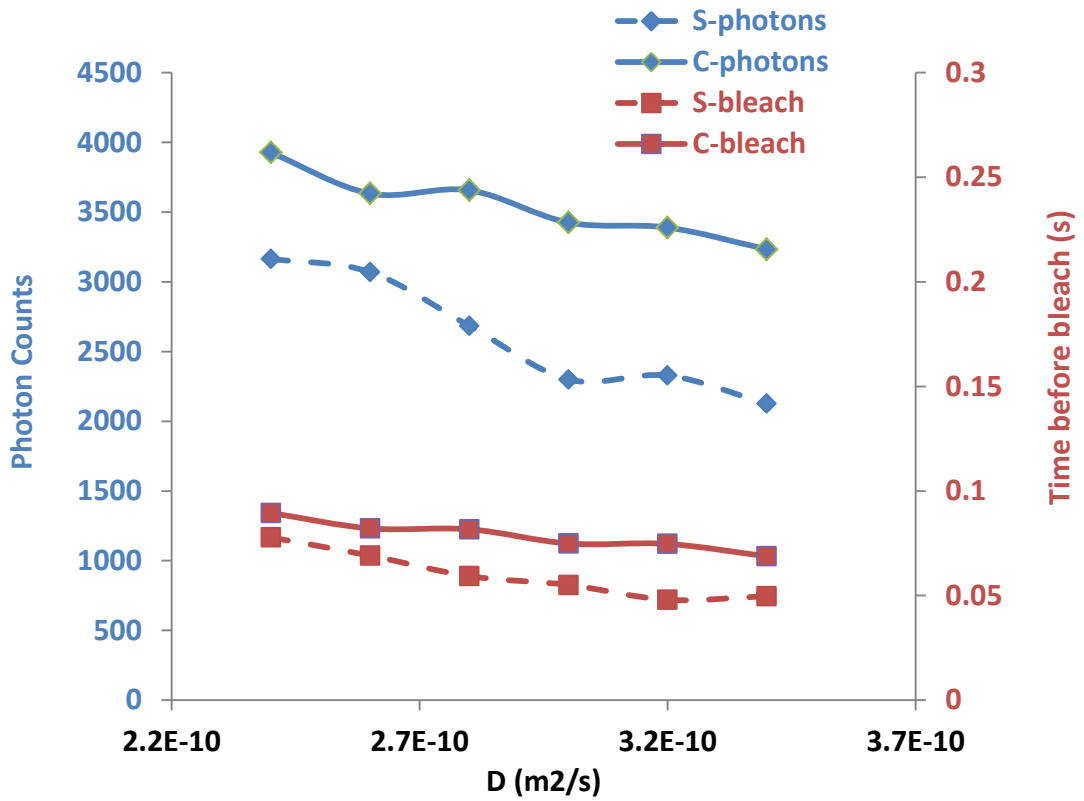

Figure 16. Average photons emitted per molecule (blue) and average time molecules remain trapped until bleaching (red) for the square (dashed) and circular (solid) cases of the trap plotted against an increasing diffusion coefficient.

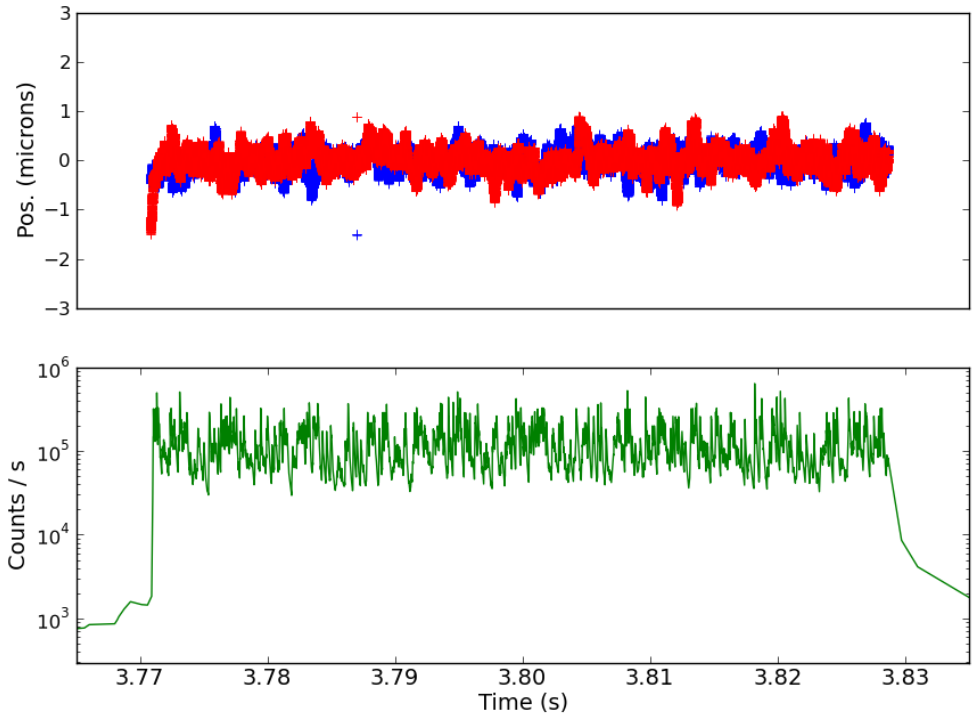

Figure 17. Example of photon count rate (green, bottom) and molecule trajectory (red: X coordinate, blue: Y coordinate) vs. time for the circular trap when using two-photon excitation.

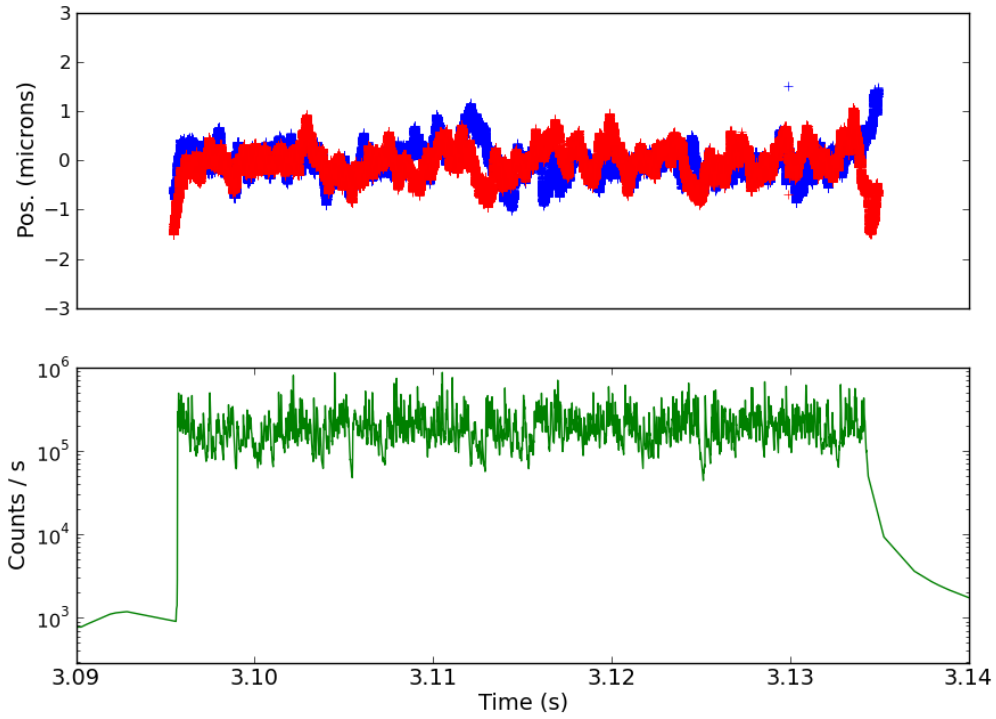

Figure 18. Example of photon count rate (green, bottom) and molecule trajectory (red: X coordinate, blue: Y coordinate) vs. time for the square trap when using two-photon excitation.

lower than when using one-photon excitation. The parameters used in these cases are recorded in Table 6 (page 43). The laser foci separation and scanning radius were initially set to 0.5 ω_0, where the beam waist ω_0 is 0.5 μm. To improve performance as discussed below, the spacing was later changed to 1.2 ω_0, and the data in Figures 17 and 18 uses this setting.

For two-photon excitation with the foci separation and scanning radius of 0.5 ω_0, trapping was not as robust as when using one-photon excitation at a diffusion coefficient of 2.2×10^{-10} m^2/s . Figure 19 shows average photons collected per moleculeand average time before bleaching versus diffusion coefficient for both types of trap.

Figure 20 shows the average number of photons per molecule and average time before bleaching for the reduced coefficient $D = 2.2 \times 10^{-11}$ m^2 /s for varying laser power. The maximum laser power that the laser can put out is the default parameter in Table 6, and we see that varying the power below this doesn't affect performance until the power drops considerably. Figure 21 shows the ACF for each type of trap when using a diffusion coefficient of 2.2×10^{-11} m^2 /s and a foci separation and scanning radius of 0.5 ω_0. The modulation shown in the ACF when using the larger scan radius of 1.2 ω_0 is mostly absent in this case.

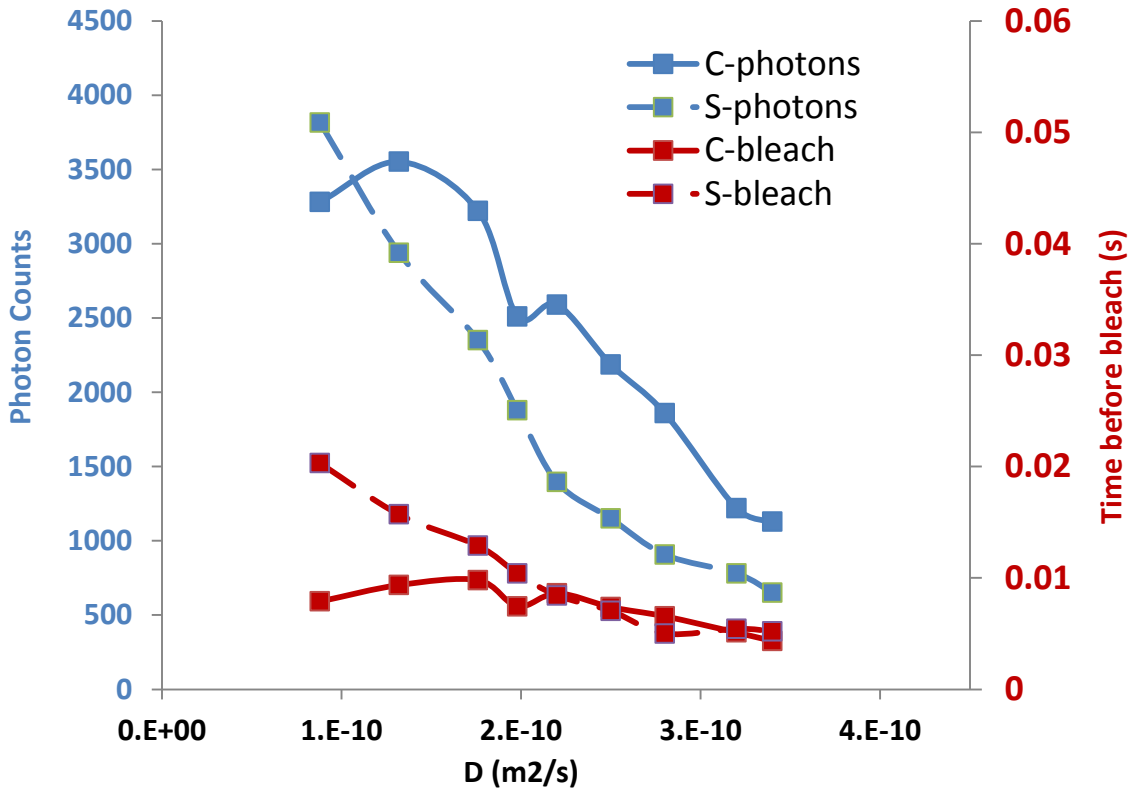

Figure 19. Average photons emitted per molecule (blue) and average time molecules remain trapped until bleaching (red) for the square (dashed) and circular (solid) cases of the trap plotted against a variable diffusion coefficient using two-photon excitation and $R = 0.5\ \omega_0$. Statistics are obtained by averaging the results of ~400 trapped molecules.

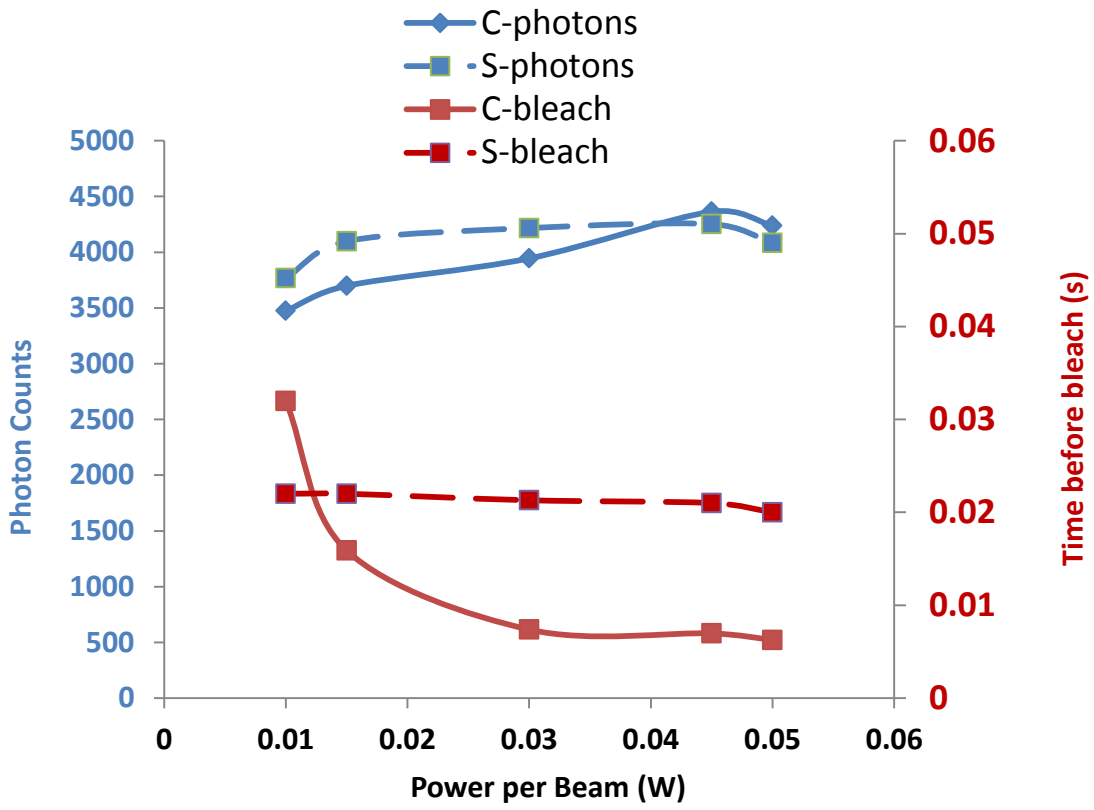

Figure 20. Average photons emitted per molecule (blue) and average time molecules remain trapped until bleaching (red) for the square (dashed) and circular (solid) cases of the trap plotted against a variable laser power using two-photon excitation and $R = 0.5\ \omega_0$.

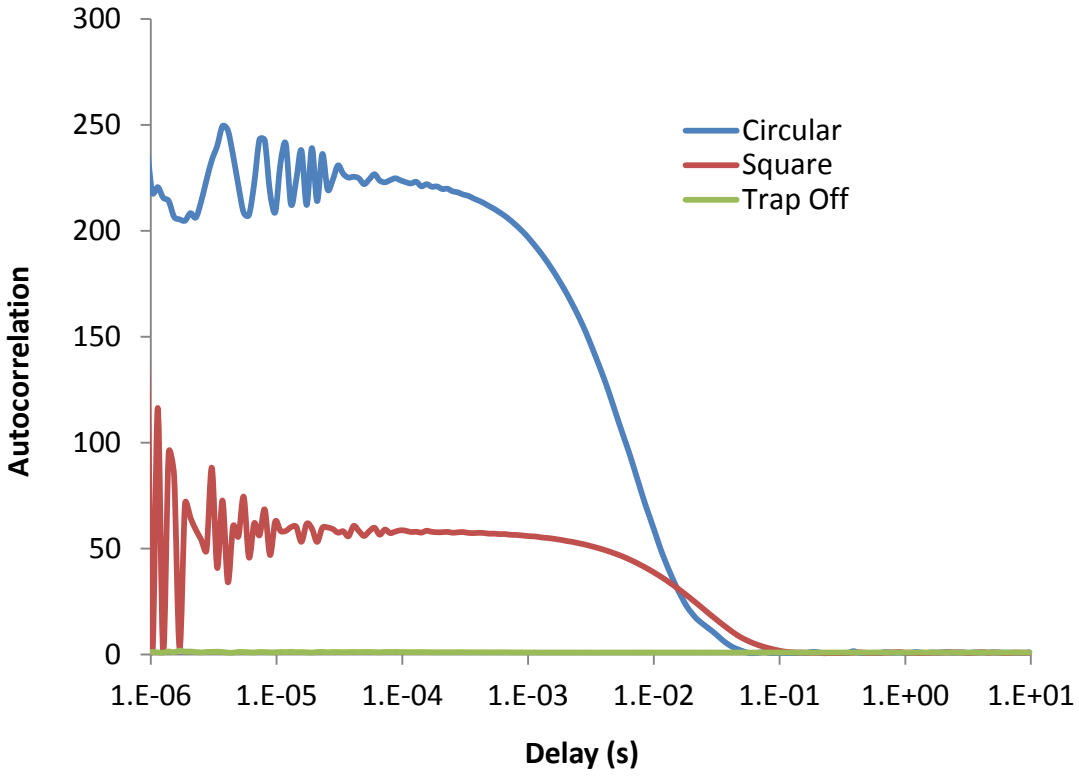

Figure 21. Autocorrelation functions for the circular trap (blue) the square trap (red), and for the case of no trapping (green, barely visible at bottom) using two-photon excitation, $D = 2.2 \times 10^{-11}$ m^2 /s, and $R = 0.5\ \omega_0$. The circular trap shows less modulation for this case than for a wider scan radius.

A reason for both the lack of modulation in the ACF of the circular trap and the inability of the traps to contain faster molecules when using two-photon excitation is the closer placement of the beams. Enlarging the beam waist for the case of two-photon excitation greatly lowers the chance of excitation, which is dependent on intensity squared instead of being linear with intensity as is one-photon excitation. However, increasing the foci separation and scanning radius to 1.2 ω_0 improves performance across a variety of diffusion coefficients as shown in Figure 22 in comparison with the results shown in Figure 19. Both traps in the case of two-photon excitation have swifter rates of bleaching than their one-photon counterparts, due to their higher count rates.

Figure 23 shows the average number of photons per molecule and average time before bleaching for a spot separation of 1.2 ω_0 and $D = 2.2 \times 10^{-11}$ m^2 /s for varying laser power. A peak in the performance was found for a power of 10 mW. Figure 24a shows the ACF for the 10 mW power, and Figure 24b shows the ACF for the 30 mW power. The lower power shows longer occupancy time with a break in the early part of the ACF, but trapping of the molecule is evident for both powers.

A cross-sectional view of the concentration profiles for the square and circular traps at a separation or scanning radius of 1.2 ω_0 and at different D values may be seen in Figures 25a ($D = 2.2 \times 10^{-11}$) and 25b ($D = 2.2 \times 10^{-10}$). For the lower diffusion coefficient, the lower powered circular trap works better than the higher powered circular trap due to

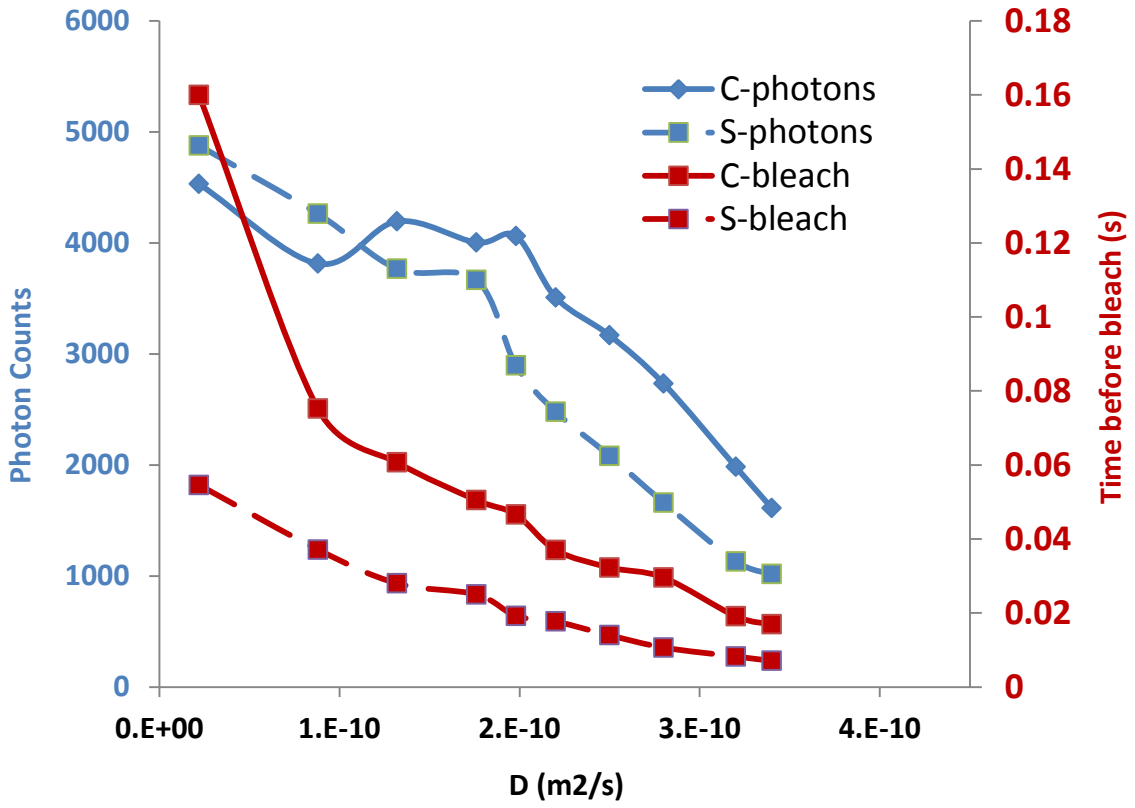

Figure 22. Average photons emitted per molecule (blue) and average time molecules remain trapped until bleaching (red) for the square (dashed) and circular (solid) cases of the trap plotted against a variable diffusion coefficient using two-photon excitation and $R = 1.2\ \omega_0$.

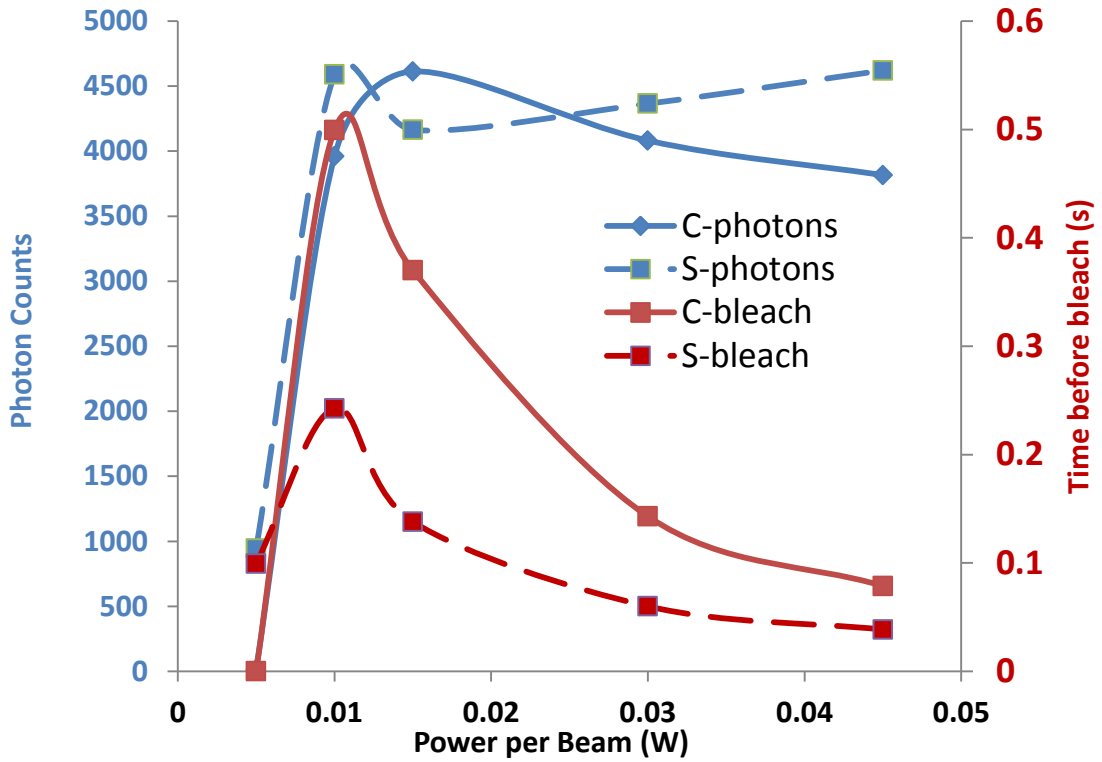

Figure 23. Average photons emitted per molecule (blue) and average time molecules remain trapped until bleaching (red) for the square (dashed) and circular (solid) cases of the plotted against a variable laser power using two-photon excitation and $R = 1.2\ \omega_0$.

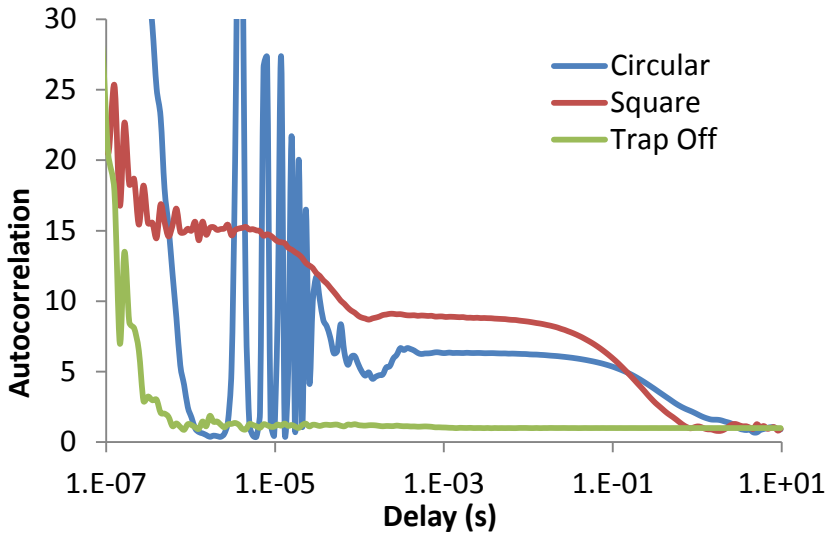

Figure 24a. ACFs for the circular trap (blue), the square trap (red), and for the case of no trapping using two-photon excitation, $D = 2.2 \times 10^{-11}$ m^2 /s, and $P = 10$ mW.

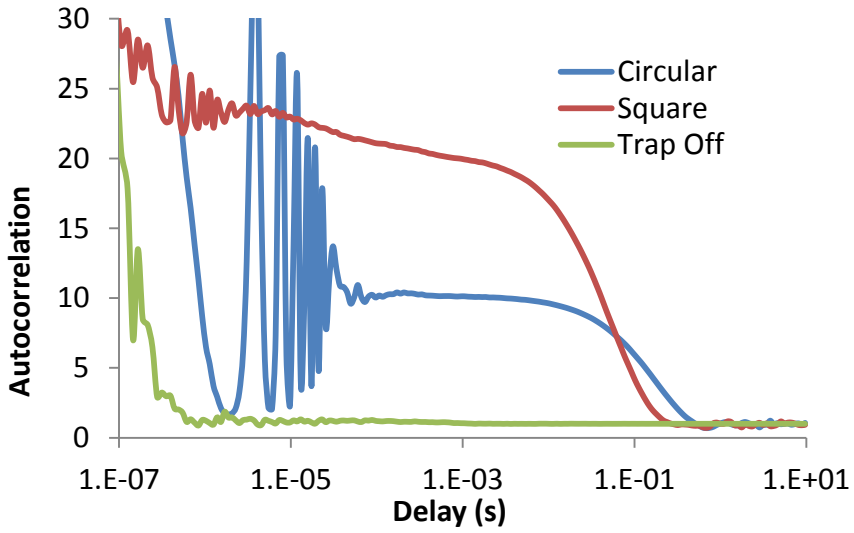

Figure 24b. ACFs for the circular trap (blue), the square trap (red), and for the case of no trapping using two-photon excitation, $D = 2.2 \times 10^{-11}$ m^2 /s, and $P = 30$ mW.

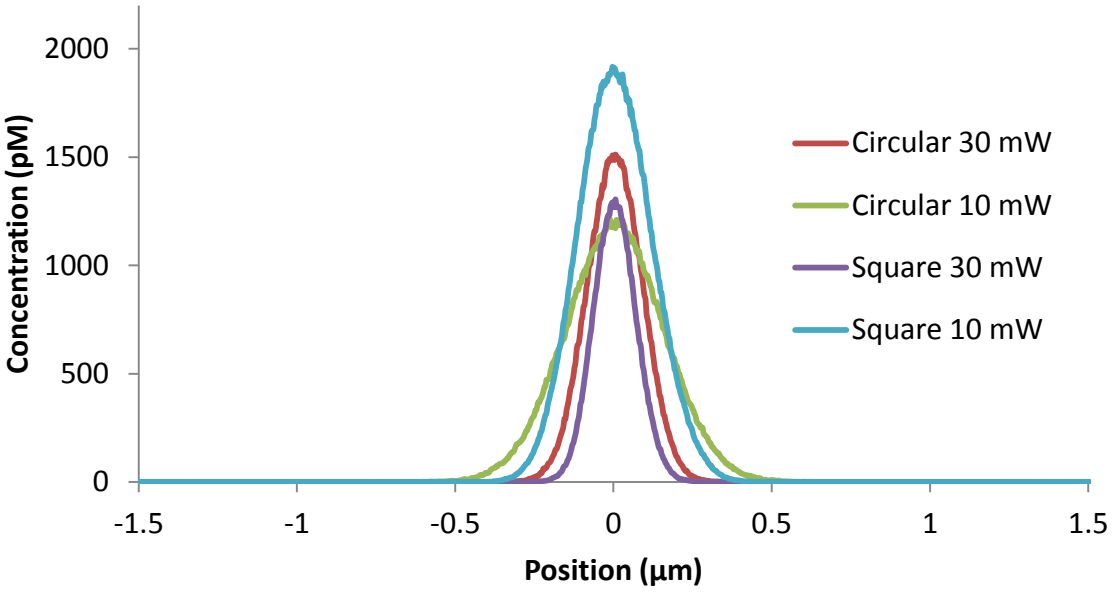

Figure 25a. Cross-sectional concentration profiles through the center of the trapping region for both types of trap at two different laser powers and $D = 2.2 \times 10^{-11}$ m^2 /s.

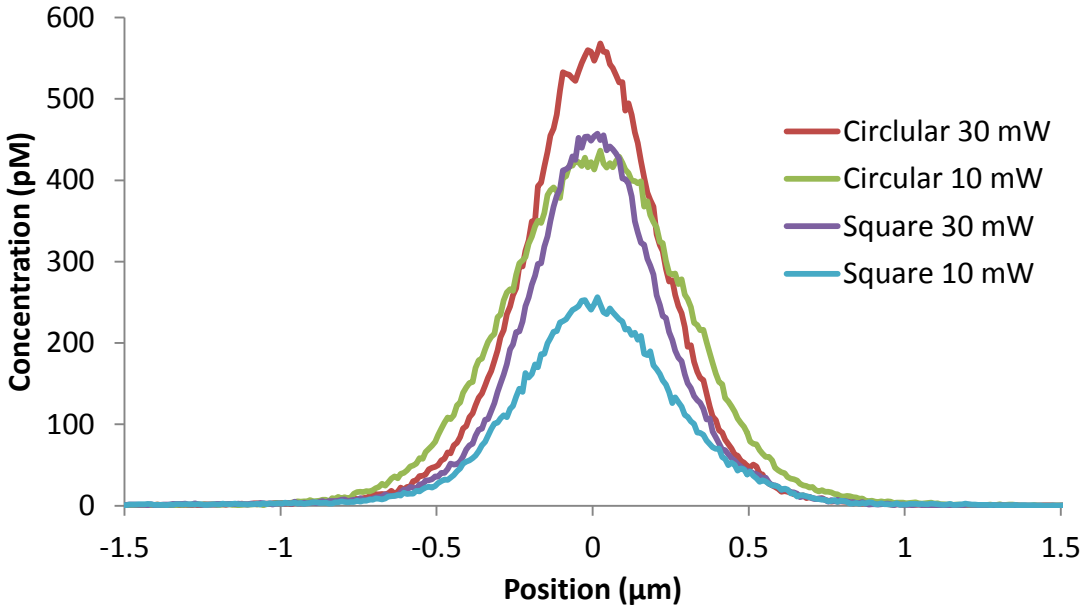

Figure 25b. As Figure 25a but $D = 2.2 \times 10^{-10}$ m^2 /s.

difference in the rate of photobleaching. With the higher diffusion coefficient, the higher powered circular trap outperforms it's lower powered counter part. For both types diffusion coefficients, the higher powered square trap outperforms the lower powered one. The case with highest peak concentration for the lower diffusion coefficient is the circular trap at 10 mW, while the square trap at 30 mW is shows the highest peak for the higher value of *D*. The molecules were contained more tightly for the slower diffusion coefficient as expected.

For two-photon excitation, trapping can work for slowed molecules with the close placement of the lasers but wider placement yields better performance. Both types of trap are capable of holding molecules until photobleaching, with the circular trap having longer occupancy times due to slower photobleaching.

In comparison with one-photon excitation, two-photon excitation trapping yields more photons per molecule and shorter occupancy times due to a higher count rate. The concentration profiles indicate tighter containment for two-photon excitation than for one-photon, because of the smaller beam waist and the dependence of two-photon excitation on intensity squared.

Chapter 4: Simulation of Single-Molecule Detection in a Microchannel with Fluorescence Detection by an EM-CCD Camera

4.1 Overview

This simulation studies single-molecule detection in a microchannel to explore the feasibility of a detection system consisting of many channels illuminated by one continuous-wave laser diode and with detection of light performed with an EM-CCD camera, rather than a SPAD. This work inherits algorithms and code from the simulations of 1-D trapping described in Chapters 1 and 2, except for modelling of the EM-CCD. Specifically, the simulation considers the flow of a solution with a concentration of 1 pM of fluorescent dye molecules through an illuminated channel with a width and depth of 1 μm and with other operating parameters given in Table 8.

Illumination is provided by a 660 nm laser diode with beam shaped by a diffractive optical element and cylindrical lenses so that it is focused to a narrow Gaussian profile with a beam waist of 1 μm along the length of the channels but has a uniform intensity across the widths of the set of channels. See Figure 3 on page 16 for a simple cartoon. The laser outputs 40 mW, and this is spread over all the channels. This simulation considers a single 1-μm-wide channel of a system consisting of 150 channels spaced over a distance of 625 μm, such that each channel recieves 64 μW.

Table 8. Screening simulation parameters

Parameter	Value(s)
Laser power $\overline{P}$	40 mW
Power per channel P	64 µW
Beam waist ω_x	1–5 µm
Absorption cross section σ_a	2×10^{-20} m^2
Fluorescence lifetime τ_f	3.0 ns
Triplet lifetime τ_p	1 µs
Grid resolution Δx	10 nm
Diffusion coefficient D	200×10^{-12} m^2/s
Concentration C	1 pM

If the ultimate goal were detection of molecules in a single channel, a SPAD would be the preferred detector; however, imaging 150 channels onto a SPAD and separating the signals is not feasible, and purchasing multiple SPADs is not cost-effective. An EM-CCD camera can be used instead to collect data from multiple channels by imaging the fluorescence from the illuminated row of channels to a single row of pixels on the detector as shown in Figure 3 (page 16). If the fluorescence output from the transit of a single molecule across the illumination zone is just a small number of photons, it would be helpful if the camera were capable of detecting single photons. It is not possible to distinguish the detection of a single photon with a conventional CCD due to the readout noise. The gain of an EM-CCD trivializes this readout noise by amplifying the photoelectron from a single photon to produce an output voltage that is above the readout noise. However, the amplification process has statistical fluctuations. More about detection with the EM-CCD is presented in section 4.3.

Many of this simulation's components are similar to those described in Chapter 2 and so are only briefly discussed here. This simulation is driven by a vector of scheduled possible events as in previous simulations. Diffusion and flow of molecules along the microchannel are simulated by use of a discrete grid in one dimension, as described in section 2.2. The same grid spacing of Δx = 10 nm is used, except when using a larger beam waist, where the grid spacing increases as $\Delta x = \omega_0 / 100$. Molecular entry and

electrokinetic flow are also simulated as described in section 2.2, although the flow remains constant as there is no trapping behavior.

As in the other simulations, when the molecule decays from the excited state, it has a chance to become excited again. This simulation features a constant irradiance profile:

$$I(x) = \sqrt{\frac{2}{\pi}} \frac{P}{\delta_y \omega_x} \exp[-2(x - x_l)^2 / \omega_x{}^2] \ , \tag{24}$$

where P is the laser power in the portion of the beam that intersects the single microchannel, δ_y is the width of the channel and ω_x is the beam waist in the dimension along the length of the channel. Here, x_l is the position of the center of the laser beam along the length of the channel. As the illumination source is continous and not pulsed, the time of the next excitation for a molecule in the ground state is determined by an exponentially distributed random number with a mean dependent on the irradiance at the molecule's current position. The rate of excitation is given by

$$k(x) = \sigma_a I(x) / E_\lambda \ . \tag{25}$$

As before, σ_a is the (one-photon) absorption cross-section and E_λ is the photon energy.

Once a molecule is excited, it has the same decay pathways with the same probabilities defined in section 2.3 and shown in Figure 4. If pathway *ii* is chosen, then the time of the photon's arrival t_N is stored to be used later in simulating the EM-CCD. Following a return to the ground state, the next excitation event is scheduled.

Background photons are also simulated. Just as in Section 2.2, they consist of detector dark counts, which for the EM-CCD are due primarily to thermally generated photoelectrons, and scattered light coming through the filters. The background rate B is again set in simulation as $B = sP + d$, which for our chosen parameters of s = 18.75 $\mu W^{-1}s^{-1}$, d = 50 s^{-1}, give B = 1250 background photons per second on average for P = 64 μW. This level of background is consistent with experimental measurements.

A SPAD detector that records the times of photon arrivals (with no noise, dead-time or afterpulsing) is simulated in comparison with the EM-CCD detector described in the next section. The raw times of photon arrival are simulated first for the entire length of simulation, and then the output from an EM-CCD detector is simulated using these generated times.

4.2 Photon Detection

The EM-CCD can be operated as a conventional CCD with no gain, wherein it has Gaussian-distributed readout noise with root-mean-square fluctuation of σ = 6 electrons when operating at 1 MHz digitization rate. This noise can obscure the fluorescence signal if the detection bin time is short so that the number of detected photoelectrons per pixel is of the order of σ = 6. Operation of the camera at 10 MHz gives a readout noise of σ = 49,

which thoroughly washes out detection of small numbers of photons when not using gain. The gain setting is discussed below.

In addition to different digitization rates and gain, the camera has two different modes of operation. In Fast Kinetics mode, the ratio of recording time to digitization time (~ 1 ms to ~ 50 ms) is not favorable, as described in Chapter 1. Further, the camera's standard software only records a single set of data at a time so that custom software (e.g., in Labview) would have to be developed to record a series of Fast Kinetics data. It is shown in the results section that the Kinetics mode has a sufficiently short bin time to detect single molecules, so this report focuses on that mode. The Kinetics mode features a 100% duty cycle. At either digitization rate, the camera's pixels are continually digitized such that the camera may record without interruption. In this mode with the 10 MHz digitization rate, the minimum bin time (i.e., the exposure time before pixels are transferred) is 122 μs. The lower digitization rate of 1 MHz may be used with a longer bin time of 1.13 ms.

Gain is used to detect a fluorescence signal despite the readout noise when using the 122 μs bin time. For this simulation, as recommended by Basden when counting single photons, the gain is set to 1000 (57). With gain on, each photoelectron is multiplied by a random exponential value with a mean equal to the gain setting. The gain register in an EM-CCD is composed of many stages, each of which provides a chance on the order of a

few percent of signal amplification through impact ionization, wherein one electron produces two. As the number of these stages becomes large, the effective signal increase becomes random with an exponential distribution. Then the random Gaussian readout noise is added to produce the output $o(t)$ of the EM-CCD camera. Here, t increases in discrete increments of time equal to the camera exposure time. After this a thresholding technique is used to convert the gain-influenced signal to photon counts.

One might expect that if gain multiplies the detected photons by 1000 on average, then division by 1000 would return the number of photons detected, but according to Basden *et al.* (57), once gain has been applied to the CCD detection signal, simple division of that signal by the gain produces extra noise. They proposed a multi-thresholding scheme for detection that has been implemented in this simulation. The cutoff threshold for detection of a single photon has been arbitrarily picked as 5σ of the readout noise. Basden's thresholds are shown in Table 9. These thresholds are a consequence of the random nature of gain. As described in his paper, for n incoming photons and with a mean gain of g, the approximate probability distribution of the detected signal is

$$p(x) = \frac{x^{n-1}\exp(-x/g)}{g^n(n-1)!}. \tag{26}$$

Gain in an EM-CCD is exponentially distributed and this can be seen for the $n = 1$ case of the above equation. The full distribution was derived by convolving the $n = 1$ case

Table 9. Threshold values for photon detection

Signal	Photons detected
< 5 σ of the dark noise	0
< 0.71 Gain	1
< 1.89 Gain	2
< 2.93 Gain	3
< 3.95 Gain	4
< 4.96 Gain	5
< 5.97 Gain	6
< 6.97 Gain	7
< 7.98 Gain	8
< 8.98 Gain	9
< 9.98 Gain	10
< 11.0 Gain	11
n Gain	*n*

with itself multiple times and then simplifying the resulting series to what is seen in Eqn. (26). The author then performs another convolution of Eqn. (26) with a Poisson distribution for a given average light level of μ photons per pixel to receive the probability of getting an output x:

$$p(x,\mu) = \sum_{n=1}^{\infty} p(x) \frac{\exp(-\mu)\mu^n}{n!}, \tag{27}$$

or

$$p(x,\mu) = \sum_{n=1}^{\infty} \frac{\exp(-\mu - x/g)\mu^n (x/g)^{n-1}}{g(n-1)!n!}. \tag{28}$$

This equation yields the contents of Table 9. As the number of photons per pixel increases, this method's results approach that of simple gain division.

Although Basden's technique for counting photons was studied as a method for detection of photon bursts from single molecules with results given in the graphs below, it was found that for most experimental parameters, the information gained was not needed. For discrimination of single molecules, it was found that a matched digital filter employed on the un-thresholded data, rather than on the photon counts from Basden's technique, allowed for best detection efficiency. Such a filter was used by Bunfield in his thesis to discern the presence of individual molecules in simulated photon bursts obtained with a SPAD detector (12). For the case at hand, the binned data or signal $o(t)$ is convolved with a Gaussian profile $w(t)$ to find the filtered signal $S(t)$. As the molecule travels through the Gaussian laser profile in the channel, its fluorescence signal is expected to be

Gaussian in time. Thus, a Gaussian function with standard deviation chosen as $\sigma_w = \omega_x/v_F$ is used as a matched filter. This fluorescence response of a molecule may be cut short by bleaching, but otherwise σ_w defines the filter's width as equal to the temporal width of the expected fluorescence signal. With the digital signal defined out to 6 σ_w in both directions, *S* is given by

$$S(t) = \sum_{t'=t-12\sigma}^{t} o(t')w(t'+6\sigma), \text{ for discrete } t \text{ and } t'. \quad (29)$$

To find a suitable threshold, *S* is averaged. Then, any data that crosses a threshold value of twice the average value of *S* is counted as part of a peak. The time corresponding to the center of a peak is checked against the times when molecules were in the simulation to confirm detection.

4.3 Results and Conclusions

This setup with parameters given in Table 8 (page 86) yields several hundred to a few thousand detectable photons per molecule, which allows a molecule to be detected above the background. Figure 26a shows the photons emitted per molecule on average versus flow velocity for several values of the beam waist. At flow velocities less than ~3×10^{-6} m/s, the diffusional motion of the molecule becomes dominant. Figure 26b shows the same data presented in a different way, the photons emitted per molecule on average versus transit time t_t, which is defined as the time it takes the molecule at its

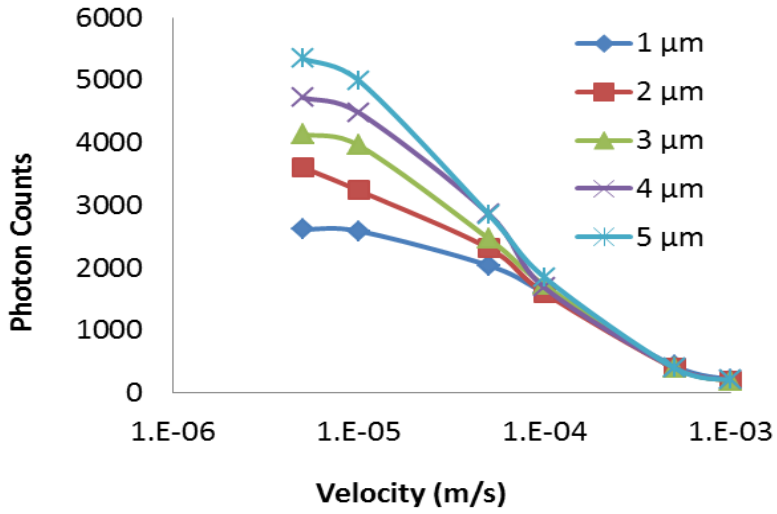

Figure 26a. Plot of average number of detected photons per molecule vs. flow velocity for several beam waists.

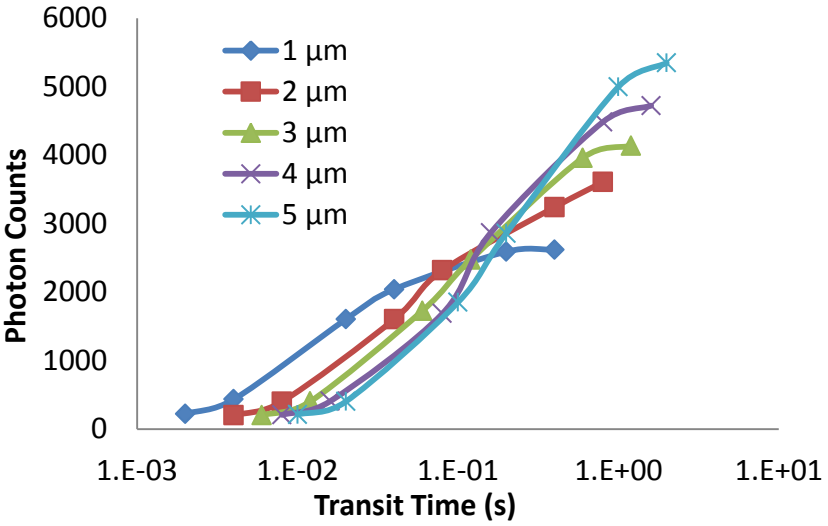

Figure 26b. Plot of average number of detected photons per molecule vs. transit time ($t_t = 2\omega_x / v_F$) for several beam waists.

current velocity v_F to move a distance equal to twice the beam waist: $t_t = 2\omega_x / v_F$. The velocity that yields the most photons per molecule is not the best for high-throughput single-molecule detection due to increased background as discussed below.

Note that for the results of Figure 26, the laser power is the same in all cases, so one might expect that the photon counts would be independent of beam waist, as the average laser intensity multiplied by the transit time is a constant. To better understand the behavior shown in Figure 26, in particular, the variation of photon counts with beam waist for slow flow velocities or long transit times, simulations were repeated with triplet crossing deactivated. Figure 27a shows the photons emitted per molecule on average versus flow velocity and Figure 27b the photons emitted per molecule on average versus transit time, with all parameters except triplet crossing the same as in Figure 26. Figure 27a shows similar results for each beam waist, indicating that the beam waist dependent behavior seen in Figure 26 is due to triplet-state saturation. Decay from the triplet state has a mean time of a microsecond, and this effective fluorescence dead time is more significant at a given velocity for a smaller beam waist, because the transit time is shorter than that for a larger beam waist. Crossing to the triplet state occurs on average once every thousand excitations, so for swifter velocities where the average number of collected photons is less, a molecule is less likely to enter this state, and the performance for different beam waists becomes similar.

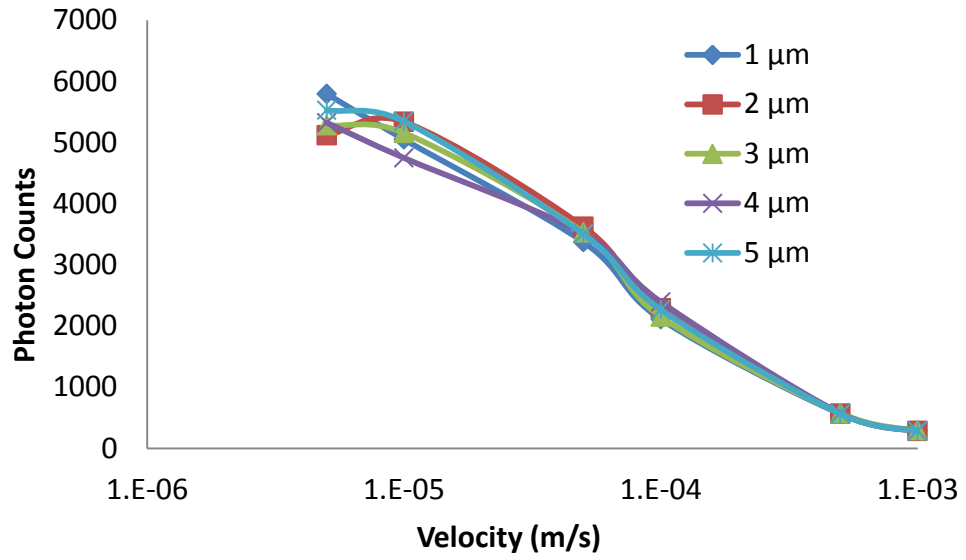

Figure 27a. Plot of average number of detected photons per molecule vs. flow velocity for several beam waists with triplet crossing deactivated.

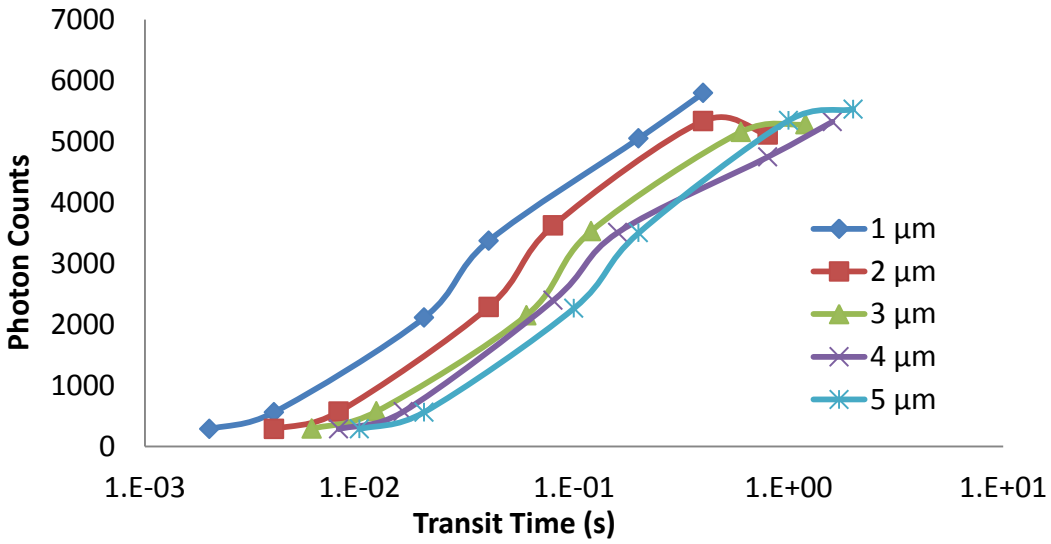

Figure 27b. Plot of average number of detected photons per molecule vs. transit time ($2\omega_x$/velocity) for several beam waists with triplet crossing deactivated.

To effectively filter the binned data, the transit time must be known, as shown in the previous section's definition of the standard deviation of the Gaussian weight function, $\sigma_w = \omega_x/v_F$. As the transit time can be experimentally determined from the ACF, a program was developed in MatLab for evaluating the ACF from simulated (or actual) camera data. Figure 28 shows that the ACF of simulated data from an EM-CCD in kinetics mode has a peak with a similar width as that from an ideal SPAD detector. Note that the autocorrelation loses information at short time delays, because of the relatively slow binning time of the EM-CCD, but the width of the peak can still be found. This demonstrates that it is possible to obtain the transit time from the ACF.

As in the work in Section 1, simulation allows observation of the molecular trajectories, which are not observed in experiment. Figure 29 shows the count rate of an ideal SPAD detector (top), photons detected by the simulated EM-CCD as determined by the thresholding method of Basden (second from top), position of a molecule in the nanochannel (third from top), and EM-CCD data filtered by Eqn. (29) (bottom). This figure shows that the EM-CCD allows for clear identification of the transit of molecules through the illumination region. For the data taken for this figure, with a flow velocity of 5×10^{-4} m/s and a concentration of 1 pM, every molecule was identified correctly from a peak in the filtered data above a preset threshold that accounts for background. Figure 30 shows a zoomed-in view of the first single-molecule transit of this same data.

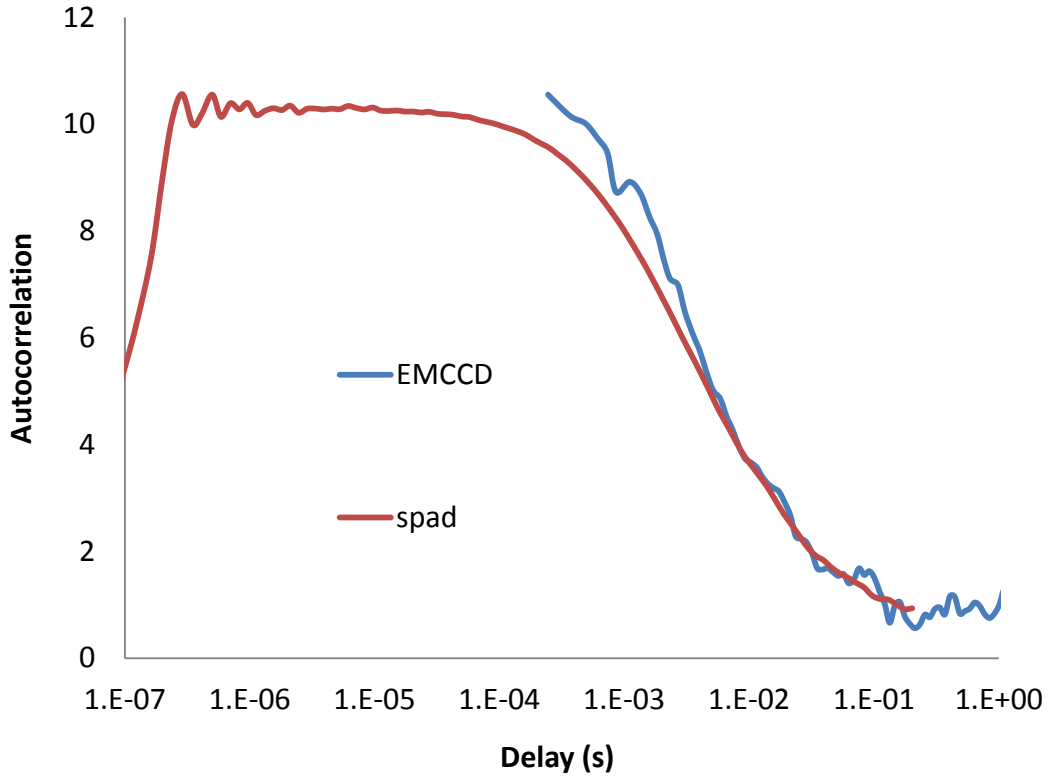

Figure 28. Autocorrelation functions from a dataset with flow velocity of 5×10^{-5} m/s and a beam waist of 1 μm using an ideal SPAD detector (red) and an EMCD with an exposure time of 122 μs.

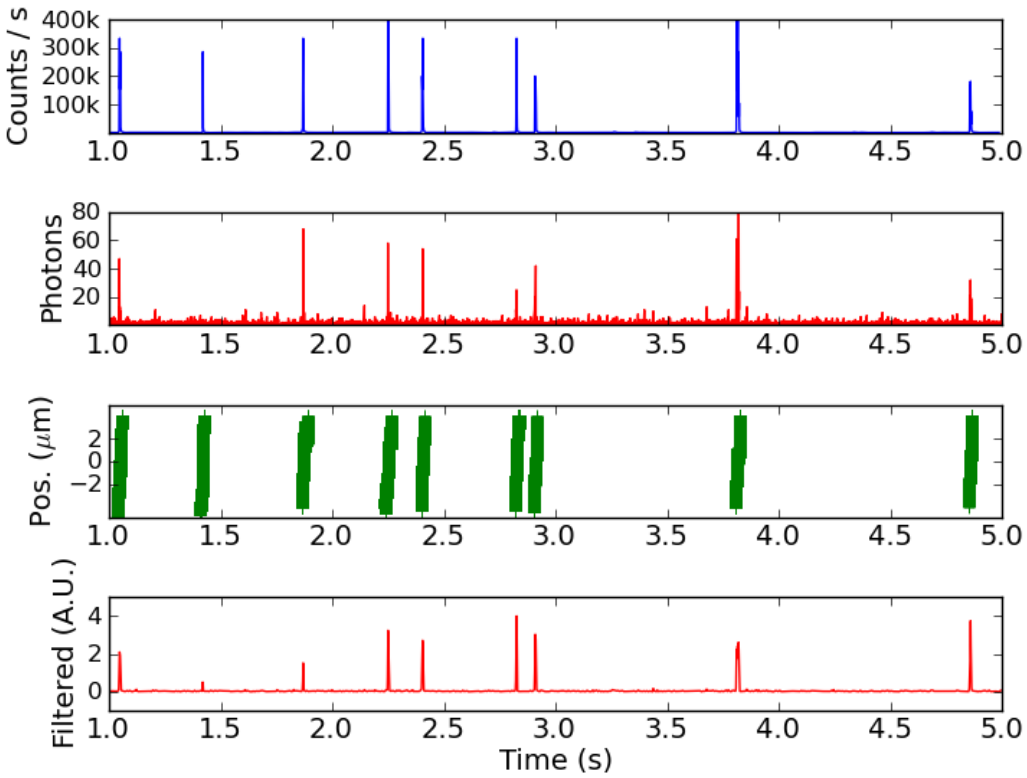

Figure 29. Plots of photon count rate (top), binned photons (2nd), molecular position (3rd), and filtered binned photons (bottom) as functions of time. The beam waist of the excitation profile is 1 μm. The count rate in the top is for an ideal detector. The detected photons in the middle are those found by using the thresholding algorithm on data from a simulated EM-CCD camera with gain of 1000.

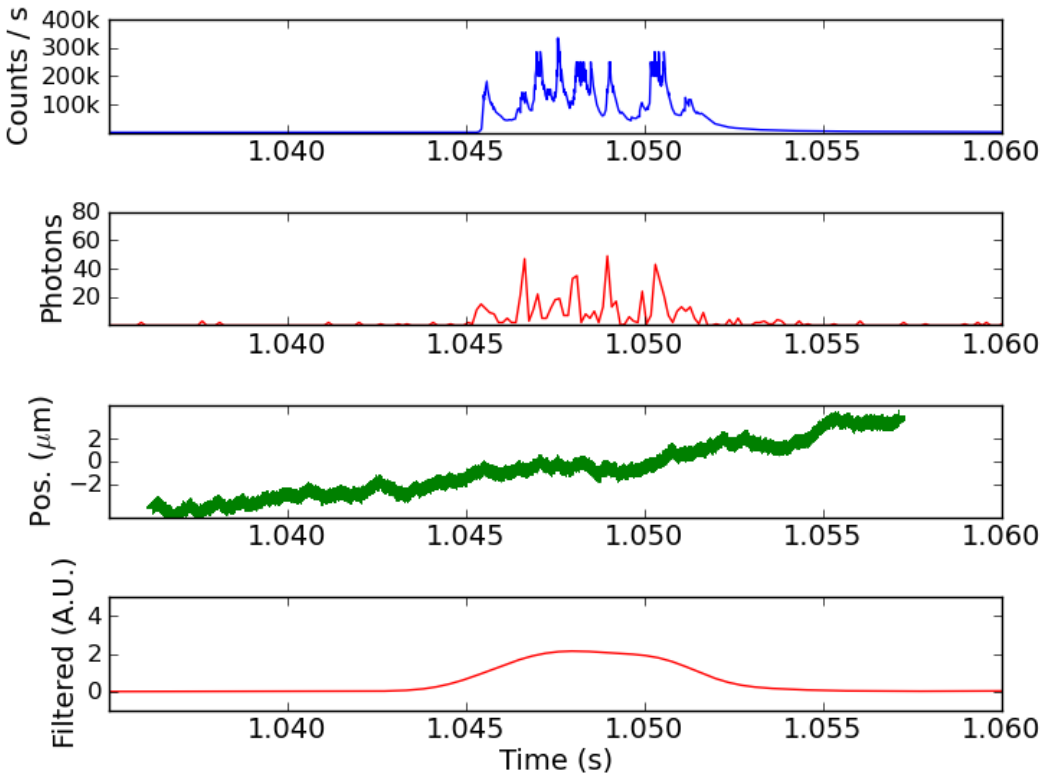

Figure 30. Plots of photon count rate (top), binned photons (2nd), molecular position (3rd), and filtered binned photons (bottom) as functions of time. These plots are a zoomed in view of the same plots presented as Figure 25. It shows a single molecular detection event.

For slower velocities, the molecule's diffusional motion can cause it to move significantly against the flow such that it can exit and reenter the region of illumination and give multiple photon bursts. Figure 31 shows two such bursts that occurred when using a velocity of 5×10^{-5} m/s and a beam waist of 5 μm. For slower velocities, the filtered signal can become unclear as molecules can produce multiple photon bursts, and more background photons may accumulate during the molecule's transit through the excitation region. The clarity of the signal can also be diminished at higher concentrations as more than one molecule may transit at the same time, resulting in overlapping peaks in the filtered signal.

Figure 32 shows the success of detection for varying velocity. Velocities between 1×10^{-4} m/s and 7.5×10^{-4} m/s allow for the detection of >95% of all molecules passing through the device with very few false detections (<5%). Velocities in the 10^{-5} m/s range allow for accurate detection of as low as 10% to as high as 50% of molecules also with very few false detections (<5%). Velocities higher than 7.5×10^{-4} m/s will show peaks in the filtered signals for most molecules but also show a high number of false peaks, with only ~2% or less of the peaks being accurate at 5×10^{-3} m/s or higher velocities.

The camera can be used with the 1 MHz readout rate and an exposure time per pixel of 1.1 ms to detect >90% of molecules when using slower velocities than with the 10 MHz readout rate. The velocities 5×10^{-4} and 1×10^{-3} m/s both allowed good detection, as

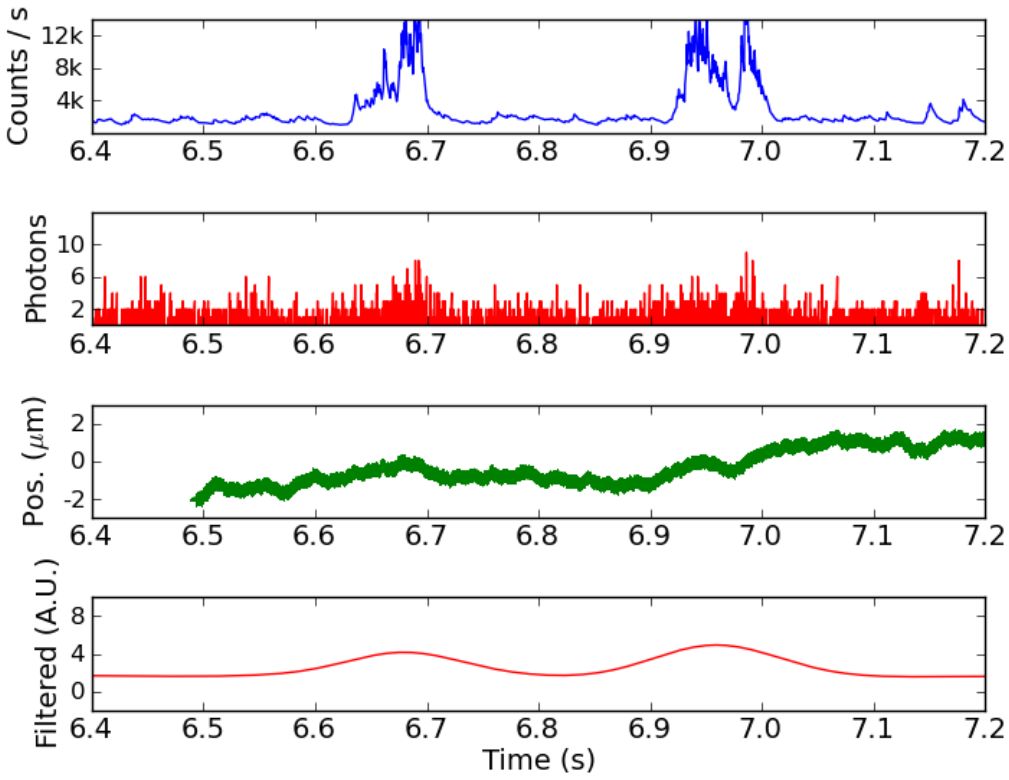

Figure 31. Plots of photon count rate (top), binned photons (2nd), molecular position (3rd), and filtered binned photons (bottom) as functions of time. Here the molecule diffuses upstream out of the region of illumination and then returns. This case was taken with a beam waist of 5 μm and a flow velocity of 5×10^{-5} m/s.

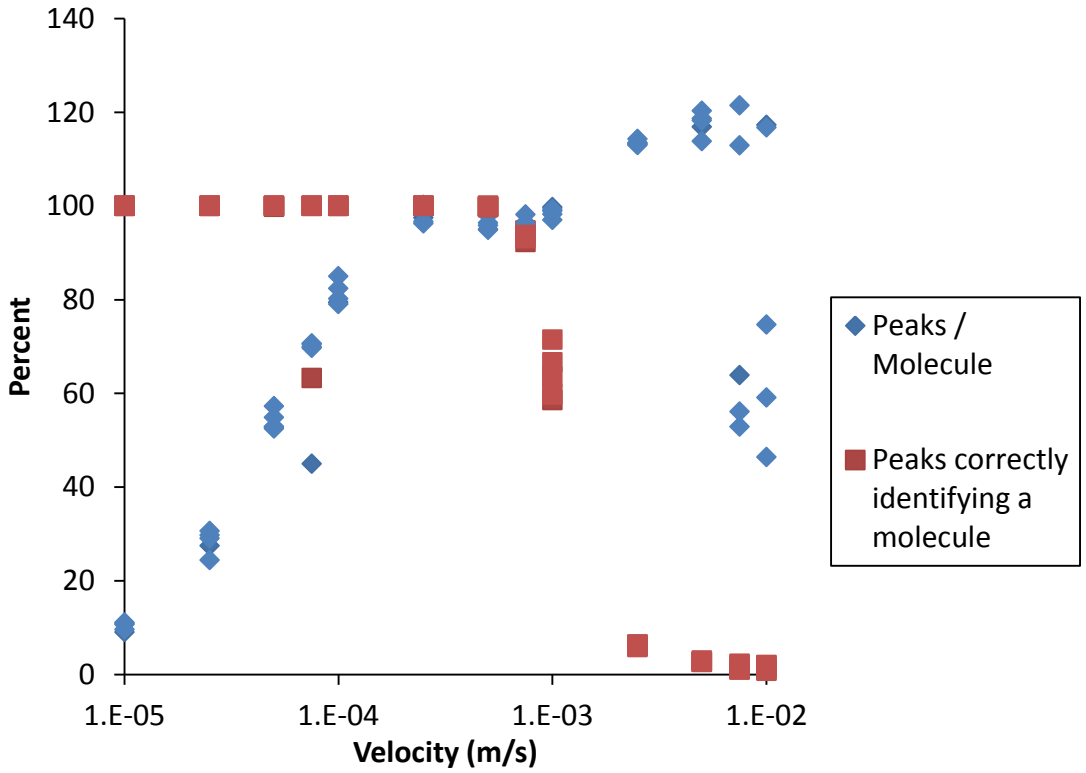

Figure 32. The blue shows the number of peaks per molecule in the filtered signal as a percentage. The percentages of peaks that correctly identify a molecule are shown in red. This data used a 10 MHz readout rate. Notice the cluster of in the middle between 1×10^{-4} and 1×10^{-3} m/s. These velocities, 2.5×10^{-4}, 5×10^{-4}, and 7.5×10^{-4} m/s, are the best for single-molecule detection in this device.

seen in Figure 33. Gain is unnecessary for these settings, and its use does not affect performance. The readout noise at this setting is 6 instead of 49 as in the 10 MHz case. At the exposure time of 1.1 ms used in the 1 MHz readout mode, the photon counts per bin are a few hundred, and the readout noise is insignificant as seen in Figure 34.

In conclusion, the results of this study provide evidence that single-molecule detection in the multi-channel device will be not only possible but also highly accurate provided that the flow velocity is set appropriately for each digitization rate: ~1–7.5 × 10^{-4} m/s for 10 MHz with gain of 1000 and between 5 × 10^{-4} and 1 × 10^{-3} m/s for 1 MHz digitization rate with no gain.

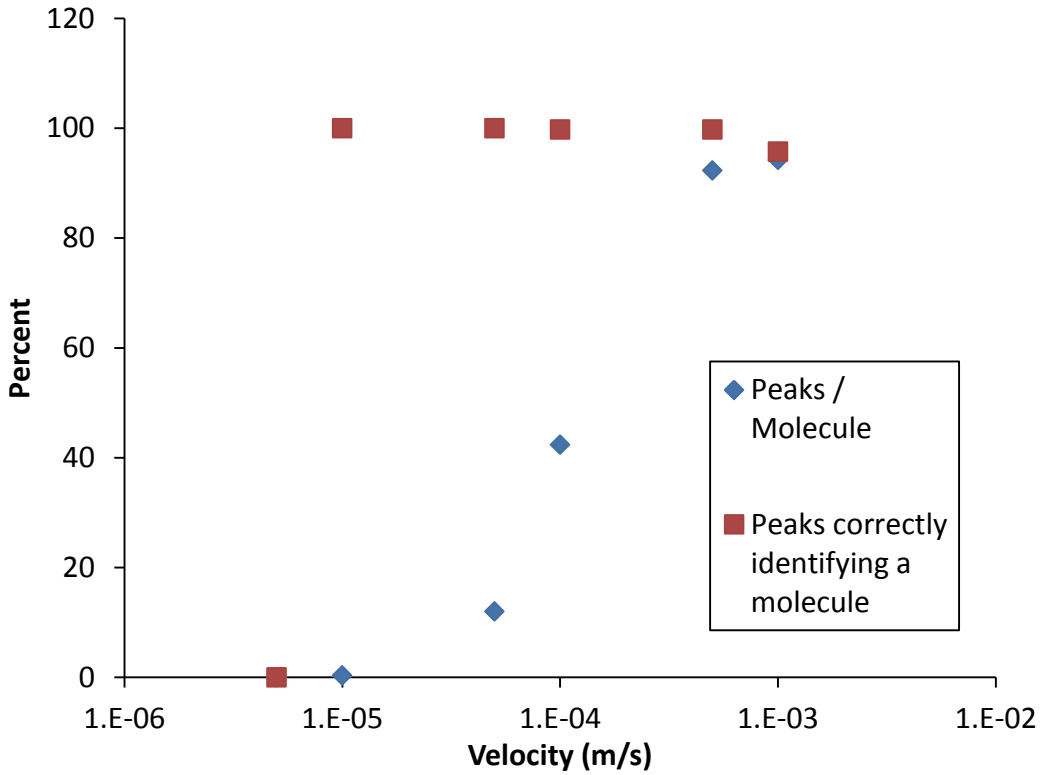

Figure 33. The blue shows the number of peaks per molecule in the filtered signal as a percentage. The percentages of peaks that correctly identify a molecule are shown in red. This data used a 1 MHz readout rate. Best performance is found at velocities of 5×10^{-4} and 1×10^{-3} m/s.

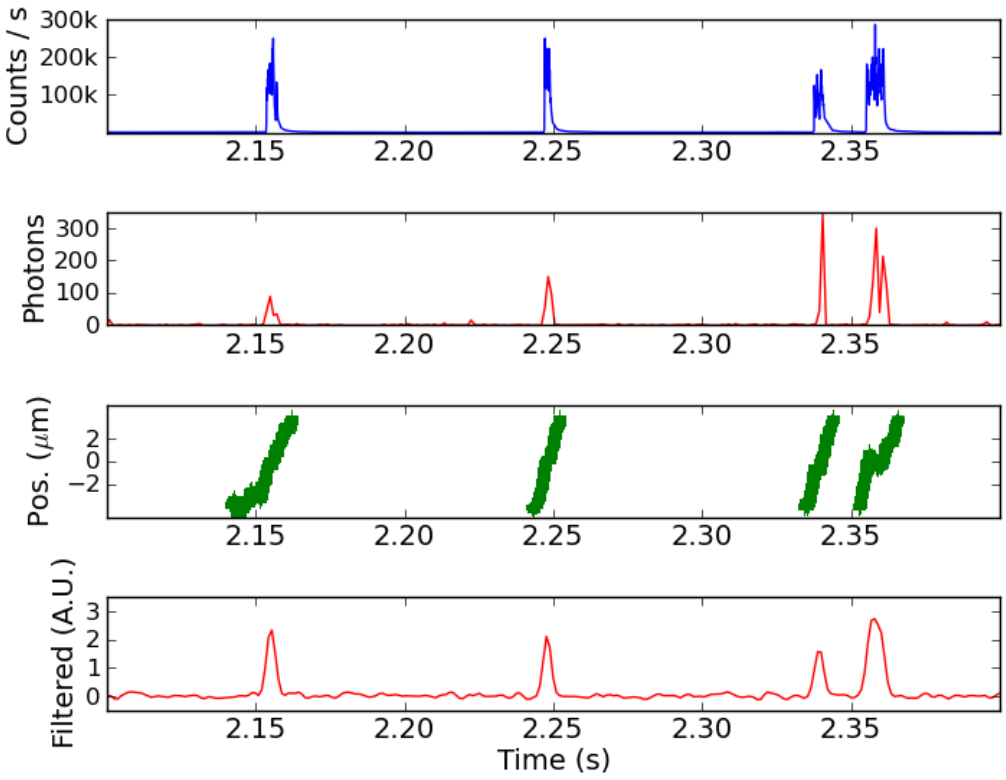

Figure 34. Plots of photon count rate (top), binned photons (2nd), molecular position (3rd), and filtered binned photons (bottom) as functions of time. Here the 1 MHz readout rate is used with an exposure time of 1.1 ms, no gain is employed, and the flow is 5×10^{-4} m/s. The noise in the binned photons is barely visible. All four molecules are successfully identified.

Chapter 5: Conclusions and Future Work

Monte Carlo simulations in the research for this dissertation have established a better understanding of single-molecule trapping in one and two dimensions. For 1-D trapping in a nanochannel, quantitative agreement with prior experimental results has been achieved using algorithms that take variable time steps to follow many interdependent physical processes over disparate timescales. Details are presented in the papers in Appendices 1 and 2. This agreement provides validation of experiments and confidence in the simulation algorithms and approximations. Simulation studies over a wider range of parameters than that used in experiments have provided insight on methods for improving future 1-D trapping experiments.

Similar algorithms have been applied to developing simulations for studying single-molecule trapping in 2-D. The results of the simulations have established that it should be possible to use a novel illumination scheme with four laser spots arranged in a square and with pulse-interleaved excitation and time-gated single-photon counting to achieve stable single-molecule trapping. With this illumination, trapping times and photon yields are similar to those obtained by the conventional illumination method, which uses a single laser focus that scans in a circle at 40-240 MHz, obtained by use of a pair of acousto-optic modulators. Simulations have studied both one-photon or two-photon excitation: Both types of trap, either square or circular, with either one- or two-photon excitation can

contain a single molecule until photobleaching occurs, typically several hundreds of milliseconds. One of the challenges for future trapping work is exposing molecules to a level of irradiance and using the resulting fluorescence in such a way that tightens molecular containment and maintains or improves the rates of photobleaching. Future laboratory work will involve creating a setup to trap single fluorescently-labeled molecules in 2-D with the square setup, being guided by the findings of this dissertation.

The algorithms developed in this research can be extended to develop simulations for studying single-molecule trapping in 3-D. Both simulations and laboratory experiments are planned for the study of trapping in 3-D using two-photon excitation due its compressed excitation volume. Molecules in nanochannels have been observed to stick over time, and the rate of collision with the surfaces of 1- and 2-D traps are in the thousands per second. 3-D trapping would provide manipulation of molecules without either of these undesirable effects.

Similar algorithms to those used in simulating trapping in a nanochannel are also used in simulation of single-molecule detection with an EM-CCD camera. It has been shown that good identification of molecules through use of a matched filter should be possible in experiment. These results are obtainable through use of a short exposure time of 122 μs and gain for flow velocities between 1×10^{-4} m/s and 7.5×10^{-4} m/s or by use of a 1.1 ms exposure time with no gain and flow velocities between 5×10^{-4} and 1×10^{-3} m/s.

A multichannel device is currently in use in our lab to perform parallel single-molecule detection. Future work will involve the creation of swifter computational techniques to better process the data collected from hundreds of channels. In particular, the autocorrelation functions require a long time to calculate when studying long datasets from hundreds of channels.

LIST OF REFERENCES

1. E. B. Shera, N.K. Seitzinger, L.M. Davis, R.A. Keller, and S.A. Soper, "Detection of single fluorescent molecules," Chemical Physics Letters 174 (6), 553–557 (1990).

2. D. H. Bunfield and L.M. Davis, "Monte Carlo simulation of a single-molecule detection experiment," Applied Optics 37, 2315–2326 (1998).

3. L. M. Davis, J. G. K. Williams, and D. T. Lamb, "Computer simulation of gene detection without PCR by single-molecule detection," Proc. SPIE 3570, 282–293 (1999).

4. T. Wohland, R. Rigler, and H. Vogel, "The standard deviation in fluorescence correlation spectroscopy," Biophys. J. 80, 2987–2999 (2001).

5. "Photodynamics and time-resolved fluorescence of azobenzene in solution: A mixed quantum-classical simulation," T. Cusati, G. Granucci, and M. Persico, J. Am. Chem. Soc., 133 (13), 5109–512 (2011).

6. "Characterizing the unfolded states of proteins using single-molecule FRET spectroscopy and molecular simulations," K. A. Merchant, R. B. Best, J. M. Louis, I. V. Gopich, and W. A. Eaton, Proceedings of the National Academy of Sciences 104 (5) 1528–1533 (2007).

7. G. Shan and W. Huang, “Extracting the single-molecule fluorescence trajectories of folding protein in single-pair fluorescence resonance energy transfer experiment,” Journal of Nanoscience and Nanotechnology 9 (2) 1176–1180 (2009).

8. L. M. Davis, P. E. Williams, D. A. Ball, E. D. Matayoshi, and K. M. Swift, “Data reduction methods for application of fluorescence correlation spectroscopy to pharmaceutical drug discovery,” Curr. Pharm. Biotechnol. 4, 451–462 (2003); 5, 481–481 (2004).

9. L. M. Davis and G. Q. Shen, “Accounting for triplet and saturation effects in fluorescence correlation spectroscopy measurements,” Curr. Pharm. Biotechnol. 7, 287–301 (2006).

10. J. Enderlein, “Tracking of fluorescent molecules diffusing within membranes,” Applied Physics B: Lasers and Optics 71, 773–777 (2000).

11. Q. Wang and W. E. Moerner, "Optimal strategy for trapping single fluorescent molecules in solution using the ABEL trap," Applied Physics B 99, 23–30 (2010).

12. D. Bunfield, “Simulation of a Single-Molecule Detection Experiment,” Master’s Thesis, The University of Tennessee, (1997).

13. Y. Sun, “Analysis of Ultra-sensitive Fluorescence Experiments,” Ph.D. Dissertation, The University of Tennessee, (2000).

14. W. N. Robinson, “Simulation of Single-Molecule Trapping in a Nanochannel,” Master’s Thesis, The University of Tennessee, (2008).

15. P. R. Selvin and T. Ha, Single-Molecule Techniques: A Laboratory Manual, Cold Spring Harbor Laboratory, (2008).

16. L. M. Davis, B. K. Canfield, X. Li, W. H. Hofmeister, I. P. Lescano-Mendoza, B. W. Bomar, J. P. Wikswo, D. A. Markov, P.C. Samson, C. Daniel, Z. Sikorski and W. N. Robinson, “Electrokinetic delivery of single fluorescent biomolecules in fluidic nanochannels,” Proceedings of SPIE 7035, 70350A 1–12 (2008).

17. A. E. Cohen and W. E. Moerner, “Controlling Brownian motion of single protein molecules and single fluorophores in aqueous buffer,” Optics Express 16, 6941–6956 (2008).

18. A. J. Berglund and H. Mabuchi, “Tracking-FCS: Fluorescence correlation spectroscopy of individual particles,” Optics Express 13, 8069–8082 (2005).

19. A. J. Berglund and H. Mabuchi, “Performance bounds on single-particle tracking,” Applied Physics B 83, 127-133 (2006).

20. V. Levi, Q. Ruan, M. Plutz, A. S. Belmont, and E. Gratton, “Chromatin dynamics in interphase cells revealed by tracking in a two-photon excitation microscope,” Biophysical Journal 89, 4275-4285 (2005).

21. V. Levi and E. Gratton, “Exploring dynamics in living cells by tracking single particles,” Cell Biochemistry and Biophysics 48, 1–15 (2007).

22. G. A. Lessard, P. M. Goodwin, and J. H. Werner, “Three-dimensional tracking of individual quantum dots,” Applied Physics Letters 91, 224106 (2007).

23. N. P. Wells, G. A. Lessard and J. H. Werner, “Confocal, three-dimensional tracking of individual quantum dots in high-background environments,” Analytical Chemistry 80, 9830–9834 (2008).

24. W. A. Lyon and S. M. Nie, “Confinement and detection of single molecules in submicrometer channels,” Analytical Chemistry 69, 3400–3405 (1997).

25. J. T. Mannion and H. G. Craighead, “Nanofluidic structures for single biomolecule fluorescent detection,” Biopolymers 85, 131–143 (2006).

26. W. E. Moerner, “New directions in single-molecule imaging and analysis,” Proceedings of the National Academy of Sciences USA 104, 12596–12602 (2007).

27. A. E. Cohen, “Trapping and Manipulating Single Molecules in Solution,” Ph.D. Dissertation, Stanford, (2006).

28. A. P. Fields and A. E. Cohen, “Electrokinetic trapping at the one nanometer limit,” Proceedings of the National Academy of Sciences 10.1073, (2011).

29. J. Bechhoefer, “Feedback for physicists: A tutorial essay on control,” Rev. Mod. Phys. 77, 783–836 (2005).

30. M. D. Lew, M. A. Thompson, M. Badieirostami, and W. E. Moerner, “In-vivo three-dimensional superresolution fluorescence tracking using a double-helix point spread function,” Proceedings of SPIE 7571, 75710Z–1–75710Z–13 (2010).

31. M. A. Thompson, M. D. Lew, M. Badieirostami, and W. E. Moerner, “Localizing and tracking single nanoscale emitters in three dimensions with high spatio-temporal resolution using a double-helix point spread function,” Nano Letters 10, 211–218 (2010).

32. M. A. Thompson, J. Casolari, M. Badieirostami, P. O. Brown, and W. E. Moerner, “Three-dimensional tracking of single mRNA particles in Saccharomyces cerevisiae using a double-helix point spread function," Proceedings of the National Academy of Sciences 107, 17864–17871 (2010).

33. M. D. Lew, S. F. Lee, Majid Badieirostami, and W. E. Moerner, “Corkscrew point spread function for far-field three-dimensional nanoscale localization of point-like objects," Optics Letters 36, 202–204 (2011).

34. C. Gosse and V. Croquette, “Magnetic tweezers: Micromanipulation and force measurement at the molecular level,” Biophysical Journal 82, 3314–3329 (2002).

35. A. Meglio, E. Praly, F. Ding, J. Allemand, D. Bensimon, V. Croquette, “Single DNA/protein studies with magnetic traps”, Current Opinion in Structural Biology, 19, 615–622 (2009).

36. M. Manosas, A. Meglio, M. M. Spiering, F. Ding, S. J. Benkovic, F. Barre, O. A. Saleh, J. F. Allemand, D. Bensimon, V. Croquette, “Magnetic tweezers for the study of DNA tracking motors”, Methods in Enzymology 475, 297–320 (2010).

37. F. Mosconi, J. F. Allemand, D. Bensimon, and V. Croquette. “Measurement of the torque on a single stretched and twisted DNA using magnetic tweezers,” Physical Review Letters 102, 78301–78304 (2009).

38. A. Ashkin, “Optical trapping and manipulation of neutral particles using lasers,” Proceedings of the National Academy of Sciences USA 94, 4853–4860 (1997).

39. K. C. Neuman, T. Lionnet and J. F. Allemand, “Single-molecule micromanipulation techniques,” Annual Review of Materials Research 37, 33–67 (2007).

40. M. Dienerowitz, M. Mazilu, and K. Dholakia, “Optical manipulation of nanoparticles: a review,” Journal of Nanophotonics 2, 21875–21906 (2008).

41. D. Lasne, G. A. Blab, S. Berciaud, M. Heine, L. Groc, D. Choquet, L. Cognet, and B. Lounis. “Single Nanoparticle Photothermal Tracking (SnaPT) of 5 nm gold beads in live cells,” Biophysical Journal 91, 4598–4604 (2007).

42. C. Ropp, R. Probst, Z. Cummins, R. Kumar, A. J. Berglund, S. R. Raghavan, E. Waks, and B. Shapiro. “Manipulating quantum dots to nanometer precision by control of flow,” Nano Letters 10, 2525–2530 (2010).

43. C. Ropp, Z. Cummins, R. Probst, S. Qin, J. T. Fourkas, B. Shapiro, and E. Waks. “Positioning and immobilization of individual quantum dots with nanoscale precision.” Nano Letters 10, 4673–4679 (2010).

44. J. Lakowicz, Principles of Fluorescence Spectroscopy, Baltimore: Springer, (2006).

45. J. Eid, A. Fehr, J. Gray, K. Luong, J. Lyle, G. Otto, P. Peluso, D. Rank, P. Baybayan, B. Bettman, A. Bibillo, K. Bjornson, B. Chaudhuri, F. Christians, R. Cicero, S. Clark, R. Dalal, A. deWinter, J. Dixon, M. Foquet, A. Gaertner, P. Hardenbol, C. Heiner, K. Hester, D. Holden, G. Kearns, X. Kong, R. Kuse, Y. Lacroix, S. Lin, P. Lundquist, C. ma, P. Marks, M. Maxham, D. Murphy, I. Park, T. Pham, M. Phillips, J. Roy, R. Sebra, G. Shen, J. Sorenson, A. Tomaney, K. Travers, M. Trulson, J. Vieceli, J. Wegener, D. Wu, A. Yang, D. Zaccarin, P. Zhao, F. Zhong, J. Korlach, and S. Turner, “Real-time DNA sequencing from single polymerase molecules,” Science 323, 133–138 (2009).

46. M. Orrit, “Fluorescence as the choice method for single-molecule detection,” Fluorescence of Supermolecules, Polymers, and Nanosystems, Ed. M. N. Berberan-Santos, Springer Berlin Heidelberg, (2008)

47. W. E. Moerner and D. P. Fromm, “Methods of single-molecule fluorescence spectroscopy and microscopy,” Rev. Sci. Instrum. 74, 3597–35619 (2003)

48. M. Burkhardt and P. Schwille, “Electron multiplying CCD based detection for spatially resolved fluorescence correlation spectroscopy,” Optics Express 15, 5013–5020 (2006).

49. P. Song, L. M. Davis, and G. R. Bashford, “Single-molecule diffusion coefficient estimation by image analysis of simulated CCD images to aid high-throughput screening,” Conf. Proc. IEEE Eng. Med. Biol. Soc., 1396–1399 (2009).

50. R. A. Keller, W. P. Ambrose, A. A. Arias, H. Cai, S. R. Emory, P. M. Goodwin, and J. H. Jett, “Analytical applications of single-molecule detection,” Anal. Chem. 74, 316A–324A (2002).

51. Andor iXon3 897 EMCCD camera hardware guide. Some information available online at <http://www.andor.com/scientific_cameras/ixon_emccd_camera/897_single-photon/>.

52. W. N. Robinson and L. M. Davis, "Simulation of single-molecule trapping in a nanochannel," J. Biomed. Opt. 15, 045006, 1–12 (2010).

53. L. M. Davis and W. N. Robinson, "Simulations for guiding the delivery and trapping of single biomolecules in a nanofluidic device," Proc. SPIE 7750, 1–9 (2011).

54. A. Spinelli, L. M. Davis, and H. Dautet, "Actively quenched single-photon avalanche diode for high repetition rate time-gated photon counting," Rev. Sci. Instrum. 67, 55–61 (1996).

55. L. M. Davis, Z. Sikorski, W. N. Robinson, G. Shen, X. Li, B. K. Canfield, I. Lescano, B. W. Bomar, W. H. Hofmeister, J. Germann, J. King, Y. White, and A. Terekhov, "Maximum-likelihood position sensing and actively controlled electrokinetic transport for single-molecule trapping," in Single-Molecule Spectroscopy and Imaging, ed. by J. Enderlein, Z. K. Gryczynski, R. Erdmann, Proceedings of SPIE 6862, 68620P, 1−10 (2008).

56. C. Xu and W. W. Webb, “Measurement of two-photon excitation cross sections of molecular fluorophores with data from 690 to 1050 nm,” J. Opt. Soc. Am. B 13, 481–491 (1996).

57. A. G. Basden, C. A. Haniff, and C. D. Mackay, “Photon counting strategies with low-light-level CCDs”, Monthly Notices of the Royal Astronomical Society 345, 985–991 (2003).

APPENDIX 1:

W. N. Robinson and L. M. Davis, "Simulation of single-molecule trapping in a nanochannel," J. Biomed. Opt. **15**, 045006 (August 2010); doi:10.1117/1.3477320;

This paper was selected for inclusion in the August 23, 2010 issue of The Virtual Journal of Nanoscale Science & Technology. The Virtual Journal, which is published by the American Institute of Physics and the American Physical Society in cooperation with numerous other societies and publishers, is an edited compilation of links to articles from participating publishers, covering a focused area of frontier research. You can access the Virtual Journal at http://www.vjnano.org .

This paper was also selected for inclusion in the August 15, 2010 issue of Virtual Journal of Biological Physics Research. The Virtual Journal, which is published by the American Physical Society and the American Institute of Physics in cooperation with numerous other societies and publishers, is an edited compilation of links to articles from participating publishers, covering a focused area of frontier research. You can access the Virtual Journal at http://www.vjbio.org.

Simulation of single-molecule trapping in a nanochannel

William Neil Robinson
Lloyd M. Davis
University of Tennessee Space Institute
Center for Laser Applications
411 B. H. Goethert Parkway
Tullahoma, Tennessee TN 37388

Abstract. The detection and trapping of single fluorescent molecules in solution within a nanochannel is studied using numerical simulations. As optical forces are insufficient for trapping molecules much smaller than the optical wavelength, a means for sensing a molecule's position along the nanochannel and adjusting electrokinetic motion to compensate diffusion is assessed. Fluorescence excitation is provided by two adjacently focused laser beams containing temporally interleaved laser pulses. Photon detection is time-gated, and the displacement of the molecule from the middle of the two foci alters the count rates collected in the two detection channels. An algorithm for feedback control of the electrokinetic motion in response to the timing of photons, to reposition the molecule back toward the middle for trapping and to rapidly reload the trap after a molecule photobleaches or escapes, is evaluated. While accommodating the limited electrokinetic speed and the finite latency of feedback imposed by experimental hardware, the algorithm is shown to be effective for trapping fast-diffusing single-chromophore molecules within a micron-sized confocal region. Studies show that there is an optimum laser power for which loss of molecules from the trap due to either photobleaching or shot-noise fluctuations is minimized. [DOI: 10.1117/1.3477320]

Keywords: single molecule; fluorescence; nanochannel; trapping; spectroscopy; simulation; diffusion; photon counting.

Paper 10111RR received Mar. 4, 2010; revised manuscript received Jun. 14, 2010; accepted for publication Jun. 23, 2010; published online Aug. 6, 2010.

1 Introduction

A single fluorescent molecule may be readily detected in a confocal microscope, but diffusion restricts the residence time of the molecule within the probe volume and hence limits the maximum observation time. This paper presents Monte Carlo simulations of the detection and trapping of a single fluorescent biomolecule confined to a nanochannel by use of electrokinetic motion for the countering of diffusion.

Enderlein first described the use of feedback to compensate for diffusion to enhance observation capabilities for single molecules.[1] He proposed that confocal microscopy can be used to track a fluorescent molecule across a spatial range in a two-dimensional membrane. While this can also be done with wide-field microscopy, confocal microscopy typically provides improved signal-to-noise ratio (SNR) and allows for observation of subnanosecond timing of fluorescence events by use of a single-photon avalanche diode (SPAD) or photomultiplier (PM) detector and time-correlated single-photon counting. This technique also has the desirable property of being able to measure the fluorescence lifetime, but the SPAD or PM detector provides no direct spatial information. However, a focused laser spot scanning in a circular pattern can be used to determine spatial information and thereby perform tracking of a molecule. The signal given by the detector will modulate in time according to the position of the molecule, being more constant when the molecule is near the center of the scanning circle and more intensely modulated as it is displaced from this position. If polar coordinates are used, the intensity of the modulation gives the radial coordinate r, and the phase of the modulation provides the angular position θ (Ref. 1). Feedback can then be used to control a piezoelectric translator to track the molecule so that it remains near the middle of the circular pattern.

The technique has been extended to tracking in three dimensions (3-D) by use of a scanning pattern that is also modulated in the axial direction. Berglund and Mabuchi have tracked individual fluorescent particles by use of a scanning laser focus with single-photon excitation.[2] Two-photon experiments with similar scanning patterns have been performed by the group of Gratton.[3] There is clear interest in tracking single molecules, particularly proteins within living cells. Levi and Gratton have done work to this end with various probes, including colloidal gold and quantum dots.[4]

Quantum dots have also been tracked in 3-D using another technique.[5,6] Collected fluorescence is split at a beamsplitter and imaged onto two sets of two adjacent optical fibers, each connected to a separate SPAD detector. The fibers collect light from four points arranged in a tetrahedron to provide position information in all three spatial dimensions. A piezoelectric translation stage controlled by feedback then provides a means for repositioning a single quantum dot to the middle of

Address correspondence to Lloyd M. Davis, University of Tennessee Space Institute, Center for Laser Applications, Tullahoma, TN 37388. Tel: 931-393-7335; Fax: 931-393-7218; E-mail: ldavis@utsi.edu

1083-3668/2010/15(4)/045006/12/$25.00 © 2010 SPIE

the four points. This technique has enabled tracking of particles with a diffusion coefficient of $\sim 0.7\ \mu m^2\ s^{-1}$.

In addition to tracking, many single-molecule studies would benefit from trapping. For example, it is possible to covalently bind a biomolecule of interest to a dielectric bead, which is held with magnetic[7] or optical tweezers.[8] Dielectric beads as small as 20 nm have been optically trapped, and magnetic beads are available in sizes down to a few hundred nanometers.[9] In both cases, the effectiveness of trapping scales with the cube of the size of the bead and a very high magnetic field or laser power would be needed to trap a very small bead or biomolecule. Also, the covalent binding of a biomolecule to a substrate or bead may impair its biological activity or otherwise alter its behavior. Hence for studies of single biomolecules, alternative means of trapping the molecule are of interest.

Cohen and Moerner have developed the anti-Brownian electrophoretic (ABEL) trap, which uses feedback to trap a molecule within a thin fluidic cell with four electrodes to control electrokinetic motion in two dimensions (2-D).[10–12] They initially used a CCD camera for the 2-D position determination. For faster temporal response and feedback, in later experiments, they employed the circular-scanning focused laser spot technique. Four electrodes provide for the electrokinetic transport of the molecule in two dimensions, with the third dimension being confined by the walls of the fluidic device, which are separated by only ~ 400 nm.

When a molecule in solution is confined to a thin volume between two planar interfaces for trapping in 2-D, it suffers a high rate of collisions with the surfaces (typically, $>10^4$ collisions/s, as indicated by our Monte Carlo simulations). For applications that can tolerate such disturbances, a 1-D nanochannel trap should be equally useful but simpler to implement and control.[13]

There has been increasing interest in single-molecule trapping in solution.[14] Also, experiments on the confinement and detection of single molecules within nanochannels have been reported as early as 1997.[15] More recently, there have been rapid developments in the capabilities for fabricating nanochannels in lab-on-a-chip devices for single-biomolecule fluorescence detection applications.[16] Initial experiments on single-molecule detection with actively controlled electrokinetic transport of the solution within a nanochannel in a device fabricated from fused silica have been reported.[13] Maximum-likelihood data analysis strategies for sensing the position of a single molecule within a trap have also been described.[17]

This paper discusses Monte Carlo computer simulations of the successive delivery and 1-D trapping of single molecules within a nanochannel. The simulations provide a means for developing and testing algorithms that may be implemented in software within a field-programmable gate array (FPGA), which is a part of the hardware for controlling the electrokinetic voltages of the single-molecule trap.[13] The simulation also enables the robustness of the trap to be studied under different experimental conditions. The goal is to trap a molecule in a nanochannel at detected photon count rates of $\sim 10^5\ s^{-1}$ and to rapidly replace it with a new one following photobleaching or escape.

Monte Carlo simulations have been used for validating experiments and determining feasibility limits since the first reports on detection of single-chromophore molecules in solution.[18] The algorithms in early work simulated the number of detected photons in fixed sequential time intervals and have been used to study efficiency of detection,[19] two-color coincidence detection limits,[20] and statistical noise in fluorescence correlation spectroscopy.[21] An algorithm for efficiently generating the time of arrival of each detected photon by use of variable time intervals for the various physical processes was later developed and used for detailed studies of fluorescence correlation spectroscopy,[22] including the effects of triplet crossing and saturation.[23] The Monte Carlo simulations presented in this paper use a similar algorithm with variable time intervals for the excitation and photophysical processes to determine the precise timing of each photon, which must be known to implement trapping.

Section 2 presents details of the numerical modeling from which the principles of the trapping procedure become evident. Section 2.1 explains the two-beam pulse-interleaved excitation scheme and time-gated photon counting, which provide information about molecule position; Sec. 2.2 explains the procedures for modeling Brownian diffusion and timed adjustment of electrokinetic transport of molecules; Sec. 2.3 discusses the photophysical processes that molecules undergo and how these are simulated to determine the precise timing of events; Sec. 2.4 discusses photon detection, including photodetector timing jitter, background, dead-time, and afterpulses, as well as the recording of photon time-stamp data in experimental format; and Sec. 2.5 presents the algorithm used for trapping and the reloading of the trap following loss of signal. Section 3 tabulates parameters and presents figures that summarize the predicted behavior of the trap for different experimental settings. Determination of statistical data from the autocorrelation of the sequence of photons is explained, and autocorrelation functions from simulations are compared with those from previously reported experiments. Section 4 concludes with a summary of the major findings.

2 Numerical Modeling

2.1 *Laser Excitation Profile and Time-Gated Photon Collection*

In order to determine the position of the molecule along the nanochannel, a time-varying spatial pattern of laser irradiance is used together with time-gated photon detection. The irradiance pattern is formed by splitting the beam from a mode-locked laser into two beams, which are then recombined at a second beamsplitter and focused into the nanochannel at two closely spaced points separated by an adjustable distance. The mode-locked laser delivers picosecond pulses separated by $T=13.2$ ns, and one of the two beams is delayed by $T/2=6.6$ ns so that the excitation pulses at each focal spot alternate in time, with 6.6 ns between the excitations.

The width and depth of the nanochannel ($d_y, d_z \approx 100$ nm) are much smaller than the beam waist of each laser spot ($\omega_0=0.5\ \mu$m), and hence the irradiance is approximately constant through each cross section of the nanochannel. The profiles for each laser spot are assumed to be Gaussian along the length x of the nanochannel, and hence the total irradiance from the series of laser pulses is given by

$$I(x,t) = I_1(x,t) + I_2(x,t), \tag{1}$$

where

$$I_1(x,t) = \frac{\bar{P}}{\pi\omega_0^2} \exp[-2(x-x_1)^2/\omega_0^2] \sum_k \delta(t-kT), \tag{2}$$

$$I_2(x,t) = \frac{\bar{P}}{\pi\omega_0^2} \exp[-2(x+x_1)^2/\omega_0^2] \sum_k \delta(t-kT-T/2), \tag{3}$$

are the irradiance profiles of the left and right laser foci, and where $\bar{P}$ is the combined mean power of both laser beams, which are equal, ω_0 is the beam waist of each beam, x_1 is one-half of the separation between the two laser foci, and the temporal profile of each picosecond laser pulse is represented as $\delta(t)$. Ideally, the separation $2x_1$ is set to be equal to ω_0, as this provides greatest slope of the irradiance from each laser spot at the center of the trap and hence greatest sensitivity for position determination. With this beam separation, the total time-averaged irradiance from the two beams is approximately constant between $x=-x_1$ and x_1, as shown in Fig. 1. This provides the advantage that the time-averaged excitation of a trapped molecule remains constant as it diffuses within the bounds of the trap.

Photon detection is time-gated into two channels. Each channel counts photons that fall within a 6.6-ns interval that follows one set of excitation pulses at one of the two laser foci. Fluorescence photons generated by each laser focus generally fall into the time channel corresponding to that focus. However, if the fluorescence decay takes longer than 6.6 ns, the released photon will be counted after the next laser pulse, causing the photon to be registered in the incorrect time channel. Such events lead to cross talk and decreased precision in the prediction of the molecule position. Also, the single-photon timing error of the SPAD detector may cause a photon to be registered in the incorrect time channel. This is modeled by adding a random number with a distribution that approximates the SPAD impulse response function to the arrival time of each detected photon. In the results presented in Sec. 3, this distribution is taken to be a Gaussian with a standard deviation of $\sigma=127.4$ ps and a mean shift of 3σ, which closely models the experimental distribution. Figure 2 shows the histograms of the time delays between photon detection events and the laser pulses generated by a simulation of trapping in which the fluorescence lifetime is taken to be $\tau_F=3.0$ ns. In this case, the probability for assignment of a fluorescence photon into the incorrect time channel is ~0.1. The methods for simulation of background and detector afterpulses are discussed in Sec. 2.4.

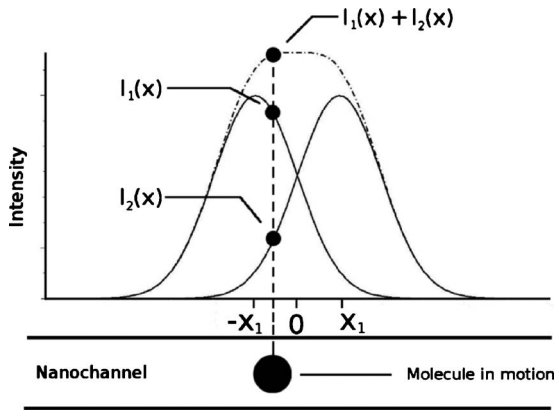

Fig. 1 Irradiance profiles of each of the two laser beams, $I_1(x)$ and $I_2(x)$, and the total irradiance (dotted-dashed line) experienced by a molecule at a position x within the nanochannel.

2.2 *Molecular Transport*

The numerical simulation considers individual molecules being transported on a one-dimensional grid along the long axis of the nanochannel by Brownian diffusion and also by electrokinetic flow due to the voltage applied across the length of the nanochannel. The grid must be fine compared to the size of the laser waist in order to accurately model the level of excitation of molecules within the focused laser beams. For the results of Sec. 3, the waist is $\omega_0=0.5$ μm, and the grid spacing is set to $\Delta x=.01$ μm. The simulation models a nanochannel with a length of 20 μm, which corresponds to $2L+1=2001$ grid points.

Electrokinetic flow along the nanochannel is modeled by moving all molecules one grid space in the appropriate direction at appropriate times. If the flow velocity v_F is constant, then the moves occur at regular time intervals Δt_F such that

$$v_F \Delta t_F = \pm \Delta x. \tag{4}$$

However, if the flow is adjusted during trapping, then the time and direction of the next flow step is reevaluated. For example, if the flow velocity is changed from v_F to v_F', at a time t' following the last flow step, then the time until the next flow step is $\Delta t_F'$ such that

$$v_F t' + v_F'(\Delta t_F' - t') = \pm \Delta x. \tag{5}$$

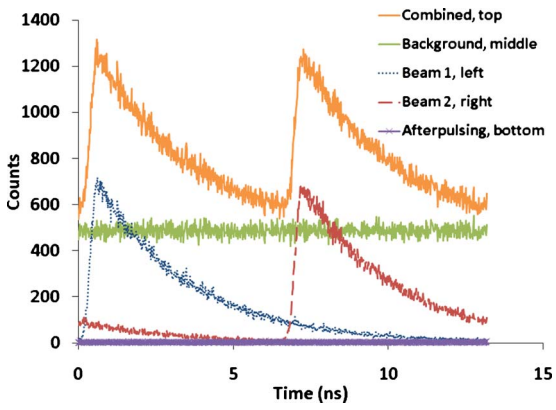

Fig. 2 Histograms of the timing delays (1024 channels at 12.89 ps/channel) between the pulsed laser excitation (beam 1, left) and the detection of photons due to fluorescence from each beam (blue and red curves), background (green curve), detector afterpulses (purple curve), and all combined (orange curve), as collected during a simulation of sequential single-molecule trapping for a total simulated duration of 1000 s. (Color online only.)

During each move, if there are any molecules on the downstream end point of the grid, they will leave the simulation. Also, for each move, molecules may enter the simulation onto the upstream end point of the grid. To model this, note that molecules enter at random with a probability for entry for each grid step due to flow equal to C_0, the mean number of molecules per grid point. Thus, following the start of the simulation and whenever a molecule enters, a geometrically distributed random number for a probability of success C_0 is retrieved (using the Intel Math Kernel Library routine *viRngGeometric*) to find the number of flow steps until the next entry. The value of C_0 is given by

$$C_0 = 10^3 N_A C \Delta x d_y d_z, \tag{6}$$

where N_A is Avogadro's number, C is the molar concentration of molecules in solution, and d_y, d_z are the width and depth of the nanochannel, with all lengths expressed in meters. Typical parameter values are $C=100$ pM and $d_y=d_z=10^{-7}$ m, corresponding to $C_0=6\times10^{-6}$ molecules per grid point.

Brownian diffusion is independent of the electrokinetic flow and is modeled by Fick's second law of diffusion in one dimension:

$$\frac{\partial \rho}{\partial t} = D\frac{\partial^2 x}{\partial t^2}\rho, \tag{7}$$

where $\rho(x)\mathrm{d}x$ is the probability of finding a molecule within $\mathrm{d}x$ of x, and D is the diffusion coefficient. With the initial condition of a molecule starting at the origin at time $t=0$:

$$\rho(x, t=0) = \delta(x), \tag{8}$$

where $\delta(x)$ is the Dirac delta function, the solution of Eq. (7) is

$$\rho(x,t)\mathrm{d}x = \frac{1}{\sqrt{2\pi}\sigma(t)}\exp\left[\frac{-x^2}{2\sigma^2(t)}\right]\mathrm{d}x, \tag{9}$$

which is a normalized Gaussian distribution with standard deviation

$$\sigma(t) = \sqrt{2Dt}. \tag{10}$$

To model diffusion on a grid, molecules may hop to nearby grid points at regular time intervals Δt_D. The time step for diffusion is chosen so that the standard deviation of the Gaussian in Eq. (9) is one grid point, i.e., $\sigma(\Delta t_D)=\Delta x$, or

$$\Delta t_D = (\Delta x)^2/(2D), \tag{11}$$

where $\rho(x, \Delta t_D)\mathrm{d}x = \exp(-x^2/2)\mathrm{d}x/\sqrt{2\pi}$. At each time step Δt_D, each molecule within the simulation is moved j grid spaces, where j is a random integer. To choose the value of j with the appropriate Gaussian weighting, a 32-bit random number X uniformly distributed between 0 and 1 is retrieved and successively compared with the cumulative probability values $P(j)$ listed in column 3 of Table 1, beginning at the top, until it is found to be less than the value listed for the corresponding value of j. For example, if $X=0.6753$, then the value of j is taken to be -1 because $0.6246<0.6753<0.8664$. The values in column 3 are given by the expressions in column 2, where we define

Table 1 Cumulative probabilities for diffusion.

j	$P(j)$ expression	$P(j)$ value
0	$2E(0.5)$	0.382924922548026
1	$E(0.5)+E(1.5)$	0.624655260005155
−1	$2E(1.5)$	0.866385597462284
2	$E(1.5)+E(2.5)$	0.926983133405366
−2	$2E(2.5)$	0.987580669348448
3	$E(2.5)+E(3.5)$	0.993557705595188
−3	$2E(3.5)$	0.999534741841929
4	$E(3.5)+(4.5)$	0.999763973247840
−4	$2E(4.5)$	0.999993204653751
5	$E(4.5)+E(5.5)$	0.999996583337313
−5	$2E(5.5)$	0.999999962020875
6	$E(5.5)+E(6.5)$	0.999999980970278
−6	$2E(6.5)$	0.999999999919680

$$E(a) = \int_0^a \exp(-x^2/2)\mathrm{d}x/\sqrt{2\pi}, \tag{12}$$

and the expressions are evaluated using the error function:

$$\mathrm{erf}(x) = 2E(\sqrt{2}x). \tag{13}$$

Note that the probability to diffuse by more than six grid spaces is less than one part in 2^{32}, and hence for the 32-bit random numbers used here, j is between -6 and 6.

When molecules hop to new grid points, there is a chance that some may hop off the grid and leave the simulation, but there is an equal possibility that new molecules may diffuse onto the grid. This is accounted for as follows: For each diffusion time step Δt_D, the probability that a new molecule hops onto a point k spaces from the end of the grid is

$$P_k = C_0[E(6.5) - E(0.5+k)], \quad k = 0, \ldots, 5. \tag{14}$$

Note that this exactly balances the probability to leave the grid. For example, if a molecule is at a point $k=4$ spaces from the end of the grid, it can escape from the grid by hopping 5 or 6 spaces, with a probability $[E(5.5)-E(4.5)]+[E(6.5)-E(5.5)]$. The total probability per diffusion time step P that a new molecule enters somewhere onto the grid from either end is found by adding the probabilities to hop to a point that is $k=0$ to 5 spaces from either of the ends. This is hence given by

$$P = 2\sum_{k=0}^{5} P_k = 2C_0\left[6E(6.5) - \sum_{k=0}^{5} E(0.5+k)\right]$$
$$= 0.763540130047191C_0. \quad (15)$$

Because molecules enter onto the grid at random at a rate equal to $P/\Delta t_D$, at the start of the simulation and whenever a new molecule enters by diffusion, a geometrically distributed random number for a probability of a success P is retrieved to determine the number of diffusion time steps until the next entry. Also, a 32-bit uniform random number X is retrieved and compared successively to the cumulative probabilities Q_l listed in Table 2 to determine the position l on the grid at which the molecule will enter.

Note that molecules may enter or leave the simulation from either end of the grid, but when the trap is operating, they are more likely to enter from the left ($l=-L=-1000$, or $x=-1000\Delta x$) and leave from the right, because when there is no fluorescence signal from molecules within the focused laser beams, the electrokinetic flow is set to a maximum so as to transport molecules in from the left side and out from the right side.

Experiments in our lab[13] have found that diffusion of fluorescent dye molecules in a nanochannel fabricated from fused silica is slowed by a factor of ~50, in agreement with the observations of Lyon and Nie.[15] However, it is likely that this is due to sticking of molecules to the nanochannel walls and that avoidance of sticking by surface treatment or other means will restore the free solution diffusion. Hence, to assess the capability for trapping molecules that do not stick, for the simulation results presented in Sec. 3, the diffusion coefficient is taken to be $D=2.2\times10^{-6}$ cm^2 s^{-1} (with corresponding $\Delta t_D=0.45$ μs), which is that of a small fluorescent dye molecule with a hydrodynamic radius of ~1 nm freely diffusing in solution.[24] As expected, trapping is easier to achieve for smaller values of D.

Table 2 Cumulative probabilities for new entry positions.

l	Q_l expression	Q_l value
$-L$	$Q_0=P_0/P$	0.404066599711270
L	$Q_L=Q_0+P_0/P$	0.808133199422541
$1-L$	$Q_1=Q_L+P_1/P$	0.895625174513805
$L-1$	$Q_{L-1}=Q_1+P_1/P$	0.983117149605069
$2-L$	$Q_2=Q_{L-1}+P_2/P$	0.991249444832068
$L-2$	$Q_{L-2}=Q_2+P_2/P$	0.999381740059067
$3-L$	$Q_3=Q_{L-2}+P_3/P$	0.999686395503419
$L-3$	$Q_{L-3}=Q_3+P_3/P$	0.999991050947771
$4-L$	$Q_4=Q_{L-3}+P_4/P$	0.999995500604795
$L-4$	$Q_{L-4}=Q_4+P_4/P$	0.999999950261819
$5-L$	$Q_5=Q_{L-4}+P_5/P$	0.999999975130910
$L-5$	$Q_{L-5}=Q_5+P_5/P$	1.000000000000000

Note: $2L+1=2001$ is the number of grid points.

2.3 *Photophysics*

As shown in Fig. 3, when irradiated, a molecule can become excited from the ground state S_0 to the S_1 manifold, and from here, it may follow four possible paths. It may (i) decay back to the ground state without the detection of a fluorescence photon, with probability $P_{(i)}$ (due either to nonradiative decay or fluorescence emission of a photon that is not detected); or (ii) decay back to the ground state with the detection of a fluorescence photon, with probability $P_{(ii)}$; or (iii) cross to the triplet manifold T_1 before decaying back to the ground state, with probability $P_{(iii)}$; or (iv) undergo irreversible photobleaching and be removed from subsequent photophysical transitions, with probability $P_{(iv)}$. For (i) and (ii), relaxation back to the ground state occurs after a random time with an exponential distribution and mean equal to the fluorescence lifetime ($\tau_f\sim3.0$ ns), whereas for (iii), the mean is equal to the phosphorescence lifetime ($\tau_p\sim1$ μs). The timing of excitation events, the pathway taken after excitation, and the time taken for relaxation to the ground state and possible photon detection are all stochastic processes that are modeled using Monte Carlo methods.

For trapping, the position determination of the molecule is dependent on the timing of photon detection events, which in turn is dependent on the timing of molecular excitation events. Two different methods have been used in the simulation to model the timing of molecular excitations. In the first, for each laser pulse (i.e., for each time step of $T/2=6.6$ ns), a uniform random number is retrieved and compared to the probability for excitation per laser pulse for that beam to determine whether that pulse causes excitation. In the second, the waiting time until the next excitation is found as follows: Geometrically distributed random numbers for probabilities of success equal to the probabilities of excitation per laser pulse for each of the two beams are retrieved to find the times at which each beam would next give excitation, and the earlier event is then chosen. However, if the molecule moves due to diffusion or flow before excitation occurs, then new geometrically distributed random numbers are retrieved for the excitation probabilities per pulse appropriate for the new location of the molecule. We find that the second method generates results that are the same as the first but is computationally much

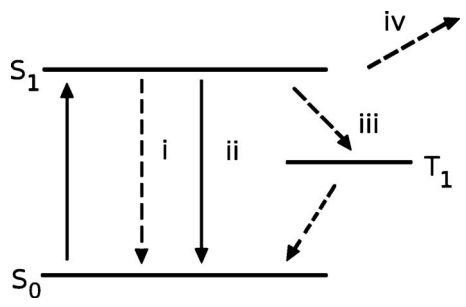

Fig. 3 Jablonski diagram for the decay possibilities of the molecule. S_0 is the singlet ground state, S_1 is the singlet excited state, and T_1 is the triplet state.

faster, as may be expected because the mean time between excitation events is long compared to the interval between laser pulses $T/2=6.6$ ns, yet short compared to Δt_F and Δt_D.

For either method of simulating excitation, a molecule at position x has a rate of excitation from each of the two beams ($b=1,2$) given by

$$k_b(x,t) = \sigma_a I_b(x,t)/E_\lambda, \tag{16}$$

where σ_a is the absorption cross section, E_λ is the photon energy, and $I_b(x,t)$ is given by Eq. (2) and (3). The probability for excitation for each laser pulse is thus $P_1^E(x) = k_1(x,0)T$ and $P_2^E(x)=k_2(x,T/2)T$ for beams 1 and 2. The values of these probabilities for each grid point may be stored in lookup tables. For the first method, these are then used for comparison with uniform random numbers to determine whether excitation occurs for each laser pulse. For the second method, these are then used to retrieve geometrically distributed random numbers for these probabilities of success to determine when the next excitation would occur. For the results presented in Sec. 3, parameter values are $\sigma_a=2\times10^{-16}$ cm^2 (corresponding to a fluorophore such as Alexa 610), $E_\lambda=3.3\times10^{-19}$ J, and a total laser power of $\bar{P}=30$ μW, so that the total mean excitation rate for a trapped molecule is $k_1(0,0)+k_2(0,T/2)\approx2.8\times10^6$ s^{-1}.

Once a molecule is excited, a uniform random number X is retrieved and successively compared to the summed values of the probabilities for the four possible relaxation pathways, which are listed in Table 3. If $X<P_{(i)}$, relaxation is by pathway (i); otherwise, if $X<P_{(i)}+P_{(ii)}$, relaxation is by pathway (ii); otherwise, if $X<P_{(i)}+P_{(ii)}+P_{(iii)}$, relaxation is by pathway (iii); otherwise, relaxation is by pathway (iv).

The most likely pathway is (i) decay to the ground state without detection of a fluorescence photon, which occurs with a probability of $P_{(i)}=1-P_{(ii)}-P_{(iii)}-P_{(iv)}$ (typically, $\sim$0.95). This is the sum of the probability for nonradiative decay from S_1 and radiative decay with missed photon detection. The second most likely pathway is (ii) decay to the ground state with detection of a fluorescence photon. For a well-designed single-molecule microscope and for the results presented in Sec. 3, $P_{(ii)}=0.05$, and in practice, it is determined by the product of the fluorophore quantum efficiency ($\sim$0.8), the fluorescence collection efficiency of the microscope objective ($\sim$0.20); the transmission of the spectral filter, objective lens, and other optical components ($\sim$0.5); and the photon detection efficiency of the SPAD detector ($\sim$0.65). The third most likely pathway is (iii) crossing to the triplet manifold, which is taken to be $P_{(iii)}=10^{-3}$, and the least likely pathway is (iv) photobleaching, which is taken to be $P_{(iv)}=10^{-5}$. These last two values are typical parameters for fluorophores commonly used in single-molecule experiments.[25] For the preceding probabilities and a mean excitation rate of 2.8×10^6 s^{-1}, the expected photon count rate is 1.4×10^5 s^{-1}, and the mean time before photobleaching is $\sim$35 ms.

Table 3 Relaxation pathway probabilities.

Path	Mechanism	Probability
i	Singlet decay without photon detection	$P_{(i)}=1-P_{(ii)}-P_{(iii)}-P_{(iv)}$
ii	Singlet decay with photon detection	$P_{(ii)}=0.05$
iii	Triplet crossing	$P_{(iii)}=10^{-3}$
iv	Photobleaching	$P_{(iv)}=10^{-5}$

2.4 *Photon Detection*

The desired outcome of molecular excitation is photon detection, which occurs in relaxation pathway (ii). Whenever pathway (i) or (ii) is chosen, a random number with exponential distribution with mean equal to the fluorescence lifetime τ_F is retrieved to find the time of decay of the molecule, as discussed in the first paragraph of Sec. 2.3. For pathway (ii), the detection time of the photon is then found by adding another random number with a Gaussian distribution (with standard deviation of $\sigma=127.4$ ps and a mean of 3σ, in order to model the timing jitter of the SPAD and the setting of the time gate of the detection electronics of the apparatus of Ref. 13), as discussed at the end of Sec. 2.1 and in Fig. 2.

In addition to fluorescence photons, there are background photons due to detector dark noise ($d=50$ photons s^{-1}) and scattered light that passes through the filters ($s=50$ photons μW^{-1} s^{-1}). In the results presented in Sec. 3, the total background count rate is taken to be $B=s\bar{P}+d$, which gives 500 photons s^{-1} for $\bar{P}=30$ μW, and background is assumed to be random with Poissonian statistics. Hence, to simulate background, the stochastic time of occurrence of the next background photon is determined by retrieving an exponentially distributed random number with a mean equal to the reciprocal of the background count rate.

Whenever the simulation finds the time of occurrence for (1) the next background photon, (2) the next flow time step, (3) the next resetting of the flow direction during trapping, (4) the next diffusion time step, or (5) the next photophysics event for any of the molecules in the simulation (possible excitation, decay without photon detection, or decay with photon detection), it then finds the process with the minimum time (using the Intel Math Kernel Library routine *idamin*). The simulation proceeds with whatever process occurs first and then generates the time for the next occurrence of that process. In this way, independent processes are synchronized.

Whenever a photon is detected (either background or fluorescence), its time of arrival is determined by recording the total number of laser pulses (with period $T/2$) since the beginning of the experiment. This time-stamp ts_i, or laser-pulse count at the time of detection of the i'th photon, which is stored as a 32-bit unsigned integer for compatibility with the analysis routines for the experiments of Ref. 13, is either even or odd, depending on whether the photon detection follows a laser pulse to the left or right of the center of the trap. Thus, time-gated photon detection may be achieved by sorting photons based on the value of the least significant bit of the time-stamp.

Note also that the SPAD detector has a dead time of $\sim$40 ns, during which it is unresponsive. This is modeled by

ignoring a photon if it follows another by less than the SPAD dead time. Also, for each photon detected, there is a 0.5% probability that the SPAD detector will experience an afterpulse, in which case, another photon detection event will occur a random time later with an exponential distribution with a mean of ~100 ns (Ref. 26). These processes are also included in the simulation and affect the shape of the autocorrelation function for small delays, but they have been found to not significantly affect the performance of the trapping for the parameters of Sec. 3.

2.5 *Trapping*

Each time a photon is detected, a routine is entered for adjustment of the electrokinetic flow in order to achieve rapid delivery and trapping of individual molecules. A significant purpose of the simulation is to evaluate the effectiveness of the algorithm used by this routine when subject to restrictions imposed by the experimental hardware. The main constraint is that the maximum electrokinetic flow speed is limited, and for most of the results of Sec. 3, it is taken to be $v_F^{\max}=2\ \mu$m/ms, which corresponds to $\Delta t_F=5\ \mu$s. In the apparatus of Ref. 13, it is possible to apply a potential of 10 V across a 200-μm-long nanochannel to achieve a field of 5×10^4 V/m, whereas electrokinetic speeds of single molecules in capillaries are estimated to be in the range of 2 to 6 μm/ms for similar fields.[27] In the 2-D, ABEL trap, a maximum electrokinetic speed of 3 μm/ms has been reported. Also, another potential constraint is that there is a delay or latency for adjustment of the flow due to the response time of the FPGA electronics and the switching time of the voltage applied to the nanochannel. For the apparatus of Ref. 13, the latency is $\Delta t_L=6\ \mu$s, which is comparable to Δt_F, and as expected, this has been found to not significantly affect trapping. Nevertheless, to study the effects of latency, whenever the algorithm makes an adjustment to the flow velocity (and hence to the flow time step Δt_F), the change is scheduled to occur with a time delay of Δt_L. As presented in Sec. 3, the performance of the trap degrades significantly if the latency is increased beyond ~100 μs. The algorithm makes adjustments to the flow velocity, and hence the time of the next flow step based on the values of the time-stamps ts_i of the last N detected photons. For the results of Sec. 3, we have taken $N=6$, in accord with the experiments of Ref. 13. Figure 4 shows a flowchart of the algorithm, which is explained in the following. A similar algorithm is programmed into the FPGA used in the experiments of Ref. 13, but in this case, the latency is not added in the algorithm, as it is already present in the electronics.

Before a molecule is transported into the laser foci so as to emit fluorescence photons, only background photons are detected. At this time, the electrokinetic flow is set to the maximum value $v_F^{\max}$ until the observed fluorescence signal is found to be above the background level. To make this determination with fast response, the difference between the last photon time-stamp and the one just two photons earlier must be shorter than a preset threshold time th, i.e.,

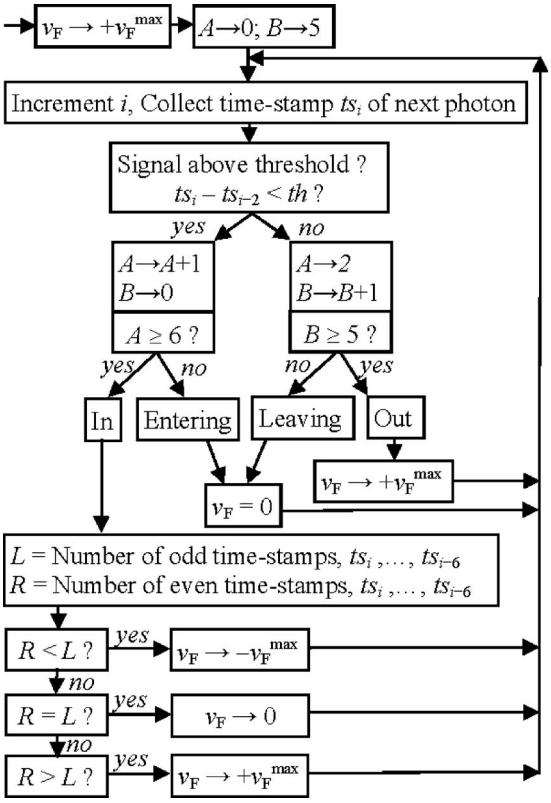

Fig. 4 Flowchart of the trapping algorithm.

$$ts_i - ts_{i-2} < th, \tag{17}$$

where the threshold time is taken to be $th=1/(5BT)=30{,}303$, corresponding to a count rate of 2.5 times the background level. Although in principle it would be possible to use a longer threshold time, it is found that small variations of the threshold produce no perceptible difference in the performance of the trapping. Also, in experiments, the background may not be known accurately or may vary, and hence a lower threshold time is more suitable.

Once the photon signal is above the background level, it is assumed that a molecule has been transported into the detection zone, so after the latency delay Δt_L, the flow is adjusted to zero. Then, after $N-3$ more photons are detected and after the latency delay Δt_L, the flow is adjusted to a value dependent on the numbers of the last N photons that are from each of the two laser beams. As before, each photon time-stamp is odd or even depending on whether the photon is more likely to originate from fluorescence excitation from the left or right laser focus. If more of the last N photons have an odd (even) time-stamp, the molecule is assumed to be to the left (right) of the center of the trap, and the algorithm then schedules the flow to be to the right (left) with the maximum flow speed $v_F^{\max}$. If the numbers of odd and even time-stamps are equal, the algorithm then schedules the flow to be zero. The flow velocity is maintained until after the next scheduled change, which occurs Δt_L after the next detected photon. For a fluorescence count rate of ~10^5 photons/s, the mean time between photons is ~10 μs, and in this time, the molecule will be moved by flow only ~0.02 μm and so should remain

within the trapping region, which is ~0.5 μm ($2x_1$) in length. Also, during initial entry of a molecule into the trap, the flow is set to zero until a time Δt_L after $N-3$ more photons are accumulated. The mean time for detection of $N-3$ photons is $\sim 10(N-3)$ μs, and in this time, the root-mean-square distance that a molecule diffuses is $\sim 0.2(N-3)^{1/2}$ μm, or ~0.36 μm, so it is unlikely that the molecule diffuses through the trapping region in this time. Also, triplet blinking does not significantly increase the chances of escape from the trap, as the triplet decay time (~1 μs) is shorter than the mean time between photons (~10 μs). If escape from the trap occurs due to statistical fluctuations, it is most likely due to a series of incorrect estimates for the direction of applied electrokinetic flow.

If the signal level decreases to the level of the background so that the condition in Eq. (17) is not true, then it is likely that that the molecule has bleached or has escaped from the trap, but it is also possible that this may occur due to statistical fluctuations. To avoid ejecting a molecule from the trap because of such fluctuations, the flow velocity is set to zero, and the condition in Eq. (17) must be false $S=5$ times in succession before the algorithm steps out of the trapping loop and sets $v_F = v_F^{\max}$ until the next molecule is loaded into the trap. The inclusion of this period of time with flow velocity set to zero following loss of signal and of multiple testing before reloading is found to reduce the probability for escape and to provide an opportunity for recapture if there is escape (as discussed with Fig. 5).

Table 4 Simulation parameters.

Parameter	Value
Laser power $\bar{P}$	30 μW
Beam waist ω_0	0.5 μm
Laser foci separation $2x_1$	0.5 μm
Laser wavelength λ	610 nm
Laser pulse spacing $T/2$	6.6 ns
Absorption cross section σ_a	2×10^{-16} cm^2
Fluorescence lifetime τ_f	3.0 ns
Triplet lifetime τ_p	1.0 μs
Grid resolution Δx	0.01 μm
Grid length $2L\Delta x$	20 μm
Diffusion coefficient D	220 μm^2/s
Maximum speed $v_F^{\max}$	2.0 μm/ms
Background count rate B	500/s
Concentration C	100 pM
Feedback latency Δt_L	6 μs

3 Results and Discussion

Table 4 summarizes the typical values of the parameters used in the simulations presented in this section. A simulation of a 1000-s experiment, including collation of statistical and diagnostic information, executes within ~120 s on a 2.3-GHz Dual-Core Pentium PC. Thus, repeated execution of the program allows one to optimize experimentally adjustable parameters such as the laser power, to easily modify experimentally fixed parameters to study limitations imposed by processes such as detector dead time, background, photobleaching, triplet kinetics, and control latency, and also to view information that would not be readily available in an experiment, such as the trajectory and photophysical state of each molecule.

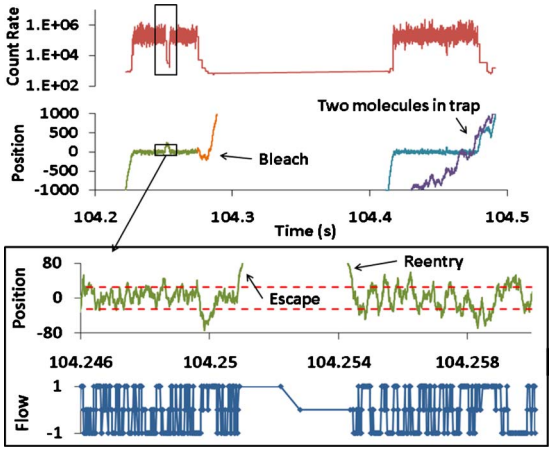

Fig. 5 Example of the total photon count rate $R(t)$ (first plot, red), and molecule trajectories $x(t)$ (second plot); (position given in units of grid spaces, $\Delta x=0.01$ μm) during a simulation of trapping using parameters in Table 4. A small section of the trajectory data is expanded in the inset. The red dashed lines indicate the centers of the laser foci ($x=\pm0.25$ μm). The lower plot in the inset shows the changes to the flow direction imposed by the trapping algorithm during the same time. (Color online only.)

Figure 5 presents an example of the photon count rate $R(t)$ and the positions $x(t)$ of molecules during operation of the trapping algorithm with parameters from Table 4, during a 0.3-s interval from time $t=104.2$ s to 104.5 s. The count rate shown in the figure is updated with each detected photon time-stamp but is averaged over only the last $N=6$ detected photons: $R(ts_i)=N/[(T/2)(ts_i-ts_{i-N})]$. Hence, it exhibits considerable statistical fluctuations and so is plotted on a semilogarithmic scale. During the selected 0.3-s interval, individual molecules are brought into the detection volume by the electrokinetic flow and are trapped, but in this particular slice of data, several unusual occurrences are also seen. After the first molecule (in Fig. 5) is carried in by flow, the count rate increases to $>10^5$ s^{-1}, and the molecule is trapped. Then, the count rate suddenly dips and the signal falls below threshold, i.e., Eq. (17) fails, as the molecule escapes the trap (data shown within black rectangles in Fig. 5).

The inset in Fig. 5 shows an expansion of the trajectory data around this time of escape. The red dashed lines are the positions of the centers of the two laser foci, between which the molecule is to be trapped. The direction of the electroki-

netic flow, which is determined by the trapping algorithm from the difference in the numbers of the last $N=6$ photons that have odd and even time-stamps, is also shown in the inset. Note that at the time of escape, the flow is set in the incorrect direction. After the escape, the flow is set to zero and the molecule fortunately diffuses back into the excitation region and is trapped once again, as the algorithm reactivates switching of the flow direction in response to the difference in odd and even photon time-stamps. By comparing the two plots in the inset, one can see how the flow is adjusted to recenter the molecule, albeit with considerable error due to the shot noise from the low number of photons used for analysis. For example, near the end of the data in the inset, the molecule position is $x \approx +40\Delta x$ and the flow velocity is mostly $v_F = -v_F^{\max}$, which is in the correct direction to bring the molecule back to the center. However, during simulations of experiments of 1000-s duration, due to shot noise, the fraction of the time that the electrokinetic velocity is in the incorrect direction is found to be ~0.25. Also, molecules often pass beyond the region between the centers of the two laser foci, and the fraction of molecules that permanently escape the trap and leave the simulation before photobleaching is found to be ~0.17.

In the second plot of Fig. 5, it is shown that the first molecule photobleaches at the point where the green line changes to orange. Soon after this point, the flow is switched to zero and the photobleached molecule diffuses freely for a brief time, but the count rate does not recover and hence the algorithm then switches the flow velocity to $v_F = +v_F^{\max}$, so the photobleached molecule is transported in the positive direction out of the simulation. Approximately 0.1 s later, a second molecule, shown by a light blue trajectory, is transported by the flow into the detection volume and is subsequently trapped. While the flow direction is alternating to hold this molecule trapped, a third molecule, shown by a purple trajectory, diffuses into the simulation volume. By chance, at $t \approx 104.47$ s, this diffuses into the laser foci, and the count rate approximately doubles (although this is difficult to discern on the logarithmic scale). The algorithm responds to the counts from both molecules but cannot keep two independently diffusing molecules at the center of the trap. By chance, the third molecule diffuses away, and the second molecule remains trapped for a short while later, and then it too escapes from the trap and diffuses away.

The study of simulated trajectory data such as that in Fig. 5 can provide insight on the effectiveness and/or the causes of failings of the trapping algorithm and thereby lead to more complicated algorithms with improved performance. Experiments cannot provide such detailed data, but they do provide statistical information about the trap performance from the normalized autocorrelation function $g(\tau)$ of the stream of detected photons.[13] The amplitude and width of this function provide information about the mean number and residency time of molecules within the detection volume. The amplitudes, widths, shapes, and trends of the autocorrelation functions from the experimental runs presented in Ref. 13 are consistent with those generated by simulations, as presented in the following.

Figure 6 presents $g(\tau)$ for simulated experiments of 1000-s duration with parameters given in Table 4 but with

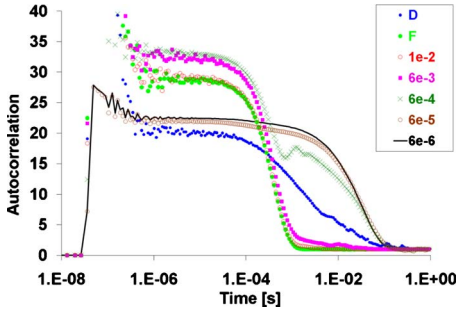

Fig. 6 Autocorrelation functions for a laser power of $\bar{P}=30$ μW for free diffusion (D, blue) and for constant electrokinetic flow (F, green) and for trapping for a range of values for the feedback latency from 1×10^{-2} s to 6×10^{-6} s. (Color online only.)

different latency delays of the feedback for the trap, decreasing down to $\Delta t_L = 6\times10^{-6}$ s, which is that of the electronics used in Ref. 13. Also shown are the plots of $g(\tau)$ for the cases of no trapping with (1) free diffusion, and (2) a constant electrokinetic flow at $v_F = +v_F^{\max}$. The change in shape and decrease in the width of $g(\tau)$ between these two curves are consistent with the experimental results shown in Figs. 14 and 15 of Ref. 13. For all these plots, $g(\tau)$ is obtained directly from the sequence of time-stamps of detected photons by use of a separate software correlator program written in LabView,[22] which is also used in the analysis of experimental data. For a latency delay of $\Delta t_L = 1\times10^{-2}$ s, the autocorrelation function is almost identical to that of the constant flow case, meaning that the trapping behavior is completely broken. On the other hand, for a latency of $\Delta t_L = 6\times10^{-6}$ s, the width of the autocorrelation is extended beyond that of free diffusion, out to a width of about 35 ms, the mean time before photobleaching calculated at the end of Sec. 2.3, indicating that the trap is working. For a latency of $\Delta t_L = 6\times10^{-5}$ s, the autocorrelation is almost the same, but when the latency is increased to $\Delta t_L = 6\times10^{-4}$ s, the trap begins to fail, as the autocorrelation now contains both the trapped and constant flow components. There is also a fluctuation at a delay time of $\sim 6\times10^{-4}$ s, due to molecules being driven out and then back into the detection volume by the electrokinetic flow.

For all the plots in Fig. 6, there is structure for time delays less than $\sim 10^{-6}$ s, also seen in experimental $g(\tau)$, due to detector dead time and afterpulses. If the values for these parameters are altered in simulations, the structure also changes. Beyond these features, at a time delay of $\sim 10^{-5}$ s, the amplitude of the shoulder gives an indication of $\bar{N}$, the mean number of molecules within the detection volume during the course of the simulated experiment. In the fluorescence correlation spectroscopy (FCS) literature, the amplitude is usually taken to be inversely proportional to $\bar{N}$, although it is also proportional to $(1-B/S)^2$, where S/B is the signal-to-background ratio.[22] One would normally expect the amplitudes for free diffusion and constant flow to be the same, as $\bar{N}$ is the same [as C_0 molecules per grid point given in Eq. (6) is the same]. However, for free diffusion, $\bar{N}$ has large fluctuations due to molecular shot noise, even for a run time of 1000 s. If the simulation is run with different random number

seeds, the number of photon bursts from single molecules and the amplitude of $g(\tau)$ varies considerably from run to run (13.2, 17.8, 23.9, 18.3, 20.1, …). This is not the case for flow or trapping, as the number of molecules that pass through the volume is much larger, so the molecular shot noise becomes negligible. Also, for free diffusion, triplet crossing and photobleaching reduce the signal-to-background ratio, and this reduces the amplitude of the autocorrelation function. All of these features can be easily observed by running the simulation with different parameters, and they explain why the amplitude for flow is greater than that of the one plot shown for diffusion. In contrast, when the trap is operating, the reduction in the amplitude of $g(\tau)$ from that of constant flow is found to be because trapping effectively increases $\bar{N}$. The occupancy $\bar{N}$ increases, because soon after each molecule photobleaches or escapes from the detection volume, the flow is switched to quickly bring in the next molecule. A similar increase in width and reduction in amplitude of $g(\tau)$ when the trap is turned on is observed in experiments reported in Fig. 17 of Ref. 13. The simulations provide supporting evidence that the changes seen in the experiments are due to effective trapping and rapid replacement of molecules, which effectively increases the mean molecular occupancy within the confocal probe region.

Figure 7 presents $g(\tau)$ obtained from a study of the effects of laser power on the trapping. For reference, plots corresponding to no trapping with free diffusion and with a constant electrokinetic flow are also included. It is found that there is an optimum laser power of $\sim$30 μW (plot shown in red), which produces the longest mean residence time [greatest width of $g(\tau)$] and the largest molecular occupancy $\bar{N}$ [smallest amplitude of $g(\tau)$]. This is about the same value of laser power that was found to be optimal for the experiments presented in Ref. 13. If the laser power is adjusted between $\sim$20 μW and $\sim$40 μW, the performance of the trap deteriorates only slightly from that at 30 μW. However, as the laser power is increased beyond $\sim$40 μW, photobleaching becomes more significant, so the mean residence time and the molecular occupancy are decreased [width of $g(\tau)$ decreases and amplitude increases]. Similarly, as the laser power is decreased below $\sim$20 μW, the rate of fluorescence photons falls, shot noise becomes more significant, more molecules escape due to shot noise fluctuations, and the mean residence time and the molecular occupancy are decreased.

As the laser power is adjusted, in addition to the changes in the experimentally measureable autocorrelation, the inset of Fig. 7 shows that there are changes in the mean concentration of molecules in the detection volume. This would be difficult to directly measure experimentally but is easily obtained in the simulation by accumulating a histogram of molecular positions for each diffusion time step Δt_D. For constant flow, the concentration profile is constant at a value of $C_0 = 6 \times 10^{-6}$ molecules per grid point, whereas for diffusion, the profile exhibits molecular shot noise and varies spatially and from run to run around this value. When the trap is operating, the concentration profile has a peak at the origin, which is clearly visible in the graph. Note that the laser power of 30 μW produces the tightest and tallest profile, with a peak of $\sim 7 \times 10^{-4}$ molecules per grid point, which is equivalent to a concentration increase by over a factor of 100.

Some statistical data from the latency and laser power studies of Figs. 6 and 7 are shown in Fig. 8. In the simulation, one can follow each molecule individually to gather statistical information, such as the number of fluorescence photons that are detected from that molecule and the time between entry and exit from the detection volume. Figure 8 plots the mean occupancy time and the mean number of photons collected from each molecule against the laser power or the latency. This figure demonstrates again that a power of 30 μW provides the longest occupancy time. Higher laser powers result in collection of a similar number of photons, but within a shorter occupancy time, due to faster photobleaching. The figure also demonstrates that for a laser power of 30 μW, the trapping is effective if the latency is below $\sim 1 \times 10^{-4}$ s. In comparison, the mean time for acquisition of $N=6$ photons required by the algorithm is $\sim 4.3 \times 10^{-5}$ s, and the mean time to diffuse out of the detection region is $\sim 6 \times 10^{-4}$ s.

A study of the effects of power imbalance between the two laser beams was conducted using simulations. If there is a power imbalance of between about +20% (i.e., 12 μW and 18 μW) and −5% (i.e., 15.75 μW and 14.25 μW), the trap-

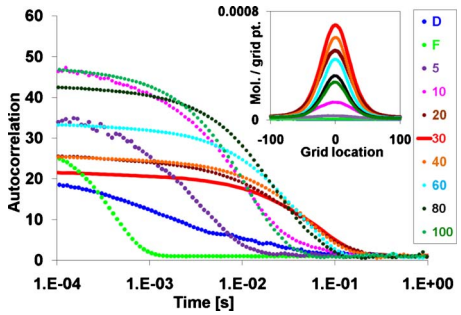

Fig. 7 Autocorrelation functions for free diffusion (D, blue) and for constant electrokinetic flow (F, green), each at a laser power of $\bar{P}$ = 30 μW, and for trapping for a range of laser powers from 5 μW to 100 μW, all with feedback latency of 6×10^{-6} s. The inset shows the mean number of molecules per grid point (Δx=0.01 μm) under the same conditions. (Color online only.)

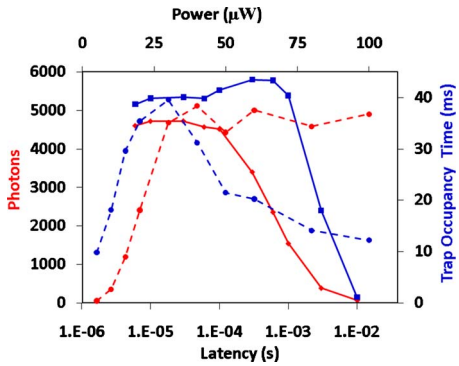

Fig. 8 Effect of laser power and latency of feedback on the trapping performance. The red curves show the mean number of photons detected (photons) before the molecule photobleaches or escapes versus latency (solid line, bottom scale) and versus power $\bar{P}$ (dashed line, top scale). The blue curves show the mean time that a molecule remains in the trap (trap occupancy time) versus latency (solid line) and power (dashed line). (Color online only.)

ping is still effective in that the autocorrelation function and the statistics of the trapping time remain the same, but the center of the trap shifts slightly, as may be seen in the concentration profiles in Fig. 9. However, if the imbalance is higher, molecules escape from the low power end, and the trap is less effective. If a molecule escapes to the left, the trapping algorithm switches on the flow to reload the trap, and the molecule is brought back to the center and retrapped. Hence, an improvement in trapping statistics is found if the downstream laser beam has slightly higher power.

As discussed at the end of Sec. 2.1 (Fig. 2), good trapping depends on effective time-gated photon detection, and one expects temporal cross talk to increase and the trapping to become poor if the fluorescence lifetime of the molecule is long compared to the 6.6-ns interval between laser pulses. This is indeed the case, as seen in Fig. 10, which shows the mean number of photons and the mean trapping time per molecule as a function of fluorescence lifetime, and also the fraction of photons that have incorrect timing (odd time-stamp instead of even, or vice versa) as a function of fluorescence lifetime. The trapping performance deteriorates if the fluorescence lifetime is longer than about 3 ns. Also, simulations have verified the experimental finding that good trapping is dependent on correct timing delays (cable lengths)—i.e., the mean shift of 3σ discussed at the end of Sec. 2.1 must be correctly set within the range of about −0.5 ns to +1.0 ns, as seen in the inset of Fig. 10, which is for a fluorescence lifetime of 3 ns.

Simulations indicate that the trapping is predicted to be effective for a wide range of sample concentrations from <1 pM up to >0.1 nM, but as the concentration increases, trapped molecules are increasingly displaced by others that diffuse into the trap, as described with Fig. 5 (see top figure labeled "two molecules in trap"). This is especially the case for concentrations >1 nM or if photostability is improved. In an experiment that uses a concentration >1 nM, it would be difficult to determine whether extended photon bursts are due to trapping of single molecules with enhanced photostability or to trapping of a series of molecules in succession. Also, as mentioned at the end of Sec. 2.2, simulations find that for a smaller value of diffusion D, trapping is more easily achieved, i.e., parameters such as the fluorescence lifetime or timing delay may be varied over a wider range while still maintaining effective trapping.

The simulation results presented so far have assumed that an electrokinetic flow of $v_F^{\max}=2$ μm/ms is achieved for the maximum applied voltage. This value was varied to study the predicted effectiveness of the trap for molecules with different electrokinetic mobilities. The autocorrelation width, which measures the mean residence time of molecules in the trap, remains about the same for values of $v_F^{\max}$ from 1 to 3 μm/ms, while the amplitude decreases with $v_F^{\max}$, as might be expected for faster reloading of the trap, which increases the mean occupancy of the trap. However, for $v_F^{\max}=0.5$ μm/ms or lower, the autocorrelation width decreases as escape from the trap increases. The same applies also for $v_F^{\max}=4$ μm/ms or higher, due to overcompensation of Brownian diffusion, and in this case, improved performance might be expected from a more sophisticated trapping algorithm that applies corrective voltages for limited time durations, so that molecules are not transported out of the trap in the time between photons.

4 Conclusions

The results show that single-molecule trapping in a nanochannel by control of electrokinetic flow to counteract Brownian diffusion is feasible for an experimental setup. A simple control algorithm that uses the timing of detected photons to determine adjustments of the flow for trapping is evaluated. While accommodating the limitations of a maximum electrokinetic flow of about $v_F^{\max}=2$ μm/ms and a mean count rate of $\sim 1.4\times 10^5$ photons s^{-1} from a molecule at the center of the detection volume, it is possible to hold a small rapidly diffusing molecule within a micron-sized confocal probe region for a prolonged time, usually until photobleaching occurs. The trap is robust in that it is possible to rapidly reload and trap a sequence of individual molecules over a broad

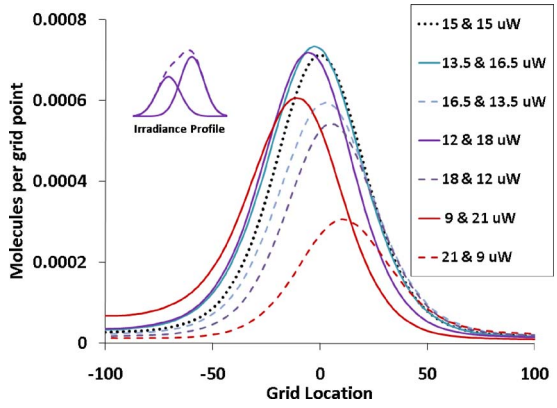

Fig. 9 Time-averaged concentration profile of trapped molecules or the mean number of molecules per grid point ($\Delta x=0.01$ μm) for different values of laser powers (μW) of the two beams. The inset shows the irradiance profile for a +20% power imbalance, i.e., 12 μW and 18 μW.

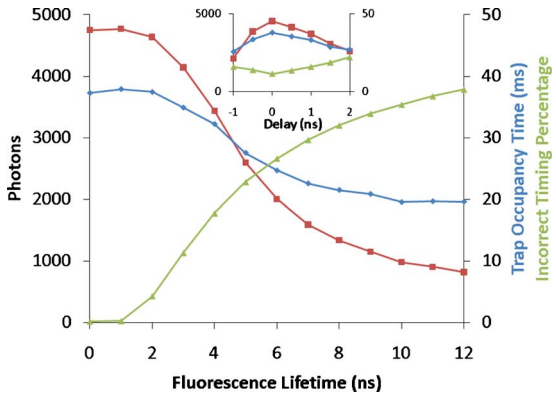

Fig. 10 Effect of fluorescence lifetime on the trapping performance. The red curve shows the mean number of photons detected (photons) before the molecule photobleaches or escapes, the blue curve shows the mean time that a molecule remains in the trap (trap occupancy time), and the green curve shows the percentage of fluorescence photons that have incorrect timing (incorrect timing percentage). The inset shows the effect of an incorrect timing delay on the trapping performance for a fluorescence lifetime of 3 ns. (Color online only.)

range of experimentally achievable parameters. Studies with the simulation show that the anticipated latency of the control does not hinder performance and that trapping should be achievable provided the latency is below $\sim 100\ \mu s$.

By examination of the autocorrelation function of detected photons and collation of statistical data from individual molecules, it is found that there is a most favorable laser excitation power ($\sim 30\ \mu W$) for which the performance of the trap is optimum. If the laser power is reduced $\sim$50% below this point so that the fluorescence signal falls below $\sim 7 \times 10^4$ photons s^{-1}, then the possibility of escape due to photon shot-noise fluctuations increases, and the trap begins to fail. Similarly, if the laser power is increased by $\sim$50% above this point, the rate of photobleaching increases so that the occupancy time of molecules within the trap is reduced, although the mean number of photons detected from each molecule is retained. The trap performance would improve if the rate of photobleaching were decreased, for example, by addition of oxygen scavengers to the solution. In preliminary experiments, molecules in nanochannels appear to have improved photostability compared to those in microchannels or in bulk solution.[13]

The algorithms for simulating single-molecule detection reported in this paper are applicable to a wide variety of experiments, including studies of molecular interactions for high-throughput screening.[28] An extension of the simulation to study trapping with two-photon excitation and also trapping in three dimensions is under way. The approach involves use of four laser foci arranged in a tetrahedron to provide 3-D spatial information and also four electrodes arranged in a tetrahedron to provide 3-D electrokinetic motion.[17]

Acknowledgments

We thank Zbigniew Sikorski for helpful discussions in the early part of this work, and acknowledge support from DARPA Grant No. W911NF-07-1-0046, NIH Grant No. EB-006639, NSF Grant No. 0619789, and the Center for Laser Applications. The contents of this paper are solely the responsibility of the authors and do not necessarily represent the official views of the NIH.

References

1. J. Enderlein, "Tracking of fluorescent molecules diffusing within membranes," *Appl. Phys. B* **71**, 773–777 (2000).
2. A. J. Berglund and H. Mabuchi, "Tracking-FCS: fluorescence correlation spectroscopy of individual particles," *Opt. Express* **13**, 8069–8082 (2005).
3. K. Kis-Petikova and E. Gratton, "Distance measurement by circular scanning of the excitation beam in the two-photon microscope," *Microsc. Res. Tech.* **63**, 34–49 (2003).
4. V. Levi and E. Gratton, "Exploring dynamics in living cells by tracking single particles," *Cell Biochem. Biophys.* **48**, 1–15 (2007).
5. G. A. Lessard, P. M. Goodwin, and J. H. Werner, "Three-dimensional tracking of individual quantum dots," *Appl. Phys. Lett.* **91**, 224106 (2007).
6. N. P. Wells, G. A. Lessard, and J. H. Werner, "Confocal, three-dimensional tracking of individual quantum dots in high-background environments," *Anal. Chem.* **80**, 9830–9834 (2008).
7. C. Gosse and V. Croquette, "Magnetic tweezers: micromanipulation and force measurement at the molecular level," *Biophys. J.* **82**, 3314–3329 (2002).
8. A. Ashkin, "Optical trapping and manipulation of neutral particles using lasers," *Proc. Natl. Acad. Sci. U.S.A.* **94**, 4853–4860 (1997).
9. K. C. Neuman, T. Lionnet, and J. F. Allemand, "Single-molecule micromanipulation techniques," *Annu. Rev. Mater. Res.* **37**, 33–67 (2007).
10. A. E. Cohen, "Control of nanoparticles with arbitrary two-dimensional force fields," *Phys. Rev. Lett.* **94**, 118102 (2005).
11. A. E. Cohen, "Trapping and manipulating single molecules in solution," Ph.D. Dissertation, Stanford University (2006).
12. A. E. Cohen and W. E. Mourner, "Controlling Brownian motion of single protein molecules and single fluorophores in aqueous buffer," *Opt. Express* **16**, 6941–6956 (2008).
13. L. M. Davis, B. K. Canfield, X. Li, W. H. Hofmeister, I. P. Lescano-Mendoza, B. W. Bomar, J. P. Wikswo, D. A. Markov, P. C. Samson, C. Daniel, Z. Sikorski, and W. Robinson, "Electrokinetic delivery of single fluorescent biomolecules in fluidic nanochannels," *Proc. SPIE* **7035**, 70350A (2008).
14. W. E. Mourner, "New directions in single-molecule imaging and analysis," *Proc. Natl. Acad. Sci. U.S.A.* **104**, 12596–12602 (2007).
15. W. A. Lyon and S. M. Nie, "Confinement and detection of single molecules in submicrometer channels," *Anal. Chem.* **69**, 3400–3405 (1997).
16. J. T. Mannion and H. G. Craighead, "Nanofluidic structures for single biomolecule fluorescent detection," *Biopolymers* **85**, 131–143 (2006).
17. L. M. Davis, Z. Sikorski, W. Robinson, G. Shen, X. Li, B. Canfield, I. Lescano, B. Bomar, W. Hofmeister, J. Germann, J. King, Y. White, and A. Terekhov, "Maximum-likelihood position sensing and actively controlled electrokinetic transport for single-molecule trapping," *Proc. SPIE* **6862**, 68620 (2008).
18. E. B. Shera, N. K. Seitzinger, L. M. Davis, R. A. Keller, and S. A. Soper, "Detection of single fluorescent molecules," *Chem. Phys. Lett.* **174**, 553–557 (1990).
19. D. H. Bunfield and L. M. Davis, "Monte Carlo simulation of a single molecule detection experiment," *Appl. Opt.* **37**, 2315–2326 (1998).
20. L. M. Davis, J. G. K. Williams, and D. T. Lamb, "Computer simulation of gene detection without PCR by single molecule detection," *Proc. SPIE* **3570**, 282–293 (1999).
21. T. Wohland, R. Rigler, and H. Vogel, "The standard deviation in fluorescence correlation spectroscopy," *Biophys. J.* **80**, 2987–2999 (2001).
22. L. M. Davis, P. E. Williams, D. A. Ball, E. D. Matayoshi, and K. M. Swift, "Data reduction methods for application of fluorescence correlation spectroscopy to pharmaceutical drug discovery," *Curr. Pharm. Biotechnol.* **4**, 451–462 (2003); **5**, 481–481 (2004).
23. L. M. Davis and G. Q. Shen, "Accounting for triplet and saturation effects in fluorescence correlation spectroscopy measurements," *Curr. Pharm. Biotechnol.* **7**, 287–301 (2006).
24. M. T. Tyn and T. W. Gusek, "Prediction of diffusion coefficients of proteins," *Biosens. Bioelectron.* **35**, 327–338 (1990).
25. S. A. Soper, E. B. Shera, L. M. Davis, H. L. Nutter, and R. A. Keller, "The photophysical constants of several fluorescent dyes pertaining to ultrasensitive fluorescence spectroscopy," *Photochem. Photobiol.* **57**, 972–977 (1993).
26. A. Spinelli, L. M. Davis, and H. Dautet, "Actively quenched single photon avalanche diode for high repetition rate time-gated photon counting," *Rev. Sci. Instrum.* **67**, 55–61 (1996).
27. K. Fogarty and A. Van Orden, "Two-beam fluorescence cross-correlation spectroscopy for simultaneous analysis of positive and negative ions in continuous-flow capillary electrophoresis," *Anal. Chem.* **75**, 6634–6641 (2003).
28. P. Song, L. M. Davis, and G. R. Bashford, "Single molecule diffusion coefficient estimation by image analysis of simulated CCD images to aid high-throughput screening," in *Proc. 31st Annual International Conference of the IEEE Engineering in Medicine and Biology Society*, pp. 1396–1399 (2009).

APPENDIX 2

L. M. Davis and W. N. Robinson, “Simulations for Guiding the Delivery and Trapping of Single Biomolecules in a Nanofluidic Device,” Proc. SPIE 7750, 775005 (2011).

This paper proceeded from an invited talk at Photonics North 2010 given by Dr. Lloyd Davis.

Invited Paper

Simulations for Guiding the Delivery and Trapping of Single Biomolecules in a Nanofluidic Device

Lloyd M. Davis*, and William N. Robinson,

Center for Laser Applications, University of Tennessee Space Institute,
Tullahoma, TN 37388

ABSTRACT

A microfluidic device has been developed wherein single molecules in solution are electrokinetically transported along a nanochannel. The nanochannel is irradiated by two adjacently focused laser beams so that the timing of fluorescence photons induced by each beam indicates the position of a molecule along the nanochannel. This is then used to actively control the electrokinetic flow, so that the molecule may be held within the confocal volume for a prolonged time and then rapidly replaced following photobleaching or completion of the single-molecule measurement. Here we focus on Monte Carlo computer simulations of the physical processes that occur during the delivery and trapping. The simulations help in understanding the constraints imposed by experimental limitations, such as the latency of feedback, the maximum achievable speed of electrokinetic flow, and photophysical processes such as triplet crossing and photobleaching. They also aid in evaluating the effects of shot noise and photon timing error and in predicting optimum experimental operating parameters. Studies indicate that the 6 μs latency of feedback in our experiments is well below that required for stable trapping (~100 μs); for small freely diffusing molecules, a limited flow speed of ~2 μm/ms can result in ~10–20 % of molecules escaping before they photobleach; there is an optimum laser power of ~30–40 μW that provides a sufficient rate of fluorescence photons for trapping while reducing loss due to photobleaching; an increase in the spacing between the beams or increase in relative power of the down-stream beam increases the trapping time.

Keywords: Single-molecule, nanochannel, electrokinetic trapping, Monte Carlo simulation, fluorescence spectroscopy, photon counting, pulse-interleaved excitation, nanofluidics

1. INTRODUCTION

The detection of single fluorescently labeled biomolecules in solution, such as proteins and antibodies, has become vital to the study of biophysical processes on the molecular level. Impressive progress has been made in the field [1] since the first measurements two decades ago [2]. Single-molecule detection is often achieved by photon burst detection within a confocal fluorescence microscope as this technique can provide a sub-femtoliter excitation volume to achieve signal-to-noise that is superior to that from wide-field imaging; however, for studies in solution, the molecules rapidly diffuse through the focal region. Tethering of molecules to a surface or to a bead is not always possible or desirable as it can alter stereochemical access and molecular interaction behavior. Therefore, a means of constraining the molecule of interest to a small volume is needed, in addition to methods for opposing Brownian motion and controlling the motion and environment of the molecule.

Optical trapping is not suitable for use with a molecule much smaller than ~ 100 nm as it requires intense irradiance that can cause heating or photodamage. As an alternative, Cohen and Moerner have developed the Anti-Brownian Electrokinetic (ABEL) trap, in which the solution is constrained between fused silica surfaces with sub-micron spacing, and the observed Brownian motion in the plane of the fluid sample is countered by a two-dimensional electrokinetic motion, which results from adjustment of voltages at four electrodes surrounding the probe region [4]. When a molecule in solution is confined to a thin volume between two planar interfaces for trapping in 2-D, it suffers a high rate of collisions with the surfaces [4]. For molecular applications that can tolerate such disturbances, a 1-D trap should be equally useful, because the collision rate is not significantly increased by confinement of the molecule to a one-dimensional channel of similar dimensions. A 1-D nanochannel also has the advantage of being easily adaptable to adjustment of the flow for rapid replacement of a molecule following photobleaching or completion of the single-

* ldavis@utsi.edu; phone 1 931 393-7335; www.utsi.edu/ldavis

Photonics North 2010, edited by Henry P. Schriemer, Rafael N. Kleiman, Proc. of SPIE Vol. 7750,
775005 · © 2010 SPIE · CCC code: 0277-786X/10/$18 · doi: 10.1117/12.871823

molecule measurement. Hence electrokinetic trapping within a nanochannel offers a means for prolonged studies of conformational changes and interactions and for rapidly collecting statistical information from a succession of many individuals.

Various techniques for creation of well-defined nanofluidic networks have been demonstrated since the early 1990's [5,6], and excellent reviews on different methods for fabrication of nanochannels, fluidic transport, and applications have been published in recent years [7–10]. Nanoscale features are becoming an important component in modern lab-on-a-chip technologies for interrogating single molecules [11]. Nanofluidic structures have been fabricated from transparent materials for use as a platform for fluorescence studies of single biomolecules [12]. The nanochannel constrains the solution within a small volume, and voltages applied across the ends of the channels can electrokinetically control the transport of the molecules along the channels [13,14].

There has been increasing interest in single-molecule trapping in solution [15]. Our group has reported initial experiments on single-molecule detection with actively controlled electrokinetic transport of the solution within a nanochannel in a device fabricated from fused silica [16]. We have also described maximum-likelihood data analysis strategies for sensing the position of a single molecule within a trap [17] and for single emitter localization in 3-D to sub-diffraction precision [18].

The present paper focuses on results from Monte Carlo computer simulations of our experiments in Ref. [16] on the successive delivery and 1-D trapping of single molecules within a nanochannel. Numerical algorithms of the simulations and results for trapping fast diffusing molecules are detailed in Ref. [19]. The simulations have been helpful in validating our experimental results to date and are being used to guide future experiments. They provide a means for developing and testing algorithms that may be implemented in software within a field programmable gate array (FPGA), which is a part of the hardware for controlling the electrokinetic voltages of the single-molecule trap. The simulation also enables the robustness of the trap to be studied under different experimental conditions. The use of Monte Carlo simulations for validating experiments and determining feasibility limits was described in the first reports on the detection of single-chromophore molecules in solution [2]. Later simulations have been used to study efficiency of detection [20], two-color coincidence detection limits [21], and the efficiency of neural network analysis for distinguishing single molecules with different spectroscopic properties [22].

Section 2 presents an overview of the experiments and results. Section 3 discusses the important features of the simulations and explains the principles of key parts of the algorithms. Algorithms for trapping are discussed in Section 4. Section 5 presents results of the simulations and Section 6 presents conclusions.

2. EXPERIMENTS AND RESULTS

The nanochannels and microfluidic device are fabricated by reactive ion etching of fused silica wafers by standard photolithographic methods, as discussed in Ref. [23]. Images of the microfluidic device and nanochannels during their construction are shown in Figure 1. Figure 1(a) shows an optical microscope image of the two V-shaped microchannels, which connect 2 sets of 2 reservoirs with laser-drilled vias. The two microchannels are connected by a number of nanochannels, seen during construction in the scanning electron microscope (SEM) image in Figure 1(b). The nanochannels are etched to a depth of ~100 nm and are protected by a layer of photoresist during etching of the ~2-micron deep microchannels, hence there are nanoscale structures protruding into the microchannels. A dual-beam focused ion beam/SEM was used to mill a cross-section of a nanochannel of a bonded device, which is shown in Figure 1(c).

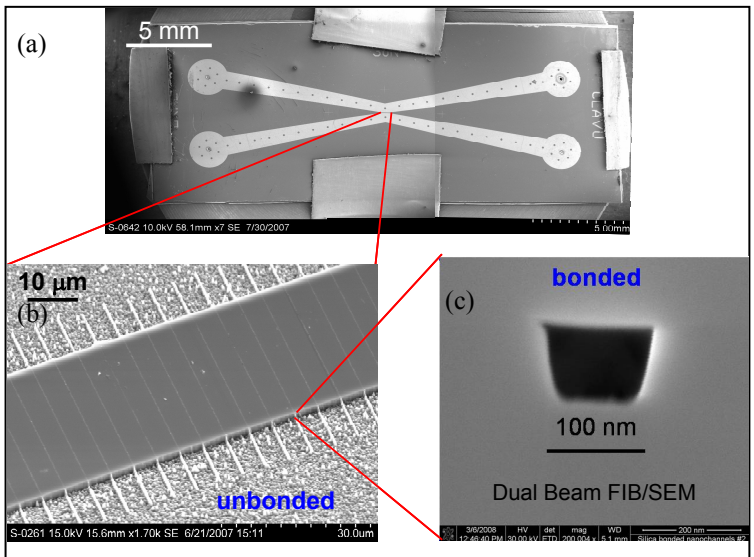

Figure 1: Optical and scanning electron microscope images of the microchannels and nanochannels.

The chip, which is ~1 cm × 5.5 cm, is mounted between acrylic and aluminum blocks, with o-rings sealing connections to the fluidic inputs, and is positioned on the stage of a custom-built single-molecule microscope, as shown in Figure 2.

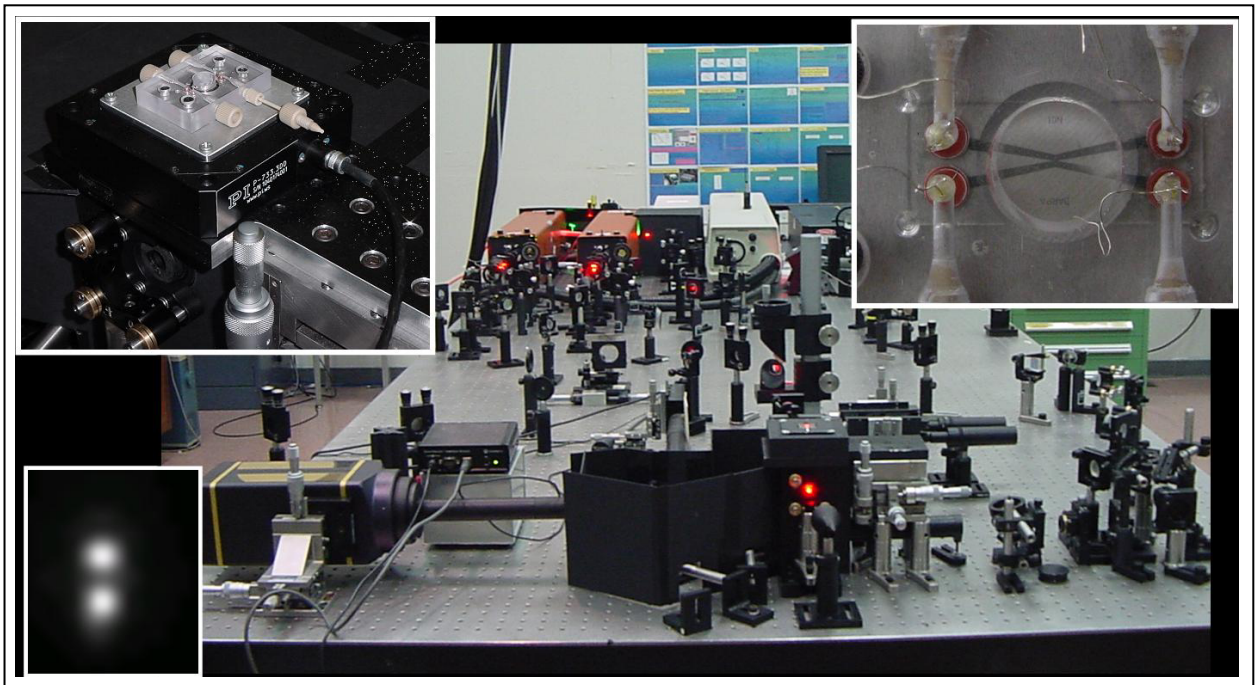

Figure 2: Photographs of the experimental set-up: The single-molecule microscope is at the front of the optical table; the microfluidic device mounted on the stage of the microscope is at top left; a photo of the V-shaped microchannels is at top right; an intensified-CCD image of the two laser beams focused along a nanochannel is at bottom left.

Photon burst detection of single molecules may be accomplished within a microchannel or a nanochannel. Figure 3 illustrates that the width of the autocorrelation function, which is a measure of the mean residence time of molecules

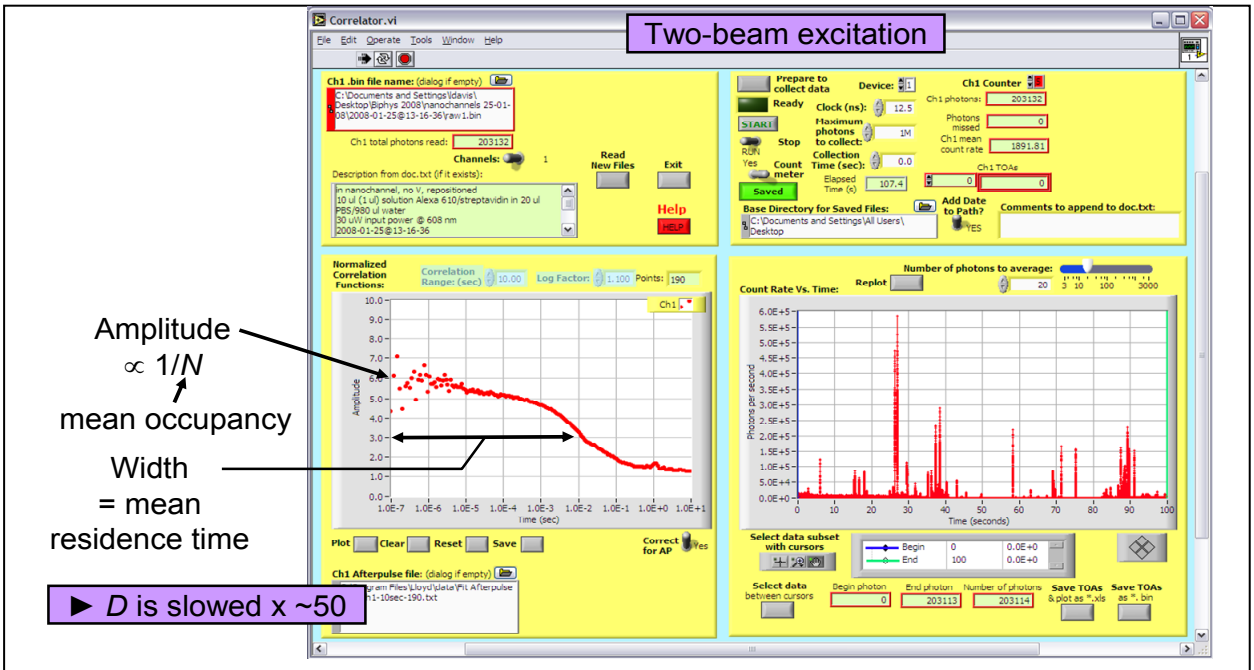

Figure 3: Photon bursts and normalized autocorrelation function form a solution of Streptavin-Alexa 610 within a nanochannel.

within the confocal volume, is increased when observing molecules in a nanochannel as compared to a microchannel, indicating that the diffusion coefficient is slowed by a factor of about 50. This is in concurrence with the observations of others [24]. When a constant voltage is applied across the nanochannel, the autocorrelation function displays a reduced width as a result of molecules being electrokinetically transported through the confocal volume.

Trapping of a single molecule is achieved by activating a program within a field programmable gate array (FPGA) circuit, which actively controls the electrokinetic voltage. When the trap is turned on, the width of the autocorrelation function broadens considerably, as shown in Figure 4. Also, the amplitude of the autocorrelation function decreases slightly, indicative of a higher mean occupancy of the confocal volume, as one would expect if a new molecule is rapidly loaded into the trap as soon as the previous one photobleaches.

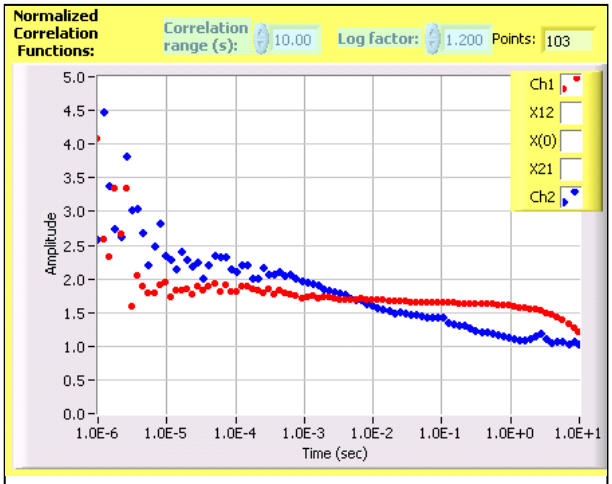

Figure 4: The autocorrelation functions obtained under conditions of free diffusion (blue) and active trapping (red).

3. TRAPPING ALGORITHMS

The algorithm for the FPGA program applies a voltage proportional to the difference between the numbers of photons in each of the two time channels corresponding to each laser focus, as illustrated in Figure 5 (V=6(R–3)). As shown in Figure 4, this algorithm successfully extends the residence time of molecules that have slowed diffusion. A possible contributing factor for slowed diffusion is that molecules stick to the walls of the nanochannel, as the experiments find that background from immobile molecules increases over the course of several hours [16]. Sticking and slow down of diffusion could possibly be avoided by surface treatments and future experiments will investigate trapping of small freely diffusing molecules in treated nanochannels.

The use of our simulations described below has determined that trapping would be more effective if the FPGA program were to use an alternate algorithm, which is illustrated in Figure 6. This algorithm applies the maximum voltage to return a molecule to the center of the trap with the maximum possible electrokinetic velocity ($\pm v_F^{\max}$), which is estimated to be ~2 μm/ms [19]. The results of the simulations presented below in Section 5 consider this alternate trapping algorithm.

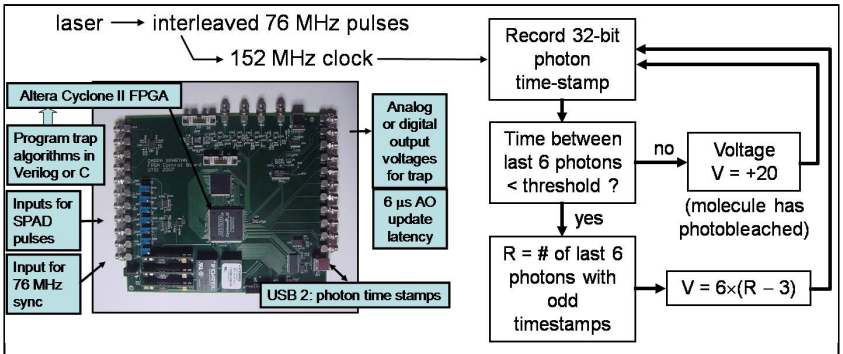

Figure 5: The FPGA is clocked synchronous to the pulse-interleaved laser excitation and programmed with an algorithm shown at lower right so as to provide the voltage levels for the electrokinetic transport of molecules along the nanochannel.

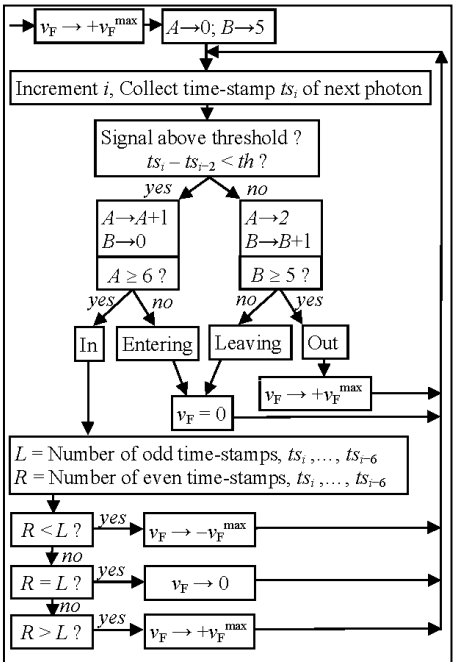

Figure 6: Alternate trapping algorithm, which applies the maximum possible electrokinetic velocity to compensate for diffusion.

4 SIMULATION ALGORITHMS

In this section, a description of features of the algorithms used in the simulation code is given. Complete details of the simulation algorithms and of the equations used to describe all the physical processes are reported in Ref. [19].

An important factor in creating a useful program is ensuring sufficient speed for repeated execution through many different sets of parameters for long periods of time so as to gather statistically meaningful results. For trapping, the precise timing of each detected photon must be generated by the simulation, as the trapping algorithm begins by sorting photons into channels on the basis of their timing. This requires an approach different from that used in early simulations of single-molecule detection, where the code used random-number calls to generate the numbers of detected photons in subsequent time bins, rather than the timing of each photon.

To address the challenge of developing a fast algorithm that generates precise timing of each photon, in the parts of the code that model the photophysics, time is treated as a real continuous variable, rather than being incremented in discrete steps. Appropriately distributed random numbers are used to find the waiting times from one photophysical event to the next. For example, after a molecule is excited, if it decays with detection of a fluorescence photon, one fetches an exponentially distributed random real number with mean equal to the fluorescence lifetime $X_{EXP}(\tau_F)$ to determine when the molecule returns to the ground state. To determine the time of detection of the photon, another random number with a Gaussian distribution is added to account for the timing jitter of the detector. As another example, as illustrated in Figure 7(a), if there is a molecule in the ground state at a given location in the nanochannel, one evaluates (or looks up) the probabilities P_1 and P_2 that the molecule would be excited by the next pulse in beam 1 or beam 2. One could fetch a uniformly distributed random real number X_U to test if it is less than P_1, then fetch another X_U to test if it is less than P_2, and keep repeating this until success is achieved, wherein the molecule becomes excited. However, it is statistically equivalent and much more efficient to generate two geometrically distributed random integers with probabilities of success P_1 and P_2, $I_G(P_1)$ and $I_G(P_2)$, as shown in Figure 7(b), then check which random integer is smaller to determine the number of laser pulses that one must wait for the molecule to become excited. Note however, that if the molecule moves to a new location with different P_1 or P_2 before excitation occurs, then one must revaluate the integers $I_G(P_1)$ and I_G (P_2) and repeat the test. We use the Intel Math Kernel Library routine viRngGeometric to fetch geometrically distributed random numbers and similar routines for other distributions. We find that the code runs much faster when recompiled with the 2010 Intel compiler compared to Microsoft C/C++ Visual Studio 2008.

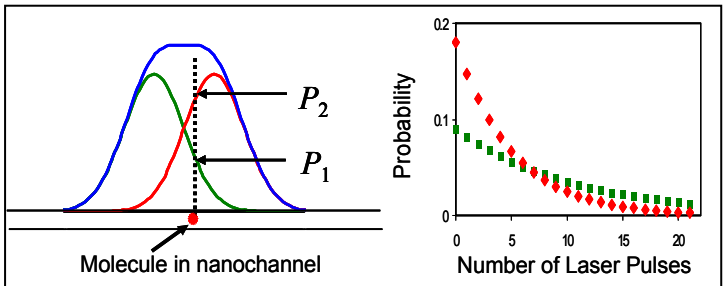

Figure 7: (a) A molecule in the nanochannel has probabilities P_1 and P_2 of being excited by each laser beam. (b) Probability densities of geometrically distributed random integers with probabilities of success P_1 and P_2.

To model molecular transport along the nanochannel, we consider molecules localized to a 1-D grid, which is fine compared to the size of the focused laser beams. As shown in Figure 8, for constant electrokinetic flow (top of Figure 8), each molecule jumps to the next point on the grid at fixed time intervals of $\Delta t_F = \Delta x / v_F$, where Δx is the grid spacing and v_F is the flow velocity. To model Brownian diffusion, each molecule jumps to a randomly selected nearby point at fixed time intervals of $\Delta t_D = \Delta x^2 / (2D)$, where D is the diffusion coefficient (middle of Figure 8). Molecules may jump off the end of the grid in a number of different ways (left end of middle of Figure 8), and hence to exactly compensate and maintain a constant concentration outside of the trapping region, a new molecule is introduced to a random point near the end of the grid at waiting intervals that are geometrically distributed random integers multiplied by Δt_D. Details are discussed in Ref. [19]. In modeling trapping

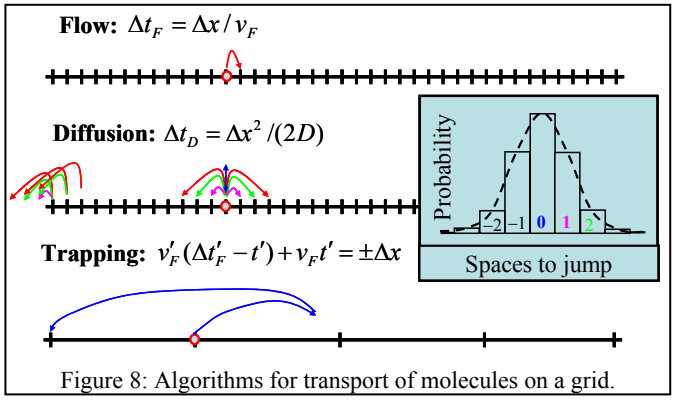

Figure 8: Algorithms for transport of molecules on a grid.

(bottom of Figure 8), the time and direction of the next flow step are re-evaluated whenever the flow velocity is changed. For example, if the flow velocity is changed from v_F to v_F' at a time t' following the last flow time-step, then the time until the next flow step is $\Delta t_F'$ such that $v_F'(\Delta t_F' - t') + v_F t' = \pm\Delta x$.

The overall simulation algorithm must synchronize the various physical processes that occur in the experiment. Whenever the time is reached for occurrence of a process, the simulation evaluates the waiting time until the next occurrence of that particular process. It then finds which process occurs next by using the Intel Math Kernal Library routine idamin to find the process with the minimum time, as illustrated schematically in Figure 9.

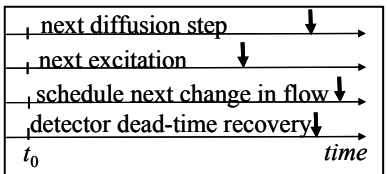

Figure 9: Synchronization of various processes in the simulation.

5. SIMULATION RESULTS

Simulations under the conditions of the experiments with slowed diffusion ($D = 4.4 \times 10^{-8}$ cm^2 s^{-1}) indicate that trapping of single molecules is readily achievable and leads to results by and large consistent with experimental findings. Figures 10–13 show the autocorrelation functions (on left) and photon bursts (on right) that are obtained from analysis of binary files of photon time stamps created by simulations by use of the LabView "Correlator.vi" program used in experiments.

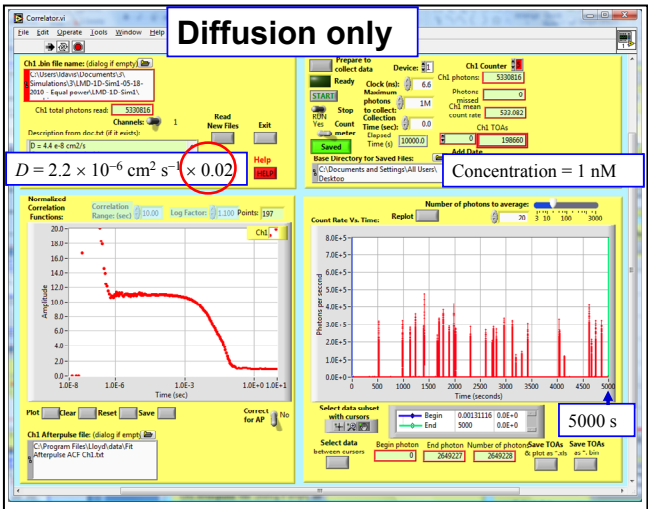

Figure 10: Simulation results for transport by diffusion only.

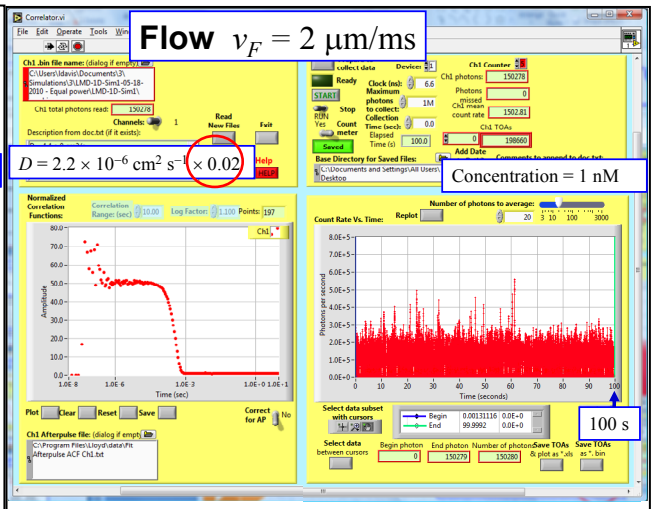

Figure 11: Simulation results for transport by steady flow.

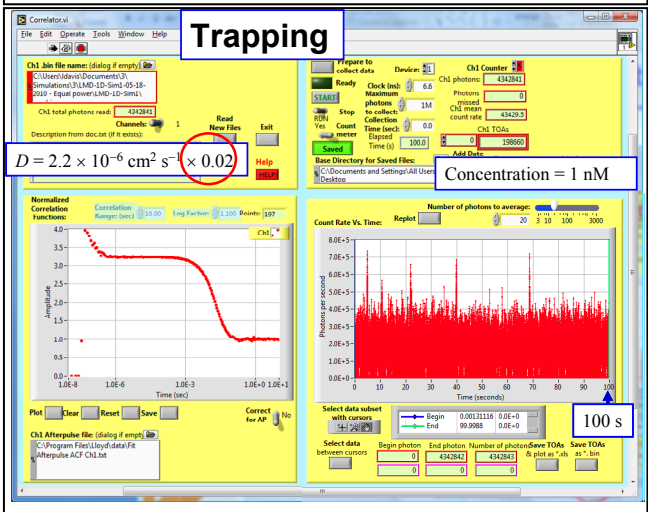

Figure 12: Simulation results for controlled flow for trapping.

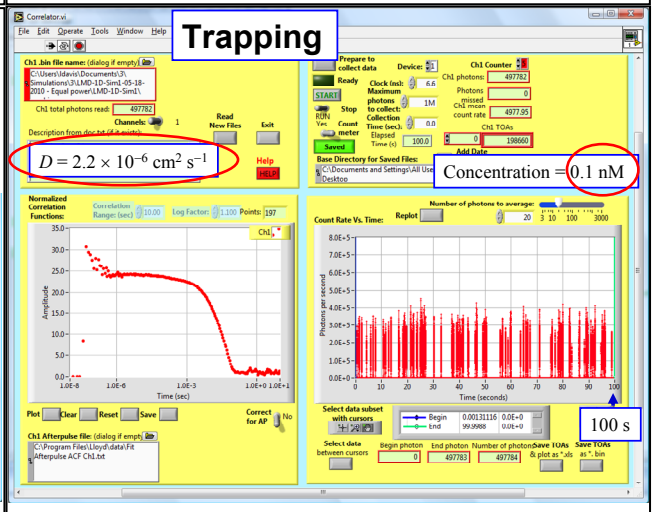

Figure 13: Simulation results for trapping with fast diffusion.

Figure 10 shows the results from a simulation of 5000 s (1 hr 23 min) of experimental data collection for transport by diffusion only with a sample concentration of 1 nM. Due to the relatively slow transport of molecules and low concentration, photon bursts are seen from only ~30 molecules (~0.006 per second) and results vary from run to run due to molecular shot noise. The autocorrelation has a width of ~10^{-2} s, in agreement with experimental results of Figure 4.

Figure 11 shows that when a steady electrokinetic flow of v_F = 2 μm/ms is applied, molecules are swiftly transported through the confocal volume to yield ~12 photon bursts per second and an autocorrelation function with a truncated width of < 10^{-3} s, in agreement with experimental results given in Ref. [16]. Note that in the photon burst plot (right of Figure 11) the photon count rate sometimes spikes higher as molecules sometimes overlap in the detection volume.

Figure 12 shows the results of trapping under the same conditions. There are ~8 photon bursts per second. The autocorrelation width increases and the amplitude decreases from that of constant flow because trapping causes the mean occupancy of the confocal volume to increase. The width of the autocorrelation and the rate of new molecules depends on the photobleaching quantum efficiency (here 10^{-5}). The increased width of the experimental autocorrelation shown in Figure 4 suggests that the photostability of molecules in a nanochannel is increased from that in bulk solution. However, note that long photon bursts also result when the concentration is sufficiently high that molecules overlap within the trap.

Figure 13 shows results of trapping fast diffusing molecules with $D = 2.2 \times 10^{-6}$ cm^2 s^{-1}. To reduce the probability of molecules overlapping in the trap, the concentration is reduced to 0.1 nM.

Further simulation studies on the trapping of fast diffusing molecules are reported in detail in Ref. [19] and have investigated the effects of (a) the delay or latency in the adjustment of flow, (b) the laser power, (c) the fluorescence lifetime of the emitter, (d) timing shift due to cable delays, (e) detector afterpulsing, dead-time, and background, and (f) mismatch of laser power between the two beams. Detailed statistical information on individual molecules, such as the time in the trap and number of photons detected per molecule, as well as ensemble behavior exhibited by the autocorrelation function and the time-averaged molecular concentration profile within the trap are reported. Conclusions from these studies for fast diffusing molecules include that triplet crossing, background counts, detector dead time and afterpulses do not hinder trapping; the 6 μs latency of feedback in our experiments is well below that required for stable trapping (~100 μs); the maximum flow speed of ~2 μm/ms presents a limitation that results in ~10–20 % of molecules escaping before they photobleach; there is an optimum laser power of ~30–40 μW that provides a sufficient rate of fluorescence photons for trapping while reducing loss due to photobleaching; the probability of escape from the trap before photobleaching greatly increases if the fluorescence lifetime of the emitter is more than ~3–4 ns or if the timing delay is not set within the range of –0.5 to +1.0 ns from the correct setting. (For slowed diffusion, the trap remains effective even for a fluorescence lifetime of ~100 ns and for a wider range of timing delays of about –1.0 to +2.5 ns.)

In supplement to the results of Ref. [19], Figure 14 shows the effects of varying the separation between the laser foci.

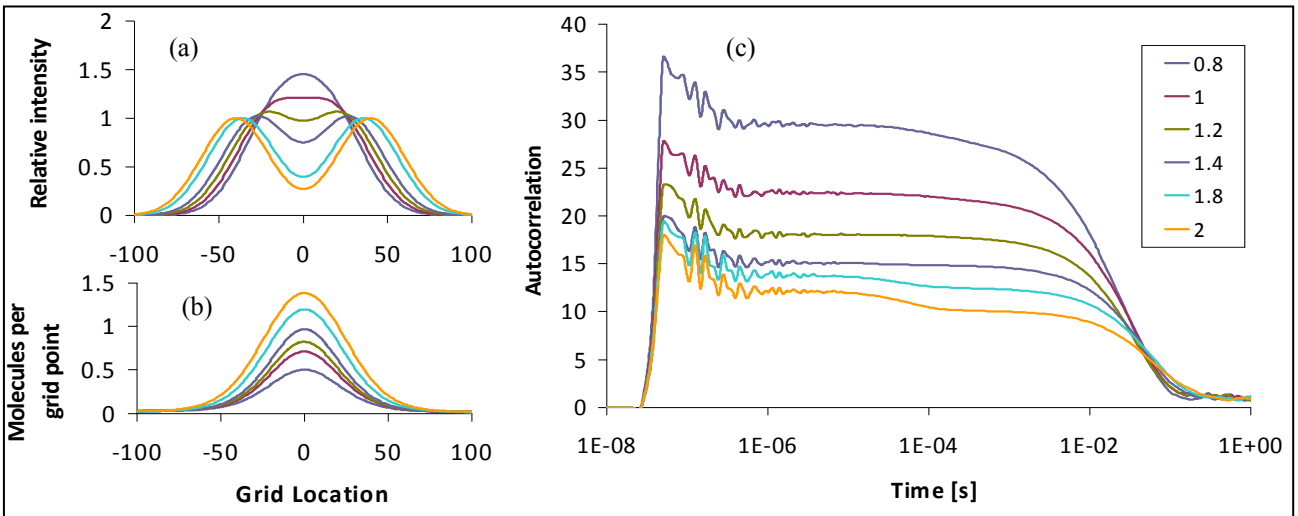

Figure 14: Effect of variation of the relative separation of the two laser spots, where 1.0 corresponds to a spacing equal to the beam waist (0.5 μm). (a) Intensity profiles; (b) Time-averaged concentration profiles within the trap; (c) Autocorrelation functions.

The intensity profile (Figure 14 (a)) has a flat top when the laser foci are separated by a distance equal to the beam waist, so the fluorescence excitation does not vary as the position of the molecule in the trap fluctuates. If the separation between the foci is increased, the size of the trap and the mean concentration of molecules in the trap increase (Figure 14 (b)), but the autocorrelation function develops a bump due to a fluctuating fluorescence signal from trapped molecules diffusing between the two laser foci.

Figure 15 shows there is a similar effect if there is a power imbalance between the two laser foci. As discussed in Ref. [19], it is possible to slightly increase the mean concentration of molecules in the trap by use of a higher power for the downstream laser beam (curves for 13.5 & 16.5 μW and 12 & 18 μW in Figure 15(a)), because molecules that escape through the lower power beam are returned when the flow reloads the trap. However, the autocorrelation develops a slight bump (Figure 15(b)) due to the fluctuating fluorescence as molecules diffuse within and in and out of the trap.

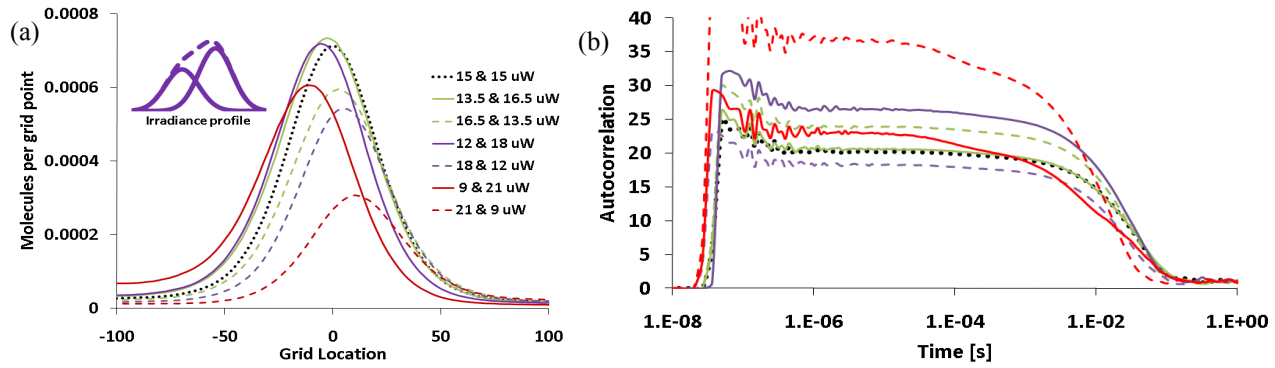

Figure 15: Effect of variation of power balance between the two laser spots. (a) Time-averaged concentration profiles within the trap; (b) Autocorrelation functions.

6. CONCLUSIONS

Fluorescently labeled biomolecules in solution, such as proteins and antibodies, may be individually detected in a confocal microscope, but Brownian diffusion limits the observation time for spectroscopic measurements and hinders the controlled sampling of large numbers of molecules. To address these issues, we have developed 100 nm cross-section nanochannels in fused silica and a means for actively controlling the electrokinetic transport of the solution within the nanochannel to achieve trapping of a single molecule within two overlapping focused laser spots, as well as rapid replacement following photobleaching. This paper focuses on Monte Carlo computer simulations of the processes that occur during the detection, delivery and trapping. The simulations incorporate algorithms that specify the precise timing of each detected photon, as is needed for implementing the trapping algorithms. Initial experiments have observed a slow down in diffusion by ~50, possibly due to molecules sticking. Simulations under these conditions indicate that trapping is easily achieved over a wide range of experimental parameters. In addition to validating prior experiments, simulations can help guide future experiments. For faster diffusion and for a limited electrokinetic speed of ~2 μm/ms, trapping is found to be achievable if the latency of feedback is less than ~100 μs, if the fluorescence lifetime of the emitter is less than ~3–4 ns, and if the total laser power is within the range of ~20–40 μW. Longer trapping times can be obtained by increasing the separation between the two laser foci or increasing the relative power of the down-stream laser spot, although the excitation profile then becomes spatially varying, leading to fluctuations in the fluorescence signal.

ACKNOWLEDGEMENTS

We acknowledge support from DARPA grant W911NF-07-1-0046, NIH grant EB-006639, NSF grant 0619789 and the Center for Laser Applications. For contributions to experimental developments, we thank Bruce Bomar, Brian Canfield, James Germann, Bill Hofmeister, Jason King, Isaac Lescano, Shaun Li, Paul Shen, Peter Sikorski, Alex Terekhov, and Yelena White from the Center for Laser Applications at the University of Tennessee Space Institute; Laura Edwards, Dale Hensley, Scott Retterer, and Darrell Thomas from the Center for Nanophase Materials Sciences at Oak Ridge National Laboratory; Dmitry Markov, Philip Samson, and John Wikswo from Vanderbilt Institute for Integrative Biosystems Research and Education at Vanderbilt University.

REFERENCES

[1] Selvin, P.R. and Ha, T., Editors, *Single-Molecule Techniques, A Laboratory Manual*, Cold Spring Harbor Laboratory Press (2008).

[2] Shera, E.B., Seitzinger, N.K., Davis, L.M., Keller, R.A. and Soper, S.A., "Detection of single fluorescent molecules," Chem. Phys. Lett. **174**, 553–557 (1990).

[3] Cohen, A.E. and Moerner, W.E. "Controlling Brownian motion of single protein molecules and single fluorophores in aqueous buffer," Opt. Express **16**, 6941–6956 (2008).

[4] Cohen, A.E., "Trapping and manipulating single molecules in solution," Ph.D. Dissertation, Stanford University, August (2006).

[5] Volkmuth, W.D. and Austin, R.H., "DNA electrophoresis in microlithographic arrays," Nature **358**, 600–602 (1992).

[6] Gajar, S.A. and Geis, M.W., "An ionic liquid-channel field-effect transistor," J. Electrochem. Soc. **139**, 2833–2840 (1992).

[7] Eijkel, J.C.T. and van den Berg, A., "Nanofluidics: what is it and what can we expect from it?" Microfluid. Nanofluid. **1**, 249–267 (2005).

[8] Mijatovic, D., Eijkel, J.C.T. and van den Berg, A., "Technologies for nanofluidic systems: top-down vs. bottom-up—a review," Lab. Chip. **5**, 492–500 (2005).

[9] Yuan, Z., Garcia, A.L., Lopez, G.P. and Petsev, D.N., "Electrokinetic transport and separations in fluidic nanochannels," Electrophoresis **28**, 595–610 (2007).

[10] Abgrall, P. and Nguyen, N.T., "Nanofluidic devices and their applications," Anal. Chem. **80**, 2326–2341 (2008).

[11] Craighead, H., "Future lab-on-a-chip technologies for interrogating individual molecules," Nature **442**, 387–393 (2006).

[12] Mannion, J.T. and Craighead, H.G., "Nanofluidic structures for single biomolecule fluorescent detection," Biopolymers **85**, 131–143 (2006).

[13] Hibara, A., Saito, T., Kim, H.-B., Tokeshi, M., Ooi, T., Nakao, M. and Kitamori, T., "Nanochannels on a fused-silica microchip and liquid properties investigation by time-resolved fluorescence measurements," Anal. Chem. **74**, 6170–6176 (2002).

[14] Karnik, R., Fan, R., Yue, M., Li, D., Yang, P., and Majumdar, A., "Electrostatic control of ions and molecules in nanofluidic transistors," Nano Lett. **5**, 943–948 (2005).

[15] Mourner, W.E., "New directions in single-molecule imaging and analysis," Proceedings of the National Academy of Sciences USA **104**, 12596-12602 (2007).

[16] Davis, L.M., Canfield, B.K., Li, X., Hofmeister, W.H., Lescano-Mendoza, I.P., Bomar, B.W., Wikswo, J.P., Markov, D.A., Samson, P.C., Daniel, C., Sikorski, Z. and Robinson, W., "Electrokinetic delivery of single fluorescent biomolecules in fluidic nanochannels," Proceedings of SPIE 7035, 70350A, 1-12 (2008).

[17] Davis, L., Sikorski, Z., Robinson, W., Shen, G., Li, X., Canfield, B., Lescano, I., Bomar, B., Hofmeister, W., Germann, J., King, J., White, Y. and Terekhov, A., "Maximum-likelihood position sensing and actively controlled electrokinetic transport for single-molecule trapping," Proceedings of SPIE **6862**, 68620P (2008).

[18] Davis, L.M., Canfield, B.K., Germann, J.A., King, J.K., Robinson, W.N., Dukes III, A.D., Rosenthal, S.J., Samson, P.C. and Wikswo, J.P., "Four-focus single-particle position determination in a confocal microscope," Proceedings of SPIE **7571**, 7571-36, 1-10 (2010).

[19] Davis, L.M. and Robinson, W.N., "Simulation of single-molecule trapping in a nanochannel," J. Biomed. Opt., in press (2010).

[20] Bunfield, D.H. and Davis, L.M., "Monte Carlo simulation of a single molecule detection experiment," Applied Optics 37, 2315-2326 (1998).

[21] Davis, L.M., Williams, J.G.K. and Lamb, D.T., "Computer simulation of gene detection without PCR by single molecule detection," Proceedings of SPIE **3570**, 282-293 (1999).

[22] Davis, L.M., Sun, Y. and Whitehead, B., "Analysis of ultrasensitive fluorescence experiments," Proceedings of SPIE **3602**, 379-390 (1999).

[23] Li, X., Hofmeister, W., Shen, G., Davis, L. and Daniel, C., "Fabrication and characterization of nanofluidics device using fused silica for single protein molecule detection," Proceedings of Materials and Processes for Medical Devices (MPMD) Conference and Exposition, September 23–25 (2007).

[24] Lyon, W. A., and Nie, S. M., "Confinement and detection of single molecules in submicrometer channels," Anal. Chem. **69**, 3400–3405 (1997).

VITA

William Robinson was born in the Fort Campbell Blanchfield Army Community Hospital on March 3, 1983. He received his Associate degree from Motlow State Community College in 2003 and his Bachelor of Science degree in May 2006 at Athens State University in Alabama. He completed his Master of Science at the University of Tennessee Space Institute in 2008.